



Politecnico di Torino

Department of Mechanical and Aerospace Engineering

Master of Science in Mechanical Engineering

Master Thesis

# **RANS simulation in complex terrain with the presence of the canopy**

**Candidate:** Alessandro Ribezzo

**Supervisors:** Prof. Eliodoro Chiavazzo  
Pietro Asinari  
Herbert Owen  
Matias Avila

**April 2020**



# Acknowledgements

All this work would not have been possible without the help of professor Asinari who presented me this opportunity and allow me to participate. My warmest thanks go to Herbert Owen and Matias Avila that with patience and passion introduced me to this challenging but fascinating world, and support me with their knowledge during my stay at the Barcelona Supercomputing Center and during the writing of the thesis, making my knowledge in the topic and its application much deeper. Another thanks goes to the other people of the center that helped me from all points of view, from the bureaucratic to the computational ones, and among them a special thanks goes to Sarath, that helps me a lot and beared all my questions with enormous patience.

This master thesis has received support from the European Union's Horizon 2020 research and innovation programme under grant agreement No 824158 (EoCoEII).



# Contents

<b>1</b>	<b>Introduction</b>	<b>1</b>
1.1	Barcelona Supercomputing Center . . . . .	3
1.2	The Benchmark . . . . .	3
1.2.1	Input Data . . . . .	4
1.2.2	Output Data . . . . .	4
1.3	CFD . . . . .	4
1.4	Softwares . . . . .	6
<b>2</b>	<b>Physics</b>	<b>9</b>
2.1	Compressible flow . . . . .	10
2.2	Incompressible flow . . . . .	11
2.3	RANS equations . . . . .	13
2.3.1	$\kappa - \epsilon$ model . . . . .	15
2.4	Coriolis effect . . . . .	16
2.5	Canopy effect . . . . .	16
2.6	Atmospheric stability . . . . .	17
2.7	Leaf Area Density and Index Analysis . . . . .	18
2.8	Complex Terrain effect . . . . .	18
2.9	Boundary Conditions . . . . .	19
2.10	Numerical Approximation . . . . .	21
<b>3</b>	<b>Simulations</b>	<b>23</b>
3.1	Simulations without canopy . . . . .	25

3.2	Simulations with canopy . . . . .	34
3.2.1	Mast 7 analysis . . . . .	38
3.2.2	Canopy effect . . . . .	40
3.2.3	Mesh refinement . . . . .	42
3.2.4	Buffer effect . . . . .	45
3.2.5	LAI and LAD impact . . . . .	53
3.2.6	Smoothing effect on LAI . . . . .	59
3.2.7	Comparison between smoothed LAI and LAD . . . . .	65
3.2.8	Smoothed LAI and mesh refinement comparison . . . . .	69
3.3	Mast 3 Analysis . . . . .	73
3.3.1	Mesh refinement . . . . .	74
3.3.2	LAI and LAD input data . . . . .	78
3.3.3	Terrain topography . . . . .	79
3.3.4	Changes in the zone . . . . .	81
3.3.5	Optimization . . . . .	89
<b>4</b>	<b>Conclusion</b>	<b>93</b>

# 1 Introduction

One of the critical points of our society is the use of renewable energy systems: among them the wind energy is, certainly, one of the most diffused and exploitable.

Wind turbines first emerged more than a century ago; following the invention of the electric generator in the 1830s, engineers started attempting to exploit wind energy to produce electricity.

So, wind power generation took place in the United Kingdom and the United States in 1887 and 1888, but modern wind power is considered to have been first developed in Denmark, where horizontal-axis wind turbines were built in 1891.

In wind turbines wind is used to produce electricity using the kinetic energy created by air in motion: wind first hits turbine's blades, causing them to rotate and turn the turbine connected to them; this movement transforms the kinetic energy in rotational energy, by moving a shaft which is connected to a generator, and thereby producing electrical energy. The output power is proportional to the dimensions of the rotor and to the cube of the wind speed.

Global installed wind-generation capacity onshore and offshore has increased by a factor of almost 75 in the past two decades, jumping from 7.5 gigawatts (GW) in 1997 to some 564 GW by 2018; production of wind electricity doubled between 2009 and 2013, and in 2016 wind energy accounted for 16% of the electricity generated by renewables.[8].

As wind energy is one of the fastest growing sources of sustainable energy production, the optimal onshore location, based on high and steady wind velocities and low turbulence levels, has almost been occupied by wind farms, while the cost of installing wind farms off-shore can be typically 100% higher than on-shore, due to higher costs for both foundations and connections to the electric grid and to maintenance .

For this reason the study of the wind behaviour in complex terrain has becoming more important.

Complex terrains are those terrains that have surfaces that influence the

wind in the atmospheric boundary layer (ABL) through terrain topology and roughness effects.

The presence of the canopy, moreover, affects the wind profile and characteristics; at first, it can be simplified as a roughness but, in order to understand better its impact it has to be modelled with proper characteristic and input data.

Trees are elevated sources for both momentum absorption and heat transfer and thus they differ from traditional surfaces since the exchange may be distributed at several model levels.

In these locations, so, turbulence and wind shear are higher, and in general wind conditions are harder to predict and there is the need to develop proper analysis.

Characterization of the wind resource is, obviously, of great importance in every wind-energy project.

Nevertheless, the quantification of the wind characteristics in a specific site is complex because it takes into account several phenomena taking place at different spatial and temporal scales. Wind, in fact, is first generated from pressure-gradient forces; nearer to the ground, seen as a blocking surface, friction gets more relevant; finally, close to the ground, micro-scale effects such as terrain shape and surface roughness becomes predominant for the wind profile and its characteristics.

One can define the ABL as "the lower region of the atmosphere where friction, turbulence and mixing are intense, and further identify a subregion called the roughness sublayer where the flow is strongly distorted by the presence of terrain and roughness"[1].

## 1.1 Barcelona Supercomputing Center

All the computations done in this work have been developed in the Computer Applications in Science and Engineering (CASE) Department, interdisciplinary research unit of the BSC-CNS, Barcelona Supercomputing Center, a public research center located in Barcelona, Catalonia, that hosts MareNostrum, a 13.7 Petaflops, Intel Xeon Platinum-based supercomputer, which also includes clusters of emerging technologies.

The simulations have been ran through Alya, a "simulation code for high performance computational mechanics that solves coupled multiphysics problems using high performance computing techniques for distributed and shared memory supercomputers, together with vectorization and optimization at the node level.

It can solve a wide variety of problems as incompressible/compressible flows, non-linear solid mechanics, chemistry, particle transport, heat transfer, turbulence modeling, electrical propagation, etc.

Multiphysics coupling is achieved following a multi-code strategy, relating different instances of Alya. MPI is used to communicate between the different instances, where each instance solves a particular physics"[5].

## 1.2 The Benchmark

The task of the benchmark is to model the flow in complex forested terrain and to provide wind profile characteristics at a number of validation locations where experimental results have been taken.

Between the two possible cases, one with westerly and one with easterly flow, in this work the latter has been developed; For what concert the input data the net radiative heat flux on the top of the canopy is obtained from field measurements (here not used), while the geostrophic pressure gradient has been obtained by mesoscalar simulations.

The subject of this thesis is the study and the analysis of the wind behaviour in complex terrain and the canopy effects on it.

The site considered is located in Sweden, near Hornamossen, a very big and forested rural zone.

The forest consists predominately of spruce, but also pine and some deciduous forest types are present, making the forest itself heterogeneous with patches of trees of different densities, height and age.

The site presented is, in this way, very heterogeneous in both topography and land cover.

Due to those characteristics the site offers many possibilities of investigat-

ing heterogeneities in the wind field due to vegetation and elevation.

### 1.2.1 Input Data

The data has been collected within a research collaboration that consists of Swedish Vindforsk IV research project ForestWind, EU ERAnet NEWA (New European Wind Atlas) project and industry partner OX2 Vindkompaniet.

"The surface data consists of a data set with 10x10 m resolution covering 40x40 km and containing elevation height, forest height and Plant Area Density (LAD) provided in netCDF format. The vertical resolution of LAD is 1 m. The vertically integrated LAD, the LAI is also included for simplicity. A flag for water surface is also included, with the value 1 for water and 0 otherwise." [7]

For what concern input data for the boundary conditions of the models, an input file in netCDF format is provided and it comes from a 3x3 km resolution run by the mesoscale model WRF, that include wind speed, tendencies, geostrophic wind speed and height for 72 hours.

Ten validation points are present, where the vertical wind profile has to be computed.

We have taken in account one stationary run for a single atmospheric state in the easterly wind case where suitable geostrophic wind speeds and directions are 12.2 m/s, 115°.

Following the conclusions of Ivanell et al [9] the following constant values should be used when using the Sogachev et al [13] turbulence model:  $k = 0.4$ ,  $C_d = 0.2$ ,  $C_{\epsilon 1} = 1.176$ ,  $C_{\epsilon 2} = 1.920$ ,  $\sigma_k = 1$ ,  $\sigma_\epsilon = 1.238$  and  $C_\mu = 0.033$

### 1.2.2 Output Data

As output data we have evaluated the wind profile, direction and turbulent kinetic energy trend in the height of some validation points.

## 1.3 CFD

Computational fluid dynamics (CFD) is the science of predicting fluid flow, heat transfer, mass transfer, chemical reactions, and related phenomena by solving the mathematical equations which govern these processes

using a numerical process. It operates in this way:

- Mathematical model of a physical problem
- Conservation of matter, momentum and energy must be satisfied in the region of interest
- Fluid properties are modelled empirically
- Simplifying assumptions, such as steady-state or incompressible fluids, are made according to the problem
- Provide appropriate initial and boundary conditions for the problem
- Get the solution

The numerical aspects of the CFD is to apply numerical discretization methods to develop approximations of the governing equations of fluid mechanics in the fluid region of interest. In this way a partial differential equation become, through a space discretization, a ordinary differential equation that become itself, through a time discretization, a set of algebraic equations for each time step. Three main space discretization methods are available:

- Finite differences, in which the domain is discretized
- Finite volumes, in which the domain is discretized and surface and volumes quantities are simplified
- Finite elements, in which the main point is the element itself and the solution is the approximation of the element. It is based on the weak form of the governing equations, an integral form of the equations that requires a weaker continuity on the field variables. For fluid the weak form can be obtained using direct formulation or weighted residual methods. The grid is based on elements; in each one the solution is written as summation of other function and coefficients.

$$T(x, y) = T^e(x, y) = \sum T_j^e \phi_j^e(x, y) \quad (1.1)$$

where  $T_j^e$  is the value of the dependent variable at the element node  $j$  and  $\phi_j^e$  is properly chosen approximation function.

In this work the finite element method has been used. The temporal discretization methods can be:

- Implicit, that are unconditionally stable but they need more efforts on computation
- Explicit, that can be easily applied but they yield conditionally stable finite equations, restricted by time steps.

To achieve stability, that means that the error reach the converge during the numerical simulation, pre-conditioning method can be utilized specially when the matrix are ill-posed.

## 1.4 Softwares

All the computations and simulations done in this thesis are developed at the Barcelona Supercomputing Center, exploiting the biggest spanish supercomputer, the MareNostrum IV. The code utilized to achieve the tasks is Alya, an homemade imulation code for high performance computational mechanics. Alya solves coupled multiphysics problems using high performance computing techniques for distributed and shared memory supercomputers, together with vectorization and optimization at the node level. In order to get the geometry and the mesh, instead, Gmsh has been used. It is a free 3D finite element mesh generator with a built-in CAD engine and post-processor. Its design goal is to provide a fast, light and user-friendly meshing tool with parametric input and advanced visualization capabilities. Gmsh is built around four modules: geometry, mesh, solver and post-processing. Finally, to post-process the results and analyze them Paraview, an open-source, multi-platform data analysis and visualization application, has been used. In order to use Alya you have to create some input files, written in Fortran :

- CaseName.dat: general data for the run, including the time step used and the time period for calculation
- CaseName.dom.dat: It has the options related to the mesh, as the number of nodes, the types of elements, the rule of integration. It includes also other geometry files like
  - CaseName.geo.dat: It has the main information about the mesh: the coordinates of each node and the conectivity of the nodes.
  - CaseName.set.dat : It creates some subdomain for the postprocessing process.

- `CaseName.ker.dat`: It contains the properties of the materials, some general options about numerical aspects as mesh division, and general postprocessing variable options. When coupling different physics some variables may be shared by modules. These variables are located here. This is a mandatory module that also includes specific numerical treatment, like mesh multiplication or division. And also post process for generic variables
- `CaseName.post.alyadat`: It gives some information about the post-process of the simulation

The last input file is build according to the type of simulation that you are going to run; in our case we used the incompressible flow for Navier-Stokes equation, the NASTIN module:

- `CaseName.nsi.dat`: It is subdivide in :
  - Physical problem: It has the description of the physical problem such as the presence of temporal derivatives or convective term and the materials parameters.
  - Numerical treatment: It contains the numerical part of the problem, such as stabilization parameters, safety factors, algorithm for equations.
  - Output and postprocess: In this subsection there are the informations about the post processing such as the physical variables to compute and where to compute them
  - Boundary conditions: In the last subsection there is the description of the boundary conditions of the problem. Also the initial conditions are here defined in a transient problem.

In order to postprocess the results has been used Paraview, an open-source, multi-platform data analysis and visualization application where users can build visualizations to analyze their data using both qualitative and quantitative techniques.

It is a program on purpose developed to analyze extremely large datasets using distributed memory computing resources and it can be also run on supercomputers to analyze datasets of petascale sizes.



## 2 Physics

In physics, the Navier–Stokes equations describe the motion of viscous fluid substances. The balance equations arise from Newton’s second law to fluid motion, together with the assumption that the stress in the fluid is the sum of a diffusing viscous term (proportional to the gradient of velocity) and a pressure term, describing viscous flow. Navier–Stokes equations are useful because they describe the physics of many phenomena of scientific and engineering interest.

The Navier–Stokes momentum equation can be derived as a particular form of the Cauchy momentum equation, whose general convective form is:

$$\frac{D\mathbf{u}}{Dt} = \frac{1}{\rho} \nabla \cdot \boldsymbol{\sigma} + \mathbf{g} \quad (2.1)$$

By setting the Cauchy stress tensor  $\boldsymbol{\sigma}$  to be the sum of a viscosity term  $\boldsymbol{\tau}$  (the deviatoric stress) and a pressure term  $-p\mathbf{I}$  (volumetric stress) we get the Cauchy momentum equation in the convective form:

$$\rho \frac{D\mathbf{u}}{Dt} = -\nabla p + \nabla \cdot \boldsymbol{\tau} + \rho \mathbf{g} \quad (2.2)$$

where:

$\frac{D}{Dt}$  is the material derivative, defined as  $\frac{\partial}{\partial t} + \mathbf{u} \cdot \nabla$ ,

$\rho$  is the density,

$\mathbf{u}$  is the flow velocity,

$\nabla \cdot$  is the divergence,

$p$  is the pressure,

$\boldsymbol{\tau}$  is the deviatoric stress tensor, which has order two,

$\mathbf{g}$  represents body accelerations acting on the continuum as gravity.

Through the conservation of the mass we get the continuity equation:

$$\frac{\partial \rho}{\partial t} + \nabla \cdot \rho \mathbf{u} = 0 \quad (2.3)$$

Using the latter, the conservation form of the Cauchy momentum equation can be written:

$$\frac{\partial}{\partial t}(\rho \mathbf{u}) + \nabla \cdot (\rho \mathbf{u} \otimes \mathbf{u}) = -\nabla p + \nabla \cdot \boldsymbol{\tau} + \rho \mathbf{g} \quad (2.4)$$

where  $\otimes$  is the outer product.

The left side of the equation is composed by time-dependent and convective components. The right side of the equation is in effect a summation of hydrostatic effects, the divergence of deviatoric stress and body forces. The Navier–Stokes equations derive by the Cauchy equations specifying the stress tensor through a constitutive relation: by expressing the deviatoric (shear) stress tensor in terms of viscosity and the fluid velocity gradient, and assuming constant viscosity, the above Cauchy equations will lead to the Navier–Stokes ones

## 2.1 Compressible flow

The compressible momentum Navier–Stokes equation results from the following assumptions on the Cauchy stress tensor:

- It is Galileian invariant: it does not depend directly on the flow velocity, but only on spatial derivatives of the flow velocity.
- It is linear in its variable
- The fluid is assumed to be isotropic, the Cauchy stress is an isotropic tensor; furthermore, since it is also symmetric, it can be expressed in terms of the bulk viscosity  $\lambda$  and the dynamic viscosity  $\mu$ .

The linear stress constitutive equation, therefore, is:

$$\boldsymbol{\sigma} = \lambda(\nabla \cdot \mathbf{u})\mathbf{I} + 2\mu\boldsymbol{\epsilon} \quad (2.5)$$

where  $\mathbf{I}$  is the identity tensor,

$\boldsymbol{\epsilon} = \frac{1}{2}\nabla\mathbf{u} + \frac{1}{2}(\nabla\mathbf{u})^T$  is the rate-of-strain tensor,  
 $\nabla \cdot \mathbf{u}$  is the rate of expansion of the flow.

By decomposing the stress tensor into isotropic and deviatoric parts:

$$\boldsymbol{\sigma} = \left(\lambda + \frac{2}{3}\mu\right)(\nabla \cdot \mathbf{u})\mathbf{I} + \mu(\nabla\mathbf{u} + (\nabla\mathbf{u})^T) - \frac{2}{3}(\nabla \cdot \mathbf{u})\mathbf{I} \quad (2.6)$$

Imposing  $\zeta \equiv \lambda + \frac{2}{3}\mu$ , we get to the linear constitutive equation in the form usually employed:

$$\boldsymbol{\sigma} = \zeta(\nabla \cdot \mathbf{u})\mathbf{I} + \mu(\nabla \mathbf{u} + (\nabla \mathbf{u})^T) - \frac{2}{3}(\nabla \cdot \mathbf{u})\mathbf{I} \quad (2.7)$$

Both second viscosity  $\zeta$  and dynamic viscosity  $\mu$  are in general dependent on density, on each other and, in compressible flows, also on temperature. By computing the divergence of the stress tensor, we finally get the Navier–Stokes momentum equation in its convective form:

$$\rho\left(\frac{\partial \mathbf{u}}{\partial t} + \mathbf{u} \cdot \nabla \mathbf{u}\right) = -\nabla \bar{p} + \mu \nabla^2 \mathbf{u} + \frac{1}{3}\mu \nabla(\nabla \cdot \mathbf{u}) + \rho \mathbf{g} \quad (2.8)$$

That can be written, with the total derivative, as:

$$\rho \frac{D\mathbf{u}}{Dt} = -\nabla \bar{p} + \mu \nabla^2 \mathbf{u} + \frac{1}{3}\mu \nabla(\nabla \cdot \mathbf{u}) + \rho \mathbf{g} \quad (2.9)$$

In its conservation form it can be written as :

$$\frac{\partial}{\partial t}(\rho \mathbf{u}) + \nabla \cdot (\rho \mathbf{u} \otimes \mathbf{u}) = -\nabla \bar{p} + \mu \nabla^2 \mathbf{u} + \frac{1}{3}\mu \nabla(\nabla \cdot \mathbf{u}) + \rho \mathbf{g} \quad (2.10)$$

Bulk viscosity is assumed to be constant, otherwise it should not be taken out of the last derivative. The effect of the volume viscosity  $\zeta$  is that the mechanical pressure is not equivalent to the thermodynamic pressure:

$$\bar{p} = p - \zeta \nabla \cdot \mathbf{u} \quad (2.11)$$

Note that this difference is usually negligible.

The convective acceleration term can also be written as

$$\mathbf{u} \cdot \nabla \mathbf{u} = (\nabla \times \mathbf{u}) \times \mathbf{u} + \frac{1}{2}\nabla u^2 \quad (2.12)$$

where the vector  $(\nabla \times \mathbf{u}) \times \mathbf{u}$  is known as the Lamb vector.

## 2.2 Incompressible flow

For the special case of an incompressible flow, the pressure constrains the flow so that the volume of fluid elements is constant: for this reason we

obtain:  $\nabla \cdot \mathbf{u} = 0$

The incompressible momentum Navier–Stokes equation results from the previous assumptions on the Cauchy stress tensor. The Stokes' stress constitutive equation is :

$$\boldsymbol{\tau} = 2\mu\boldsymbol{\epsilon} \quad (2.13)$$

Expliciting  $\boldsymbol{\epsilon}$  the equation becomes:

$$\boldsymbol{\tau} = \mu(\nabla\mathbf{u} + \nabla\mathbf{u}^T) \quad (2.14)$$

Dynamic viscosity  $\mu$  is not constant because in incompressible flows it can depend on density and on pressure.

Any equation expliciting one of these transport coefficient in the conservative variables is called an equation of state.

The divergence of the deviatoric stress is given by:

$$\nabla \cdot \boldsymbol{\tau} = 2\mu\nabla \cdot \boldsymbol{\epsilon} = \mu\nabla \cdot (\nabla\mathbf{u} + \nabla\mathbf{u}^T) = \mu\nabla^2 \quad (2.15)$$

due to  $\nabla \cdot \mathbf{u} = 0$  for an incompressible fluid.

The incompressible flow assumption typically holds well with all fluids at low Mach numbers. In those cases the following identity holds:

$$\frac{1}{\rho_0}\nabla p = \nabla\left(\frac{p}{\rho_0}\right) = \nabla w \quad (2.16)$$

where  $w$  is the specific thermodynamic work, the internal source term.

Dividing by the density the momentum equation in convective form is:

$$\frac{\partial\mathbf{u}}{\partial t} + (\mathbf{u} \cdot \nabla)\mathbf{u} - \nu\nabla^2\mathbf{u} = -\nabla w + \mathbf{g} \quad (2.17)$$

where  $\nu = \frac{\nu}{\rho_0}$  is the kinematic viscosity.

Summarizing, the Navier-Stokes equations for an incompressible fluid state that:

$$\nabla \cdot \mathbf{u} = 0 \quad (2.18)$$

continuity equation

$$\frac{\partial\rho\mathbf{u}}{\partial t} + \nabla \cdot (\rho\mathbf{u} \cdot \mathbf{u}) = -\nabla p + \mu\nabla^2\mathbf{u} \quad (2.19)$$

momentum equation

where  $a = \rho \frac{u^2}{L}$  is the non-linear advective term and  $b = \mu \frac{u}{L^2}$  is the viscous term.

The Reynolds number is  $Re = \rho \frac{uL}{\mu} \propto \frac{a}{b}$

As can be easily seen the non-linear advective term tends to amplify the perturbations pushing the flow towards instability.

For this reason for large Reynolds number there is instability, while for low one there is not turbulence.

The latter condition, for wind study, is very uncommon.

The main problems of the turbulence are that it is a three dimensional phenomena, it depends on time and it rotates.

Moreover multiple spatial and time scale are involved.

Another property of the turbulence is the energy cascade due to the energy transmission: the kinetic energy enters the turbulence at the largest scales of motion, and then is transferred to smaller and smaller scales until it is dissipated by the viscous actions.

Due to all this issues a DNS, direct numerical simulation, approach, in which every scale is computed and nothing is modelled, is practically impossible for the actual computers. There are two possibilities:

- RANS, the Reynolds Averaged Navier Stokes approach, in which the attention is focused on the mean flow properties and the effect of turbulence terms is modelled.
- LES, the Large Eddy Simulation approach, in which the behaviour of the largest eddies is tracked and the effect of the unresolved scale is modelled. In such way small eddies are approximated

## 2.3 RANS equations

It is the approach used in this work; it consists on the computation of the effect of turbulence on the mean flow properties. It is based on the Reynolds decomposition in which the value of a property is decomposed in a mean and a fluctuating component:

$$u = U + u' \quad (2.20)$$

with  $u'$  transient fluctuating component that disappear as we are interested only in the mean value and  $U = \frac{1}{\tau} \int_0^\tau u dt$  steady time averaged value. The continuity equations becomes:

$$\nabla \cdot (\mathbf{U} + \mathbf{u}') = 0 \quad (2.21)$$

$$\nabla \cdot \mathbf{U} = 0 \quad (2.22)$$

While the momentum equation becomes :

$$\frac{\partial \rho \mathbf{U}}{\partial t} + \nabla \cdot (\rho \mathbf{U} \cdot \mathbf{U}) = -\nabla p + \nabla \cdot (\mu \nabla \mathbf{U} - \rho \mathbf{u}' \mathbf{u}') \quad (2.23)$$

The additional term  $\rho \mathbf{u}' \mathbf{u}'$  is due to the convective transport and it is called Reynolds stress tensor. Paying attention to the last two terms of the 1.24 they can be grouped as:

$$\begin{aligned} \mu \Delta \mathbf{U} - \rho \mathbf{u}' \mathbf{u}' &= \frac{\delta}{\delta x_j} \left( \mu \frac{\delta u_i}{\delta x_j} - \rho u'_i u'_j \right) \\ \tau_{i,j} &= \mu \frac{\delta u_i}{\delta x_j} - \rho u'_i u'_j \end{aligned}$$

where  $\tau_{i,j}$  is the total shear stress. In this way, besides the viscous part, an additional term has been added to the total shear stress.

To obtain the closure of the problem, an approximation of the Reynolds stresses has to be done, relating the latter with the velocity field of the average flow.

The Boussinesq approximation, introducing the concept of eddy viscosity, is this relationship.

A new proportionality constant  $\nu_t > 0$ , the turbulence eddy viscosity, has been introduced.

$$-\overline{u'_i u'_j} = \nu_t \left( \frac{\partial \bar{u}_i}{\partial x_j} + \frac{\partial \bar{u}_j}{\partial x_i} \right) - \frac{2}{3} k \delta_{ij} \quad (2.24)$$

$$(2.25)$$

Which can be written as

$$-\overline{u'_i u'_j} = 2\nu_t S_{ij} - \frac{2}{3} k \delta_{ij} \quad (2.26)$$

where:

- $S_{ij}$  is the mean rate of strain tensor
- $\nu_t$  is the turbulence eddy viscosity
- $k = \frac{1}{2} \overline{u'_i u'_i}$  is the turbulence kinetic energy
- $\delta_{ij}$  is the Kronecker delta.

In this way the simplified model of the RANS equations becomes:

$$\nabla \cdot \mathbf{u} = 0 \quad (2.27)$$

$$\frac{\partial}{\partial t} \mathbf{u} + \mathbf{u} \cdot \nabla \mathbf{u} = -\nabla \left( \frac{p}{\rho} \right) + \nabla \cdot (v_t \nabla^s \mathbf{u}) \quad (2.28)$$

where :

$$v_t = C_\mu \frac{k}{\epsilon} \quad (2.29)$$

### 2.3.1 $\kappa - \epsilon$ model

The closure problem used is the modified  $k - \epsilon$  model accounting for Coriolis effects and using the Apsley and Castro correction for the mixing length limitation[2].

With mixing length we refer to the characteristic length within which a fluid parcel will conserve its properties before mixing with the surrounding fluid.

The added equations are:

$$\frac{\partial}{\partial t} k + \mathbf{u} \cdot \nabla k = +\nabla \cdot \left( \frac{v_t}{\sigma_k} \nabla k \right) + P_k - \epsilon \quad (2.30)$$

for the turbulent kinetic energy

$$\frac{\partial}{\partial t} \epsilon + \mathbf{u} \cdot \nabla \epsilon = +\nabla \cdot \left( \frac{v_t}{\sigma_\epsilon} \nabla \epsilon \right) + \frac{\epsilon}{k} (C'_1 P_k - C_2 \epsilon) \quad (2.31)$$

for the dissipation of the turbulent kinetic energy.

In both the equations  $P_k = 2v_t \nabla^s \mathbf{u} : \nabla^s \mathbf{u}$  and  $\nabla^s \mathbf{u} = 0.5(\nabla \mathbf{u} + \nabla^T \mathbf{u})$ .

In this set of four equations the unknowns are the velocity field  $\mathbf{u}$ , the pressure  $p$ , the turbulent kinetic energy  $k$ , the dissipation rate of turbulent kinetic energy  $\epsilon$ .

The modified value of the constant  $C'_1$  is due to the Apsley and Castro [2] modification to prevent the increase of the mixing length  $l_m = C_\mu^{3/4} \frac{k^{3/2}}{\epsilon}$  above a maximum value  $l_{max}$  when accounting for Coriolis effect.

$$C'_1 = C_1 + (C_2 - C_1) \frac{l_m}{l_{max}} \quad (2.32)$$

where  $l_{max} = 0.00027 \frac{|\mathbf{u}_g|}{2|\omega| \sin \lambda}$  in which  $\mathbf{u}_g$  is the geostrophic wind velocity and  $\lambda$  the latitude.

Note that, if no Coriolis forces are considered (i.e.  $\lambda = 0$ ), then  $l_{max} \rightarrow \infty$  and  $C'_1 = C_1$ .

According to the input data the constant values are :  $k = 0.4, C_d = 0.2, C_{\epsilon 1} = 1.176, C_{\epsilon 2} = 1.920, \sigma_k = 1, \sigma_\epsilon = 1.238$  and  $C_\mu = 0.033$

## 2.4 Coriolis effect

One of the key point to achieve the correct analysis is to take in account the Coriolis effect [10].

The Coriolis effect is the "deflection due to an inertial or fictitious force that acts on objects that are in motion within a frame of reference that rotates with respect to an inertial frame" [14]. In a reference frame with clockwise rotation, the force acts to the left of the motion of the object. In one with counterclockwise rotation, the force acts to the right. To take this phenomena in account, the momentum equation is modified :

$$\frac{\partial}{\partial t} \mathbf{u} + \mathbf{u} \cdot \nabla \mathbf{u} = -\nabla \left( \frac{p}{\rho} \right) + \nabla \cdot (\nu_t \nabla^s \mathbf{u}) - 2\boldsymbol{\omega} \times \mathbf{u} \quad (2.33)$$

where  $\boldsymbol{\omega}$  is the Earth's angular velocity.

## 2.5 Canopy effect

The existence of a canopy alters the wind profile. Therefore, you need to take into account the effect of the canopy on the wind studying the wind profile and its characteristics.

A simple approach to model it is to modify the surface friction including a displacement height and creating a logarithmic profile starting from the actual profile observed over a forest canopy.

A better alternative, used here and that can be only used in CFD models, is to take the forest into account in the Navier Stokes equations as additional resistance terms induced by the porous region.

The equations for the turbulence variables in the RANS model are properly modified in the canopy region.

The counterpart of this approach is that there are several models, developed for one specific set of turbulence model constants and their performance degrades significantly using other constants.

Sogachev model, the one used in this work, is a model that can provide

good results not only for different turbulence constants but also for different RANS turbulence models. The momentum equation is, according to this phenomena, modified:

$$\frac{\partial}{\partial t} \mathbf{u} + \mathbf{u} \cdot \nabla \mathbf{u} = -\nabla \left( \frac{p}{\rho} \right) + \nabla \cdot (\nu_t \nabla^s \mathbf{u}) - 2\omega x \mathbf{u} - C_d LAD |\mathbf{u}| \mathbf{u} \quad (2.34)$$

and the dissipation rate of the turbulent kinetic energy is :

$$\frac{\partial}{\partial t} \epsilon + \mathbf{u} \cdot \nabla \epsilon = +\nabla \cdot \left( \frac{\nu_t}{\sigma_\epsilon} \nabla \epsilon \right) + \frac{\epsilon}{k} (C_1 P_k - C_2 \epsilon + C_3 C_d LAD |\mathbf{u}| k) \quad (2.35)$$

where  $LAD$  is the leaf area density and  $C_3 = (C_1 - C_2) 12 C_\mu^{1/2}$

## 2.6 Atmospheric stability

The atmospheric stability, neutrality and instability concept are related to the physical conditions of dynamic equilibrium of the mass of air.

The atmospheric instability is the condition for which the vertical movement of the particles of air is enhanced [3], while the stability hinder this mixing and enhance the stratification of air.

This condition is function of the trend of the temperature in the height, the vertical thermal gradient, and to determine the correlation between the temperature and the stability properties of the air, the dry adiabatic lapse rate has to be taken into account. It is the trend of the temperature in the air for an adiabatic mass of air; in this conditions the temperature decreases of about 1°C every 100m.

In the real cases the vertical thermal gradient is often different from the adiabatic one due several factors, as the thermal radiation during the day and the night.

Comparing the thermal adiabatic gradient with the real one, three different situations can be witnessed:

- Unstable atmosphere, for superadiabatic gradient
- Stable atmosphere, for subadiabatic gradient
- Neutral atmosphere, for adiabatic gradient

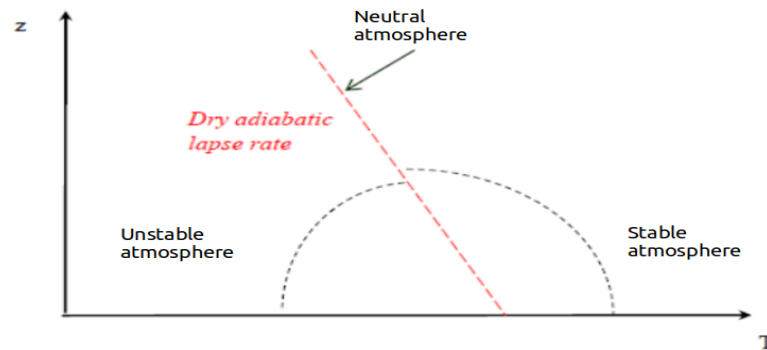


Figure 2.1: Region of atmospheric stability, instability and neutrality, function of the thermal gradient trend in the height

In this work, the neutral atmosphere is taken into account for the simulations.

## 2.7 Leaf Area Density and Index Analysis

As input data the Leaf Area Density and the Leaf Area Index are given. The leaf area density (LAD) distribution is a key index for characterizing the vertical and horizontal crown structures and is defined as the total one-sided leaf area per unit volume. The Leaf Area Index, instead, is the integral in the vertical direction of the LAD inside the canopy; being the integral, it is the sum of all the LAD values in the vertical direction, and for this reason it has a much higher value.

$$LAI = \int_0^{h_{canopy}} LAD dz$$

## 2.8 Complex Terrain effect

The study and the characterization of the properties of the wind plays, obviously, a major role in the wind energy projects; in some case, as complex terrain, this study is really difficult to achieve due to the fact that the wind is associated with a multitude of phenomena taking place at a different spatial and temporal scales. Wind is first generated from pressure-

gradient forces at a global level, providing the geostrophic wind observed at high altitudes. The latter is the theoretical wind that would result from an exact balance between the Coriolis force and the pressure gradient force, and it is, so, parallel to the isobars. As the ground is approached, friction forces become more important: here the ground is perceived as a blocking surface that is absorbing momentum. Close to the ground, micro-scale effects such as terrain shape and surface roughness become important and affect the wind significantly.

One can define the atmospheric boundary layer (ABL) as the lower region of the atmosphere where friction, turbulence and mixing are intense, and further identify a sub-region called the roughness sub-layer where the flow is strongly distorted by the presence of terrain and roughness.

Therefore, the wind is generated by pressure gradients (planetary time scale) that are affected by friction (meso-scale effect) and by roughness close to the ground (micro-scale effect): this means that the choice of one scale taking in account everything is practically impossible.

Another issue with this challenge is that the wind strongly depends on the atmospheric conditions and period of the year; this increase the complexity of the problem.

## 2.9 Boundary Conditions

In order to solve numerically the RANS equations, proper boundary conditions must be added for all the unknowns [9]. To do so, the domain is divided in four zone, each one with proper boundary conditions:

- Top, where symmetry boundary conditions are imposed: it involves that the gradients in the normal direction of the tangent component of the velocity, of the turbulent kinetic energy  $k$  and of the dissipation of turbulent kinetic energy  $\epsilon$  have been set to zero, while the pressure is set to geostrophic and the normal component of the velocity is fixed to be zero.

$$\begin{aligned}\frac{\partial k}{\partial n} &= 0 \\ \frac{\partial \epsilon}{\partial n} &= 0 \\ \frac{\partial \mathbf{u}}{\partial n} &= 0\end{aligned}$$

- Bottom, where zero diffusion through the wall is imposed for the turbulent kinetic energy,

$$\nabla k \cdot \mathbf{n} = 0 \quad (2.36)$$

while  $\epsilon$  is imposed in order to get that the production of it is equal to the dissipation

$$\epsilon(\delta_w) = \frac{k^{3/2} C_\mu^{3/4}}{\kappa(\delta_w + z_0)} \quad (2.37)$$

. A wall law satisfying the Monin-Obukhov similarity theory [12] for velocity field and pressure has been imposed on the momentum and turbulence equations. It consist on removing a boundary layer of thickness  $\delta_w$  above  $z_0$  imposing a shear stress  $\tau_w$  tangent to the wall, expressed in terms of two velocity scales,  $u_{*v}$  and  $u_{*k}$ , and based on the tangent velocity and the turbulent kinetic energy:

$$\tau_w = -u_{*v} u_{*k} \frac{u}{|u|} \quad (2.38)$$

where:

$$u_{*v} = \frac{|u| \kappa}{\ln(1 + \frac{\delta_w}{z_0})} \text{ and}$$

$$u_{*k} = k^{1/2} C_\mu^{1/4}$$

in which  $u$  is the velocity component tangent to the wall while the friction velocity  $u_{*v}$  is obtained from the neutral atmospheric velocity profile at a distance  $\delta_w$  from the wall, with  $\kappa$  Von Karman constant and  $z_0$  the roughness length.

- Inflow, where a vertical profile for  $u$  inflow velocity,  $k$  and  $\epsilon$  is imposed generated from a single-column (1D) precursor simulation assuming flat terrain and uniform roughness and using the input data of the problem.

Note that a lateral boundary is defined as an inflow one if its outwards pointing normal forms an angle greater than  $85^\circ$  with respect to the one dimensional wind profile and as an outflow otherwise.

- Outflow, where symmetry boundary conditions have been imposed for  $k$  and  $\epsilon$  while geostrophic pressure and no shear stress are imposed for the momentum equation  $\frac{\partial k}{\partial n} = 0$   
 $\frac{\partial \epsilon}{\partial n} = 0$

## 2.10 Numerical Approximation

The coupled set of equations of momentum, continuity and turbulence equations is uncoupled using a block iterative strategy. At first, velocity and pressure are decoupled from the turbulence unknowns. In this way, the problem without turbulent unknowns is solved with an Orthomin solver, while  $k$  and  $\epsilon$  are solved iteratively within an internal loop.

Using Alya equations are discretized in space using the finite element method, FEM.

In order to stabilize both the Navier Stokes equations and the equations for the turbulent unknowns, the ASGS stabilization is used.

A straightforward way to solve the discretized RANS equations (velocity and pressure) is to consider the monolithic scheme, that consists in solving the momentum and continuity equations in a coupled way, but it can lead to badly conditioned systems that would require very robust preconditioners, such as ILU, that have bad speedup properties.

To avoid it, the use of the fractional step techniques is utilized; they uncouple velocity and pressure but introduce errors due the splitting.

For this thesis we have used an Orthomin solver that converges to the monolithic scheme and uses an approximate Schur complement preconditioner (similar to fractional step schemes): it has proved to be efficient and capable of scaling up to thousands of processors.

Solving the pressure a Deflated Conjugate Gradient solver with a linelet preconditioner is used, while for the velocity and turbulence unknowns, that lead to unsymmetric problems, a GMRES solver is used.



### 3 Simulations

The task of this work is to simulate and provide at a number of validation location the wind profile over a complex and forested terrain with RANS equations using *ALYA*, an HCP simulation code for high performance computational mechanics that solves coupled multi physics problems using high performance computing techniques for distributed and shared memory supercomputers, together with vectorization and optimization at the node level.



Figure 3.1: Zone considered for the simulation [7]

The case considered, between the two presented in the benchmark, is the easterly one with stationary flow conditions. The zone under analysis has been divided in:

- A farm zone, in which there is a refined mesh and it is the zone under study and for which the input data is the real topography
- A buffer zone, with a very coarse mesh that did not coincide with the real topography of the terrain but it is a smoothing of the zone around the farm on
- A transition zone, between the two in which the mesh can move gradually from the farm one to the buffer one.

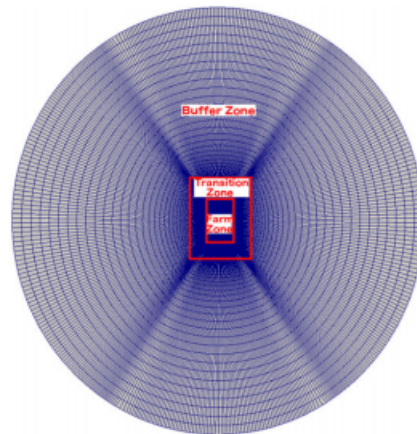


Figure 3.2: Example of the three zones [4]

The main properties taken in consideration and analyzed are the turbulent kinetic energy, the wind velocity, both in the module and the direction.

The simulations done can be grouped in two main groups:

- Simulations over a complex terrain without canopy
  - Mesh refinement analysis, in which various dimension of meshes have been tried
  - Buffer dimension analysis, in which different sizes of the buffer zone have been tried

- Mesh rotation analysis, in which the mesh has been rotated according to the wind direction
  - Vertical refinement analysis, in which the vertical mesh has been refined
  - Impact of the buffer zone, in which the cases with buffer and without it have been compared
  - Impact of the transition zone, in which different size of the transition zone have been compared
  - Coriolis effect analysis, in which the a case without Coriolis effect has been compared with a case with it
- Simulation over a complex terrain with canopy
    - Buffer impact analysis
    - Mesh refinement
    - LAI and LAD impact analysis
    - Numerical regularization analysis

### 3.1 Simulations without canopy

Almost all the simulations done in the preliminary cases without canopy had not showed significant result differences; this is due to the fact that the zone considered is a semi-complex one, with a majority of flat zones and a maximum difference of about 100m between the highest and the lowest part of the zone, as can be seen in the figures 3.3 and 3.4

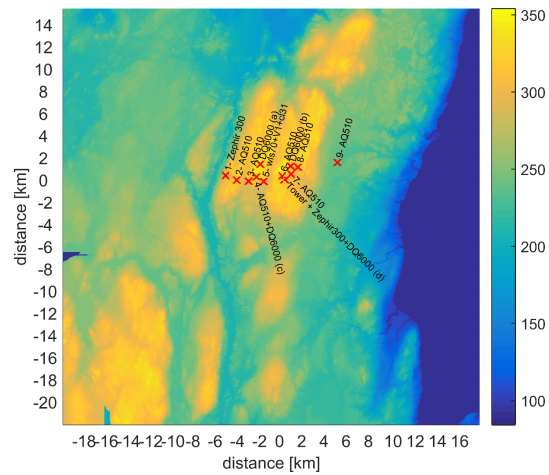


Figure 3.3: Height of the zone under study [7]

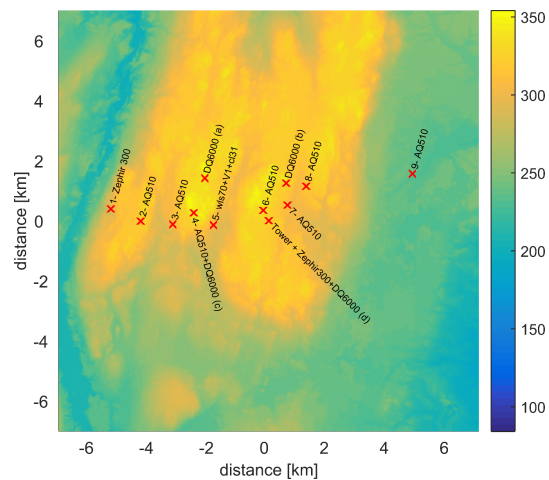


Figure 3.4: Height of the zone under study, zoom in the masts zone [7]

For this reason, for example, the mesh refinement, in which the used meshes are  $80 \times 80$ ,  $160 \times 160$ ,  $40 \times 40$  have not showed particular differences in the wind profile as can be seen in the following comparison between  $80 \times 80$  and  $40 \times 40$  in figure 3.5, 3.6, 3.7 and 3.8:

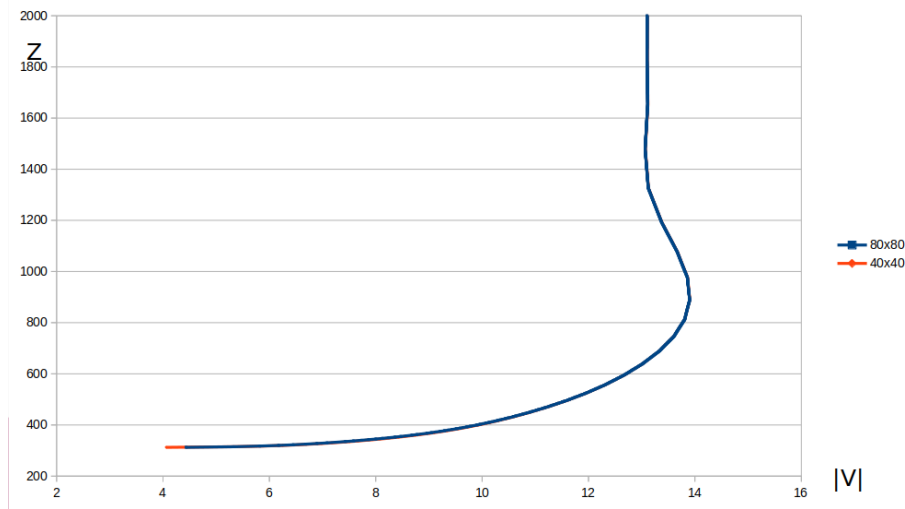


Figure 3.5: Comparison of the wind speed between the 80x80 mesh and the refined 40x40 mesh

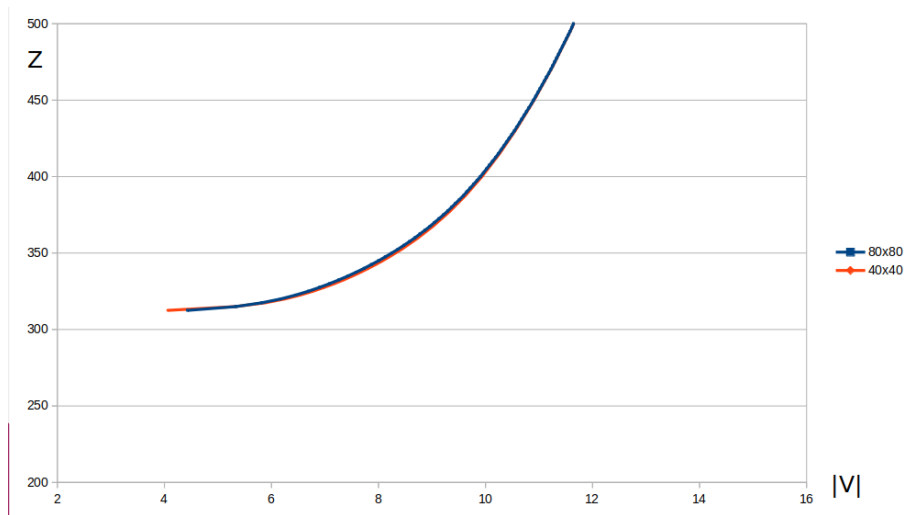


Figure 3.6: Comparison of the wind speed between the 80x80 mesh and the refined 40x40 mesh, zoom up to 500 m

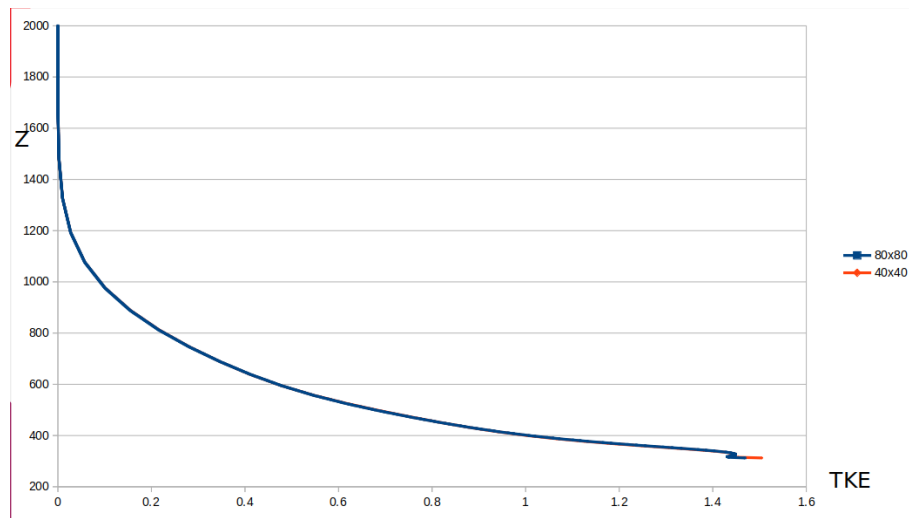


Figure 3.7: Comparison of the turbulent kinetic energy  $k$  between the 80x80 mesh and the refined 40x40 mesh

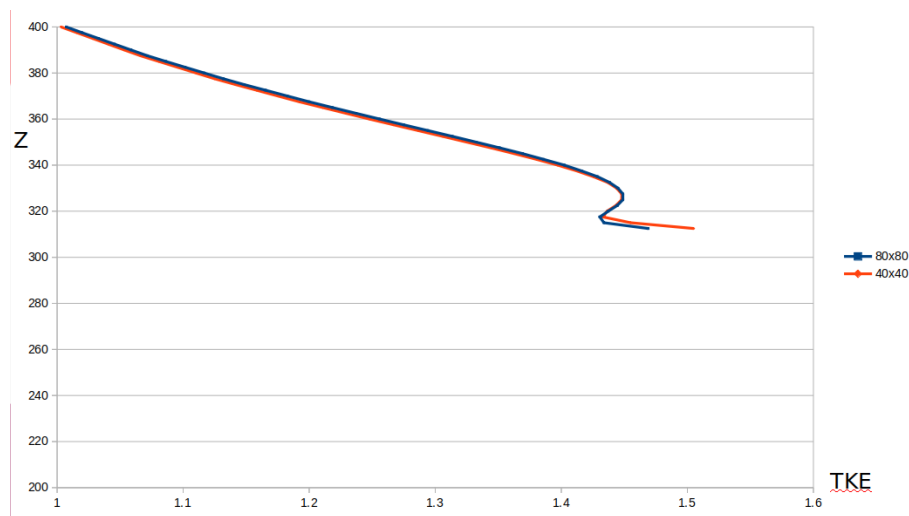


Figure 3.8: Comparison of the wind speed between the 80x80 mesh and the refined 40x40 mesh, zoom up to 400 m

Also the buffer dimension analysis, the transition zone impact the vertical refinement have not highlighted particular differences; small differences can be seen in the cases with the rotated or not rotated mesh in which the

latter has been rotated according to have the mesh about the wind input data direction.

The rotation is not as easy as can seem because the input data of the wind direction of  $115^\circ$  is the geostrophic one, while the mesh has to be rotated at the ground level. To do so a further rotation of  $20^\circ$  is being subtracted to the geostrophic one.

For this particular case-study, also the buffer zone does not impact the results, unlike the most of the other work on this topics: this is due to the fact that, for the wind direction considered, the wind comes from the adjacent lake, a very flat zone, that coincidentally coincides with the flat zone simulated with the buffer, as can be seen in figure 3.9.

Note that the buffer zone is not created according to the real topography, but only to smooth the furthest zone impact. Results are shown in figures 3.10, 3.11 and 3.12.

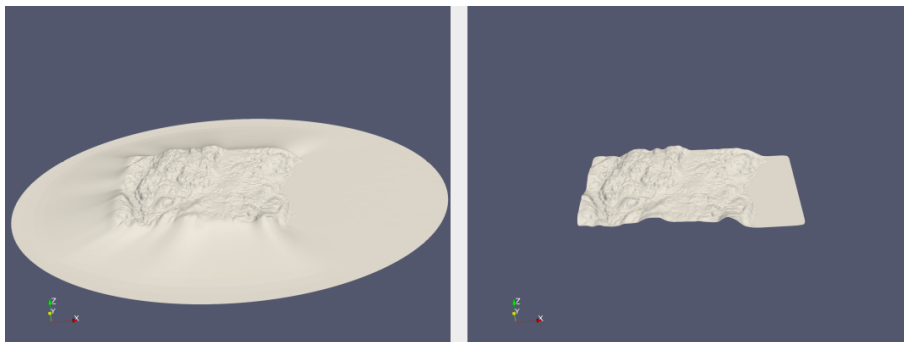


Figure 3.9: Comparison of the simulated zone with and without buffer

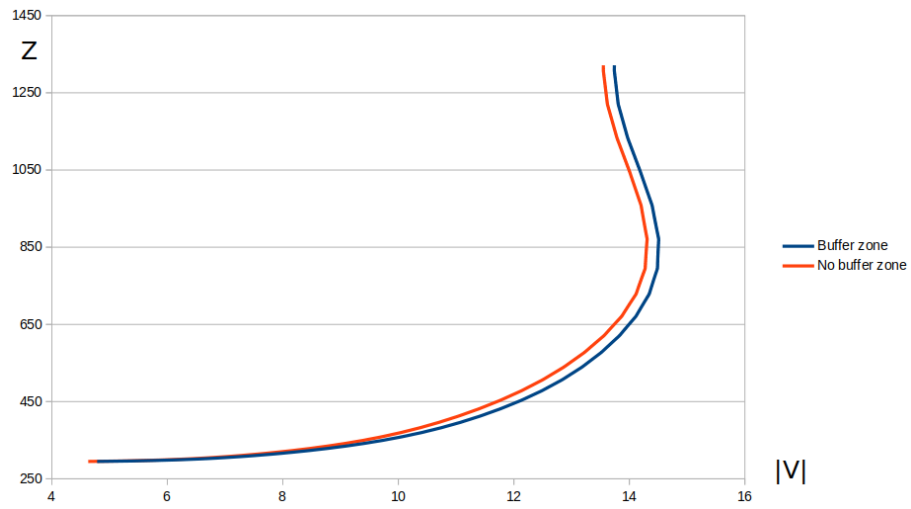


Figure 3.10: Comparison of the wind speed for the simulations with and without buffer

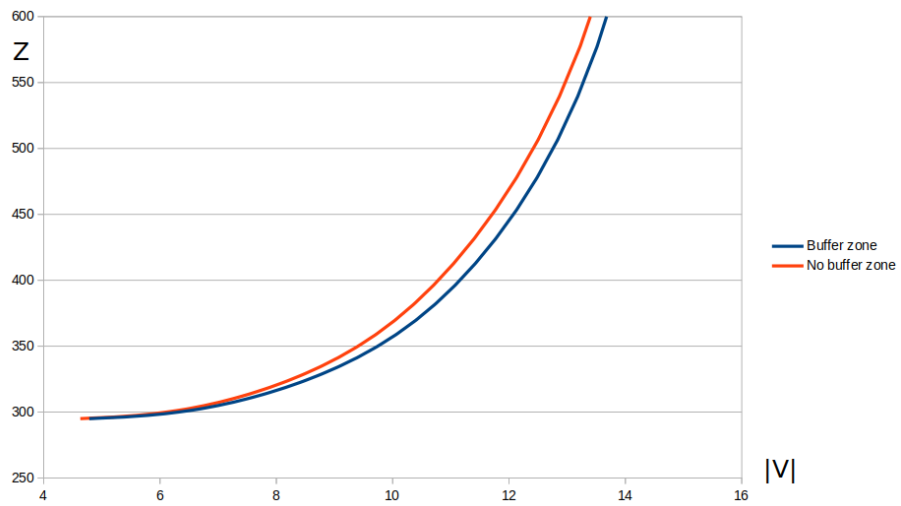


Figure 3.11: Comparison of the wind speed for the simulations with and without buffer, zoom up to 550 m

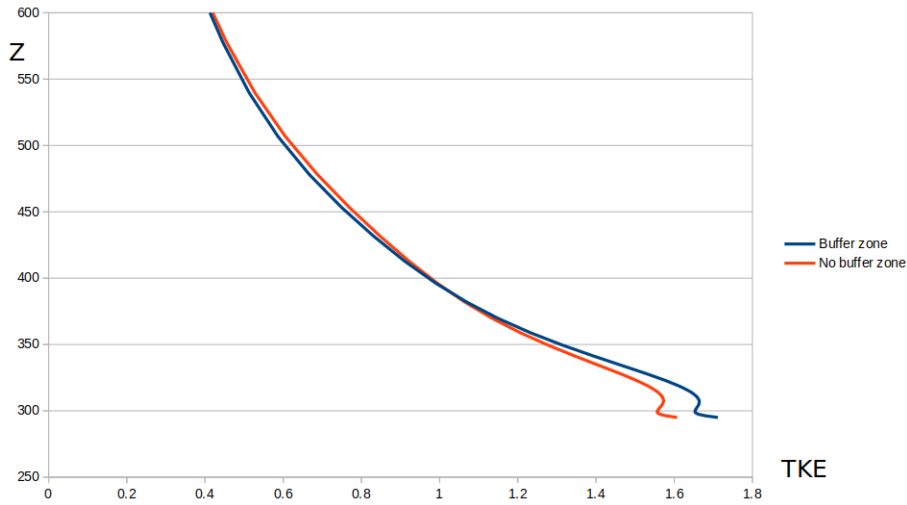


Figure 3.12: Comparison of the turbulent kinetic energy  $k$  for the simulations with and without buffer, zoom up to 600 m

A great difference in the simulation results, instead, can be seen adding the Coriolis effect.

The added Coriolis force,

$$F_c = -2m\omega \times \mathbf{u}$$

has a great influence on the wind profile, with a remarkable rotation between the top and the bottom of the vertical profile both in the speed and in the direction as can be seen in figures 3.13 and 3.14. Moreover we can notice, in figure 3.15 the path of the turbulent kinetic energy that, for high altitude, goes to zero, according to the physical properties. This phenomena does not happens in the case without canopy due to the inconsistency of the closure problem, created ad hoc for the Coriolis case.

For what concern the wind direction, we can easily see the turning of the wind of about  $20^\circ$ , typical of the wind profile.

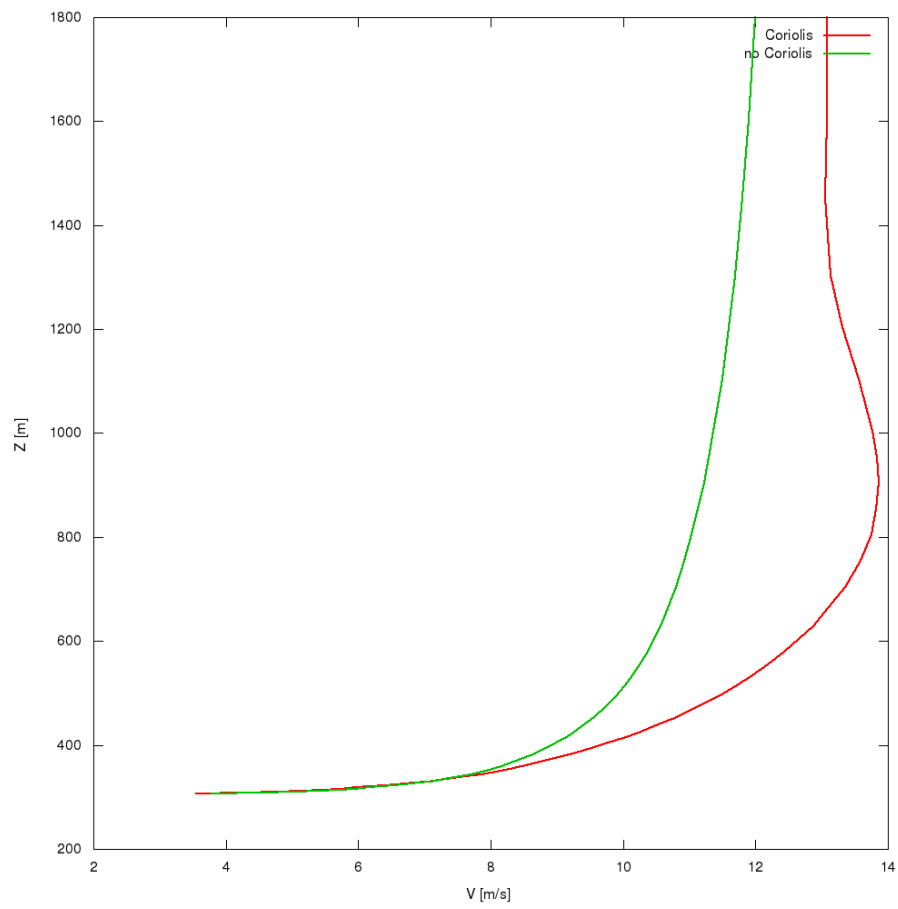


Figure 3.13: Comparison of the wind speed for the simulations with and without Coriolis force

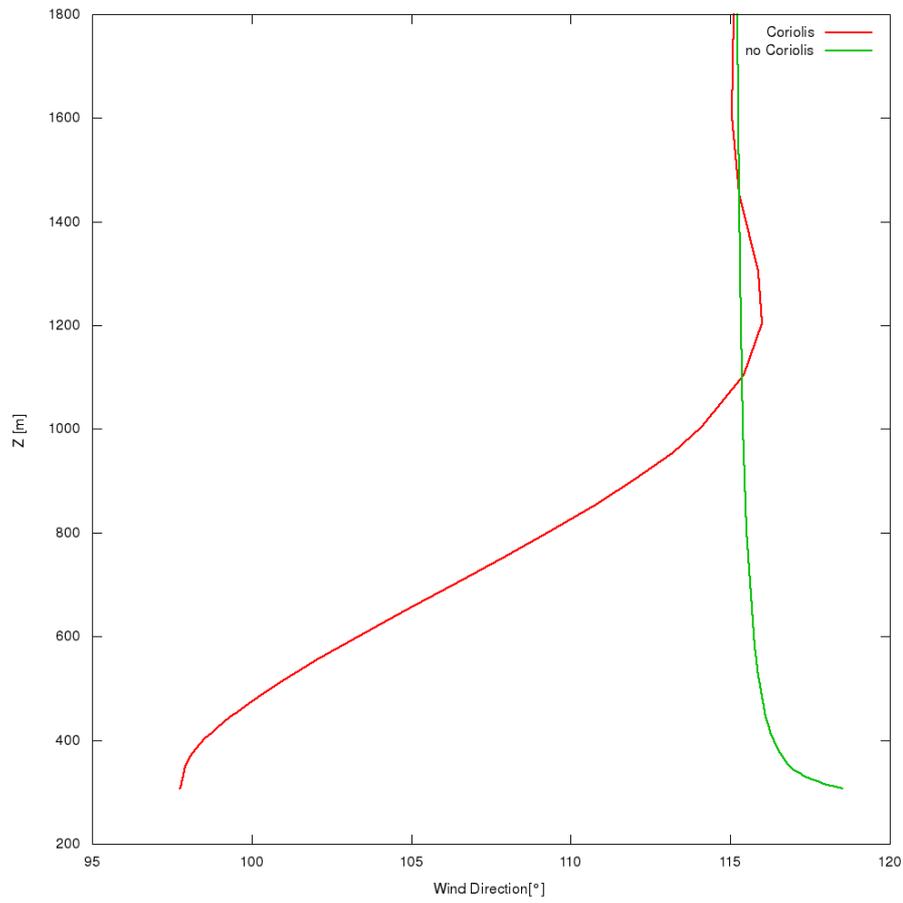


Figure 3.14: Comparison of the wind direction for the simulations with and without Coriolis force

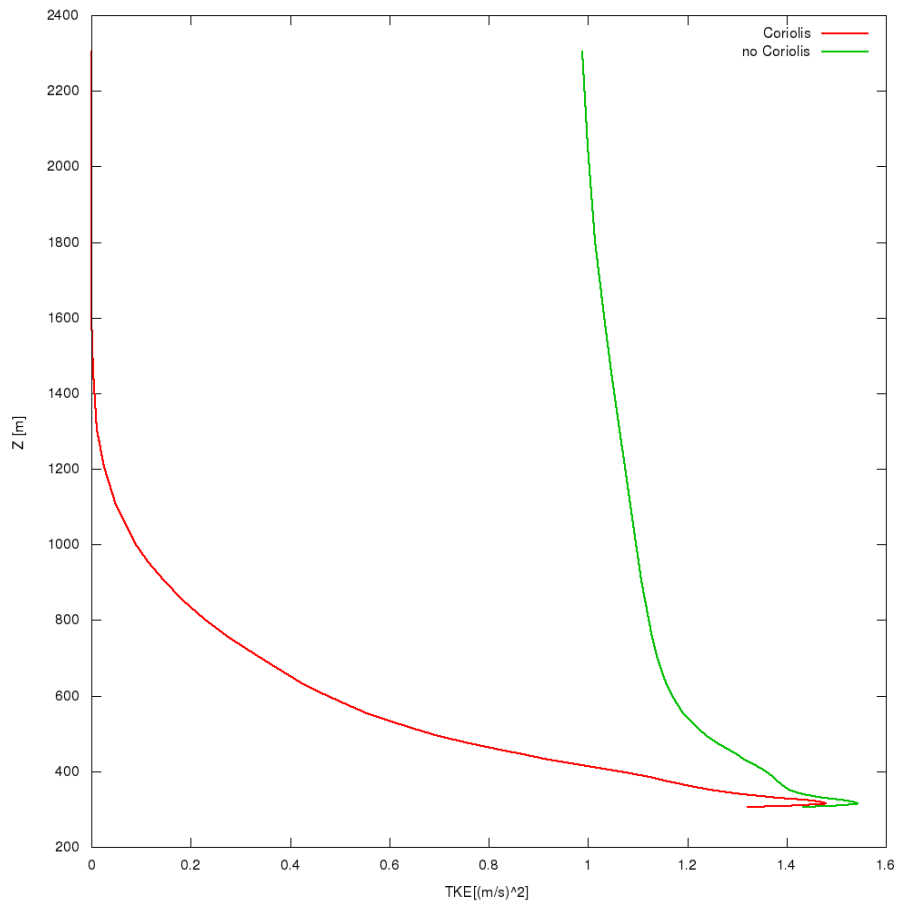


Figure 3.15: Comparison of the turbulent kinetic energy  $k$  for the simulations with and without Coriolis force

## 3.2 Simulations with canopy

After the preliminary simulations without canopy done to study the terrain and topography impact the canopy has been introduced. The canopy height in the zone under study is given as input data and its trend can be seen in the figure 3.16

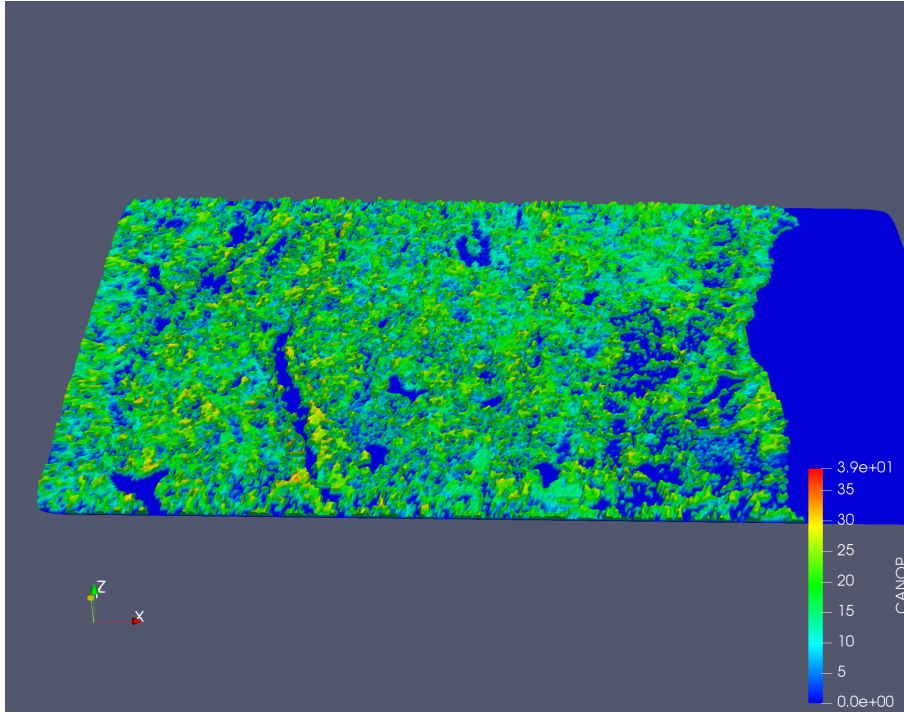


Figure 3.16: Input data of the canopy height in the simulated domain

To introduce it in the equations a drag term proportional to the punctual leaf area density and to the velocity is inserted in the momentum equation:

$$\frac{\partial}{\partial t} \mathbf{u} + \mathbf{u} \cdot \nabla \mathbf{u} = -\nabla \left( \frac{p}{\rho} \right) + \nabla \cdot (\nu_t \nabla^s \mathbf{u}) - 2\omega x \mathbf{u} - C_d LAD |\mathbf{u}| \mathbf{u} \quad (3.1)$$

In the dissipation rate of the turbulent kinetic energy equation, instead, is added a term proportional to the leaf area density, to the speed and to the turbulent kinetic energy:

$$\frac{\partial}{\partial t} \epsilon + \mathbf{u} \cdot \nabla \epsilon = +\nabla \cdot \left( \frac{\nu_t}{\sigma_\epsilon} \nabla \epsilon \right) + \frac{\epsilon}{k} (C_1 P_k - C_2 \epsilon + C_3 C_d LAD |\mathbf{u}| k) \quad (3.2)$$

The canopy input data are given in two different ways:

- Leaf Area Density, that is the density of the punctual point and depends on the height of the profile. It is given in a 10x10 m mesh in the horizontal plane and every 1 m in the vertical direction for more than 4 millions points in total.

Its trend in the height is shown in the figure 3.17. The LAD is given as  $[m^{-1}]$ .

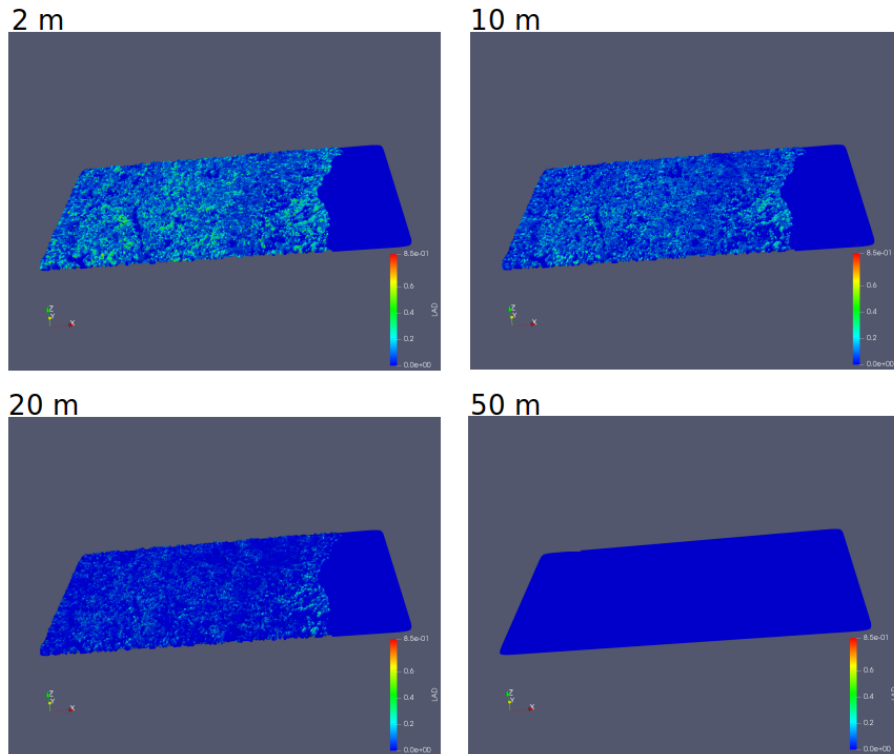


Figure 3.17: Input data of LAD values at different height

- Leaf Area Index, that is obtained from the integration over the height of the canopy of the LAD;

$$LAI = \int_0^{h_{canopy}} LAD$$

It is a much easier data to manage because it does not varies in the vertical profile.

As in the equations the LAD input data is required, when the simulation with the LAI input data were done, a constant shape profile is assumed, and the LAI value influence only its area as can be seen in the figure 3.18. The LAI is given as non dimensional parameter.

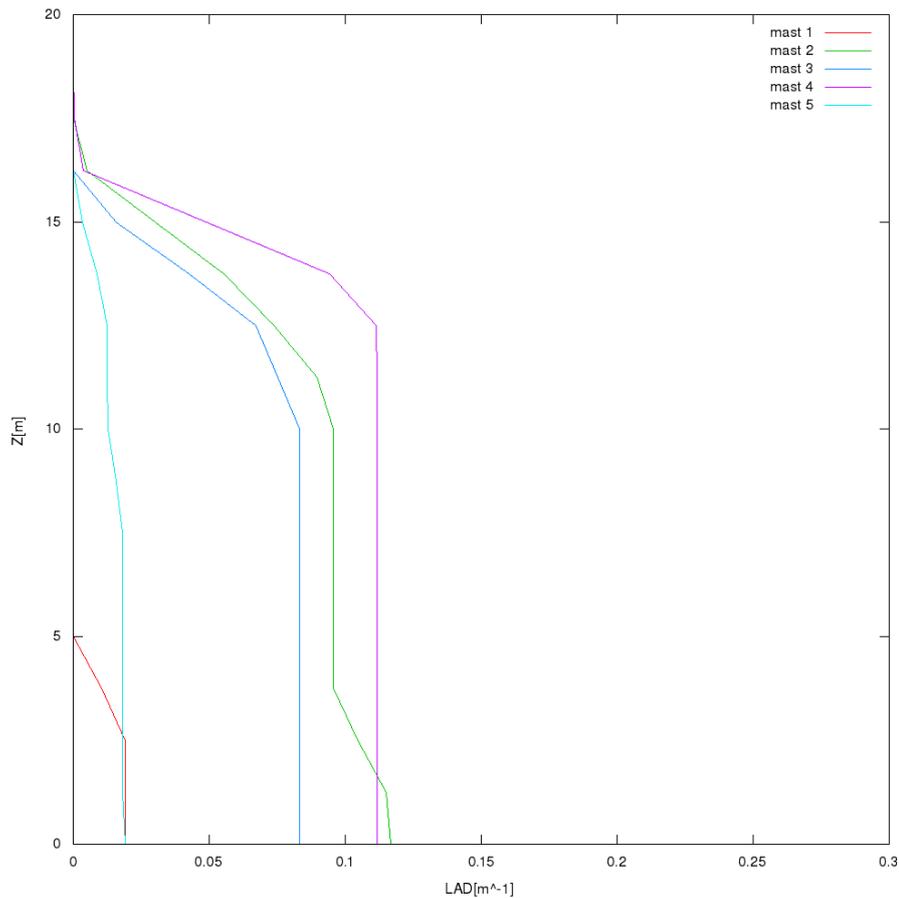


Figure 3.18: input data of the canopy height in the simulated domain

The main parameters studied for the analysis are the canopy impact as first, to see how the canopy affects wind and turbulent kinetic energy profiles; then the impact of using LAD and LAI as input data have been studied together with the buffer impact possibility. The last study has been done using a smoothing approximation for the LAI profile.

The simulations with the canopy presence done in this work are :

- 80x80 mesh, LAI input data without smoothing and without buffer
- 80x80 mesh, LAD input data without smoothing and without buffer
- 80x80 mesh, LAI input data with smoothing and without buffer
- 60x60 mesh, LAI input data without smoothing and without buffer

- 80x80 mesh, LAI input data without smoothing and with buffer
- 40x40 mesh, LAI input data without smoothing and without buffer

Those simulations have been analyzed in two masts, the mast 7 and the mast 3.

### 3.2.1 Mast 7 analysis

The first analysis with the canopy are made in the mast 7, one of the masts with the highest canopy and LAD. This mast has the coordinate of 438028.00 , 6427581.00.

A curious fact is that, comparing the input data given and the recent shape of the canopy in that zone, they seem to be inconsistent as seen in the comparison between figure 3.19,3.20 and 3.21, representing the zone in 2015, 2011 and the input data.

This is due to the fact that in the zone in the last years several cuttings and re-plantings have been made, creating a very heterogeneous canopy profile in all the zone and particularly around the mast 7 here analyzed.

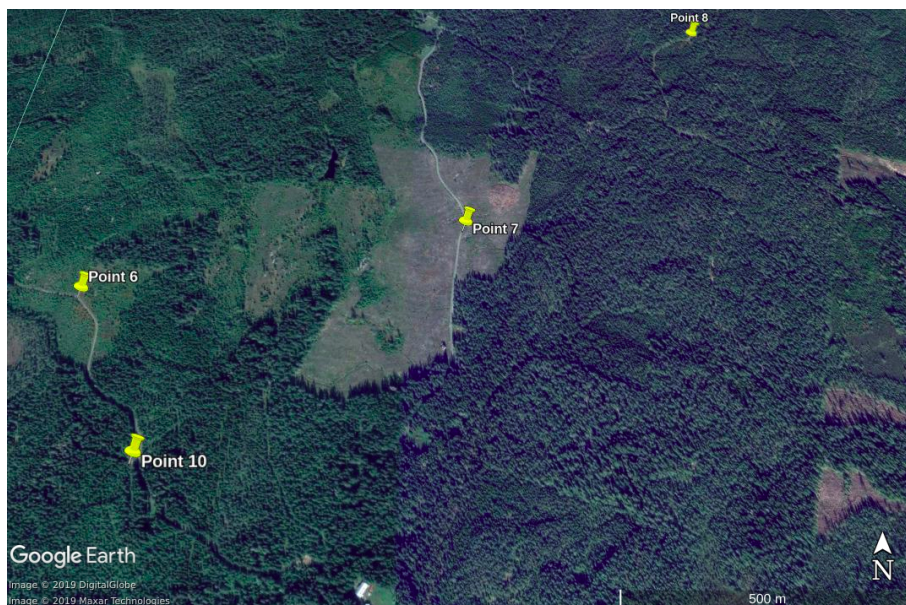


Figure 3.19: Canopy height in mast 7 zone in 2015

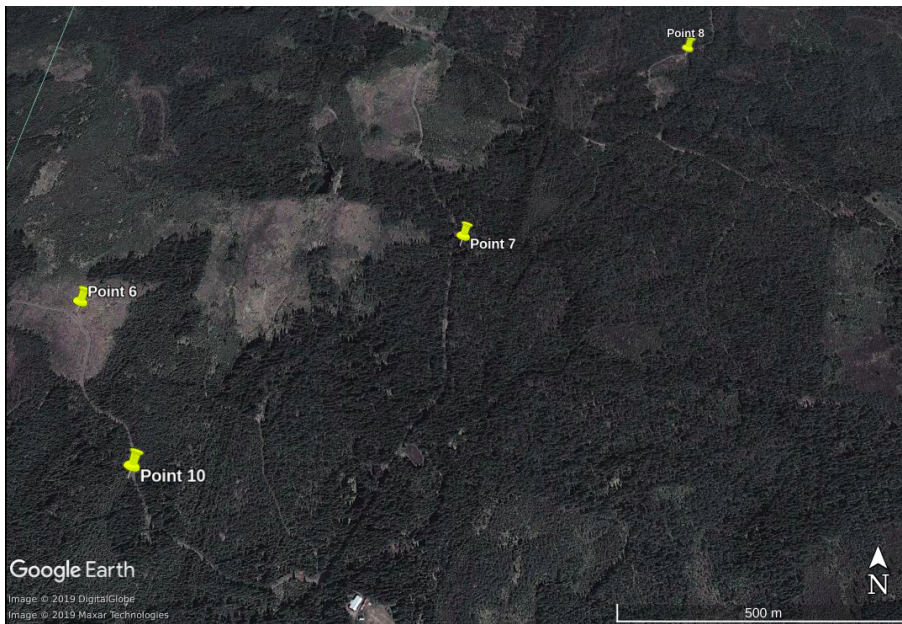


Figure 3.20: Canopy height in mast 7 zone in 2011

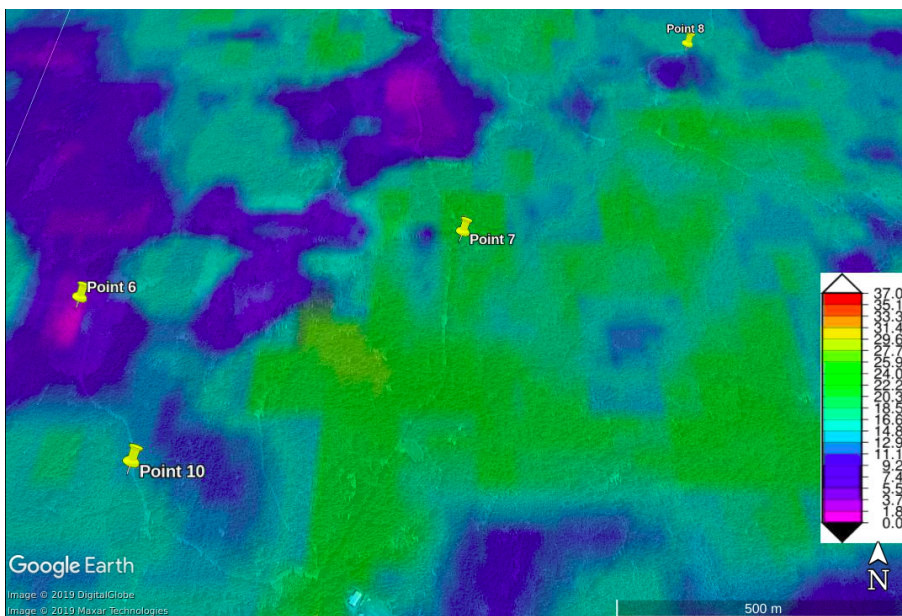


Figure 3.21: Canopy height input data

### 3.2.2 Canopy effect

The first effect analyzed is the effect of the canopy itself, comparing a case with canopy and one without it, without changing other parameters: even if the canopy is around 30 m its effects, as can be seen in the following images, is relevant also outside it. For the turbulent kinetic energy it can be seen in figure 3.22, as expected, a large increase in the values for the canopy case, due to the fact that the canopy acts as an obstacle to the flow of the wind and increases the turbulence.

It is relevant at least until 600 m and where it reaches the maximum value it is around 3 times the normal case.

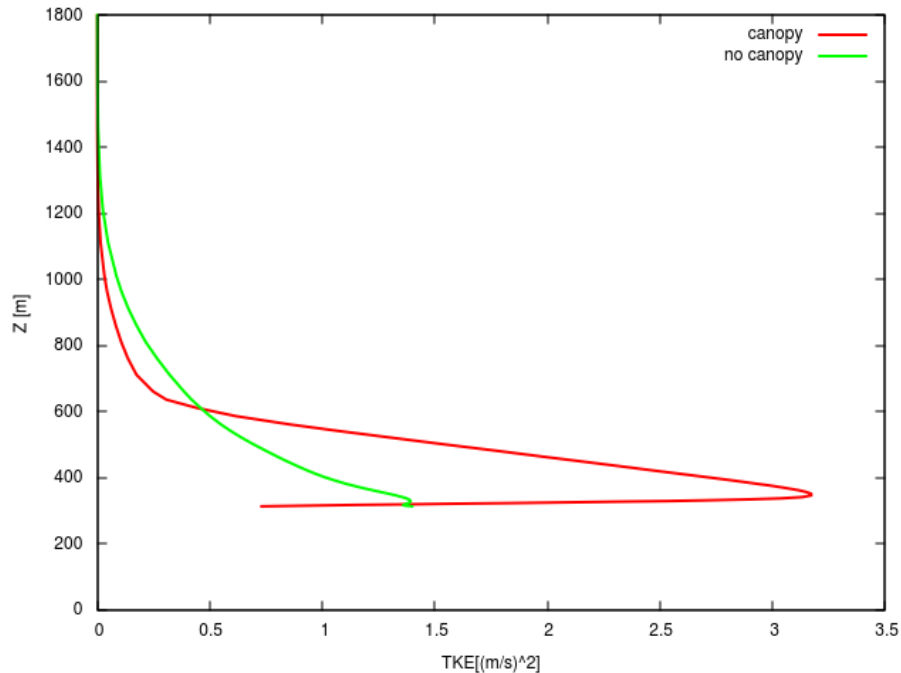


Figure 3.22: TKE profile for simulations with and without canopy

For what concern the wind speed profile, shown in figure 3.23, beyond the difference outside the canopy, the interesting aspect is the decrease of the wind speed in the canopy case (from  $4\text{ m/s}$  to less than  $2\text{ m/s}$ ) due to the drag force exerted by the canopy itself.

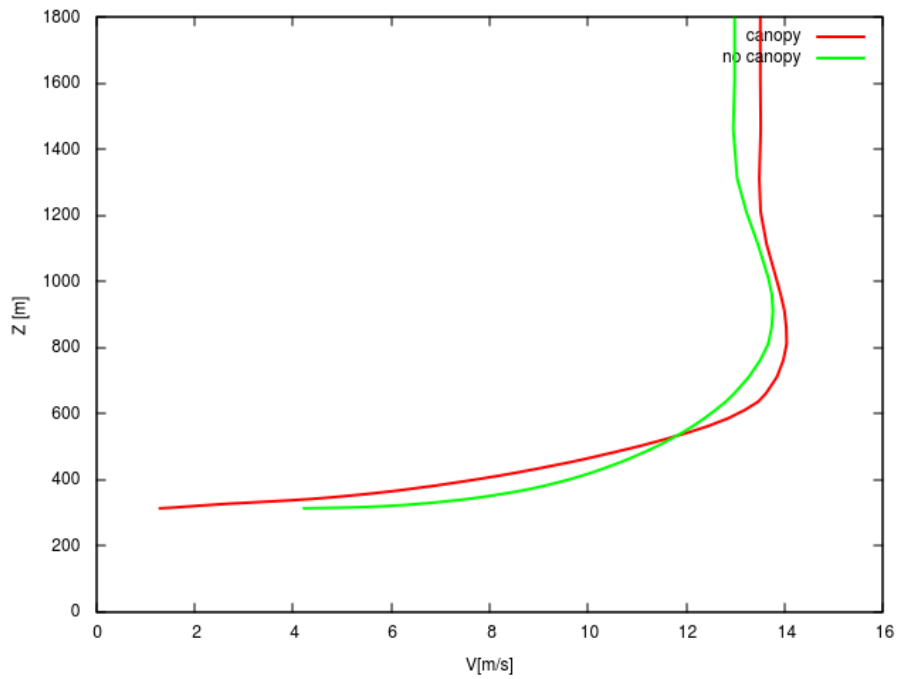


Figure 3.23: Wind speed profile for simulations with and without canopy

Also for the wind direction the main parameter is the drag force that decrease the turning of the wind in the height profile, as shown in figure 3.24:

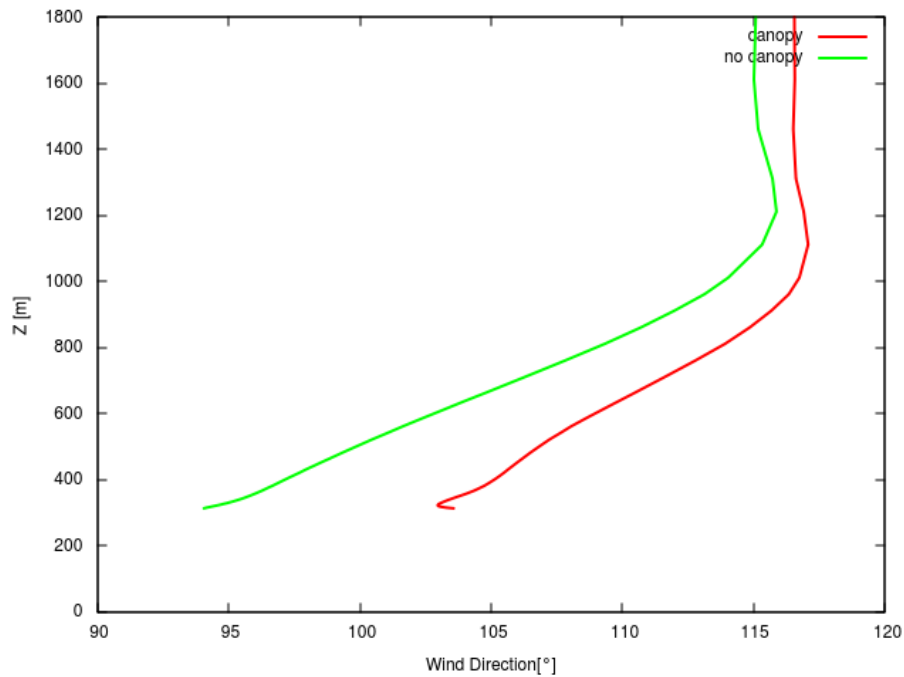


Figure 3.24: Wind direction profile for simulations with and without canopy

### 3.2.3 Mesh refinement

A mesh refinement analysis has been developed with the added canopy in order to figure out the maximum mesh size, that guarantee lower computational cost, that has the same results of a finer mesh. The meshes compared are the square one of 80 m and the square one with 40 m.

As it will be analyzed better later, the higher resolution and the noisiness of the input data in respect to the resolution of the simulating data introduce a sort of randomness in the comparing different mesh resolutions. For the finer mesh:

- The turbulent kinetic energy in the mesh refinement shows an increased value inside the canopy as shown in figure 3.25

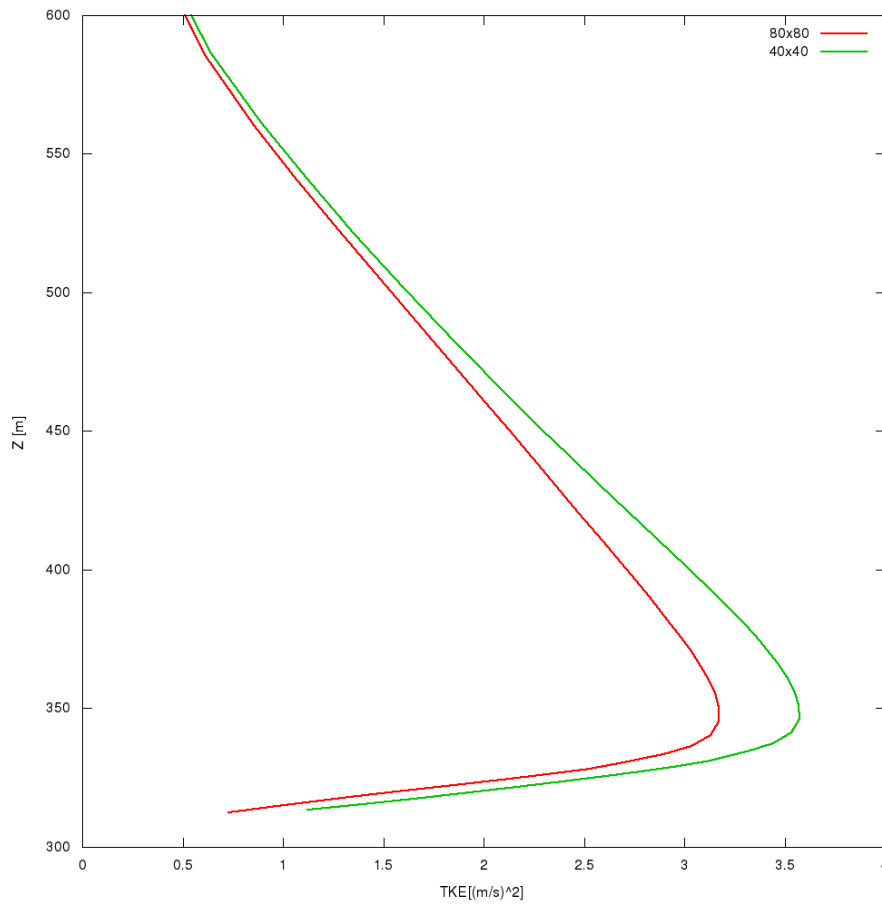


Figure 3.25: TKE profile for simulations for normal and refined mesh

- For what concern the wind speed the two profiles are quite the same and, as you can see in figure 3.26, there is an evident difference only outside the canopy

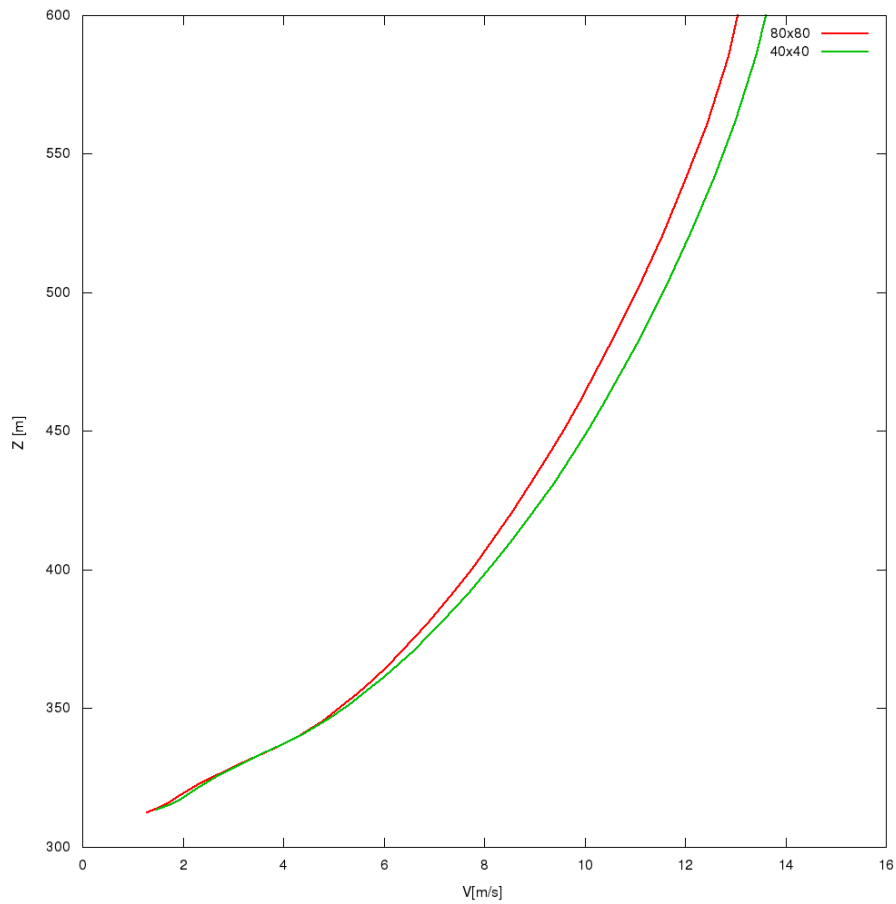


Figure 3.26: Wind speed profile for simulations for normal and refined mesh

- The wind direction behaviour is the most peculiar one: inside the canopy, in fact, as shown in figure 3.27, the mesh refined profile has a turning in the opposite direction in respect to the one in the normal mesh simulation. This will be analyzed better later.

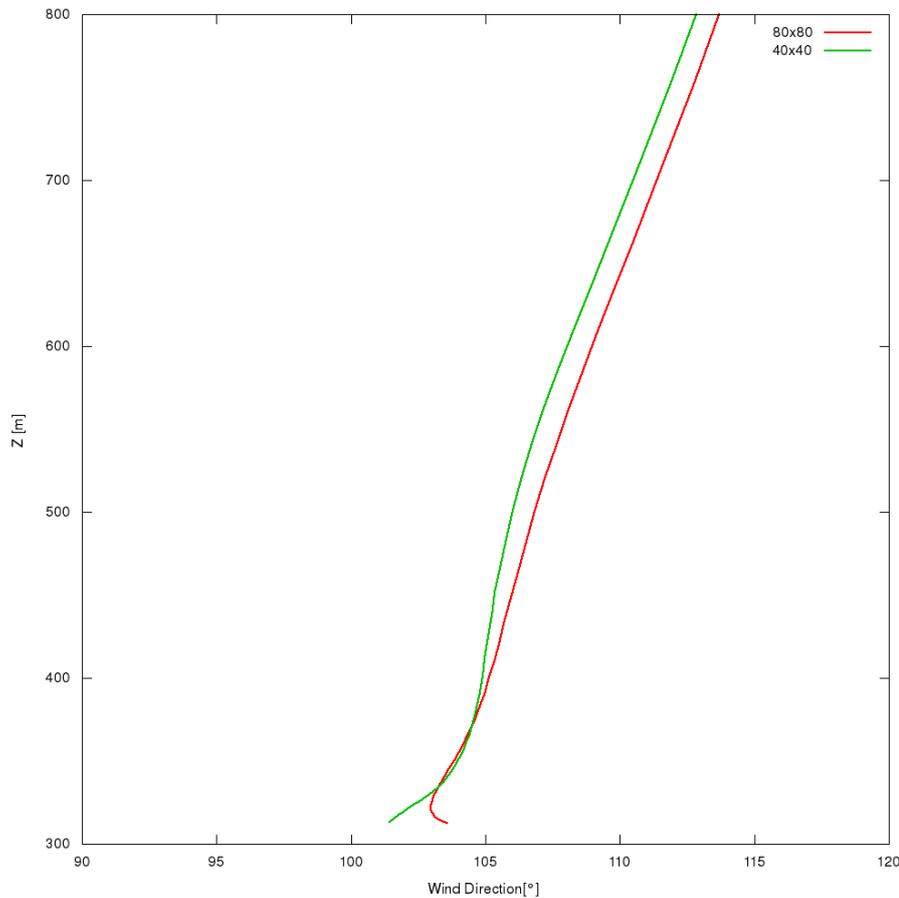


Figure 3.27: Wind direction profile for simulations for normal and refined mesh

### 3.2.4 Buffer effect

Added the canopy as input data, a study of the comparison of the buffer effect on the simulation has been done. The buffer zone is a zone of the region where a flat terrain has been added in order to smooth the surrounding over the zone under study. This is done to accommodate the inflow BCs and to avoid recirculation at the outflow boundary. In figure 3.28 and 3.29 are shown the simulated area for the case with buffer and the one without it.

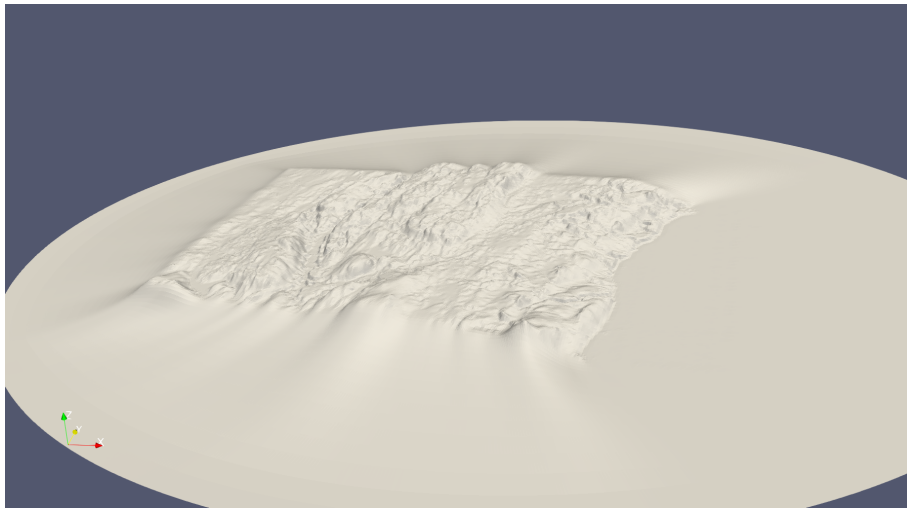


Figure 3.28: Simulated zone with buffer

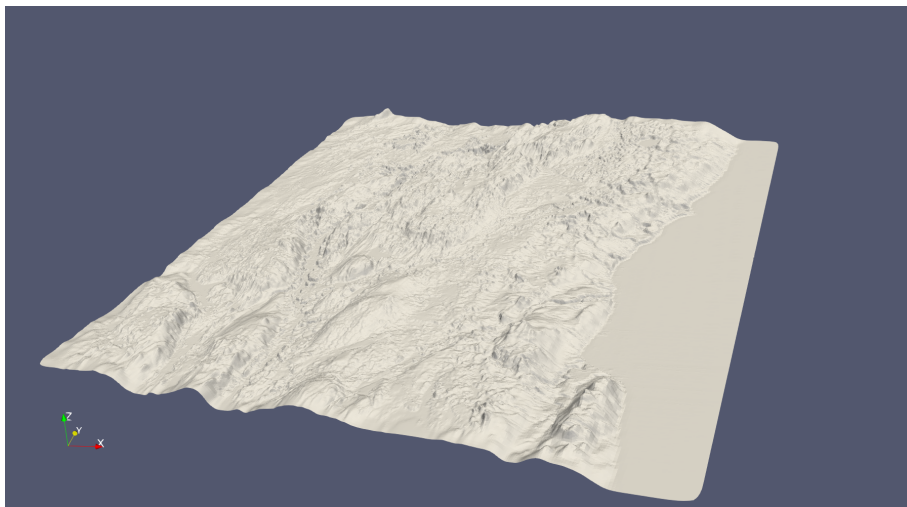


Figure 3.29: Simulated zone without buffer

As can be seen in figures 3.30, the adding of the buffer zone affects the boundaries of the farm zone directly under study ( or better of the transition zone) and change the shape of the topography.



Figure 3.30: Impact of buffer on the boundaries of the farm zone

This is particularly important in the input zone along the wind direction, where a change in the topography cause a change in the trend of the wind. Note that even if the buffer mesh is much coarser in respect to the farm one, its presence increase the computational cost.

For what concern the simulation outputs the presence of the buffer has a visible impact only outside the canopy for what concern the wind speed and direction, while it is relevant inside the canopy for the turbulent kinetic energy.

Note that analyzing the turbulent kinetic energy outside the canopy is quite useless because it is due by the canopy itself and by the terrain.

Remember also that for this case study the buffer effect has a little impact mostly due to the fact that the wind comes from the lake, that a buffer simulate quite good because it is a flat zone; it modifies only the zone in

contact to the lake, smoothing it.

In the figures 3.31, 3.32, 3.33, 3.34, 3.35 and 3.36 the simulation results for the turbulent kinetic energy, the wind speed, the wind direction and their zoom in the first 500 m are shown:

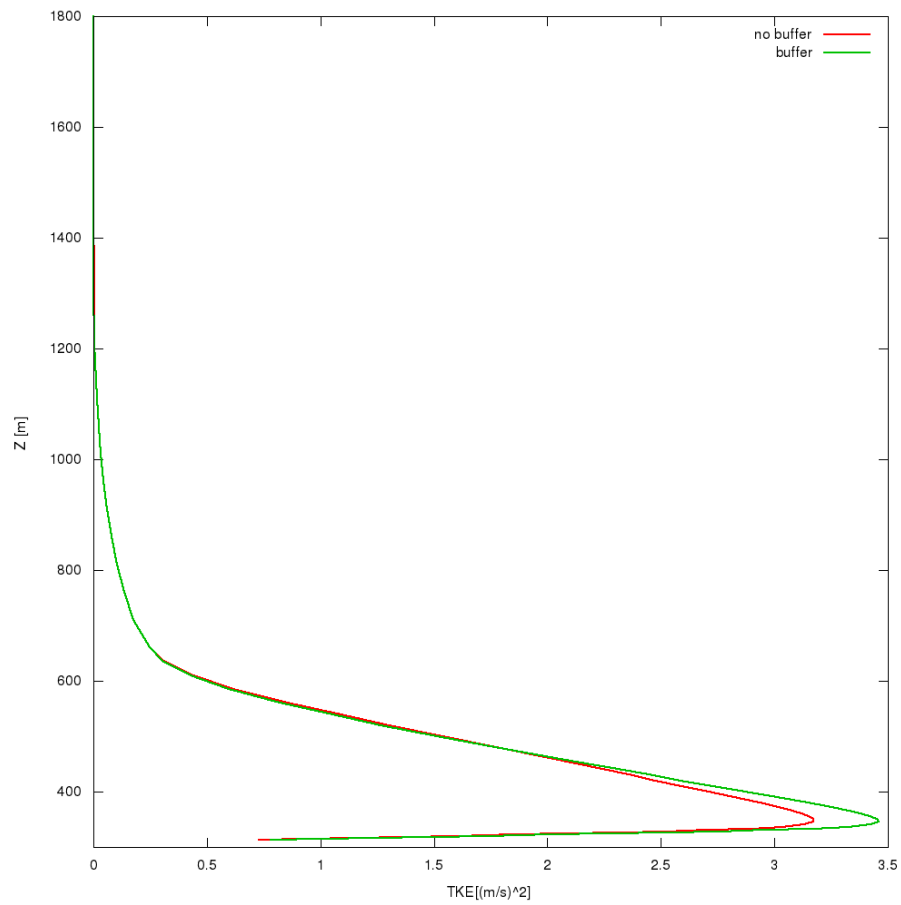


Figure 3.31: TKE profiles for simulations with and without buffer

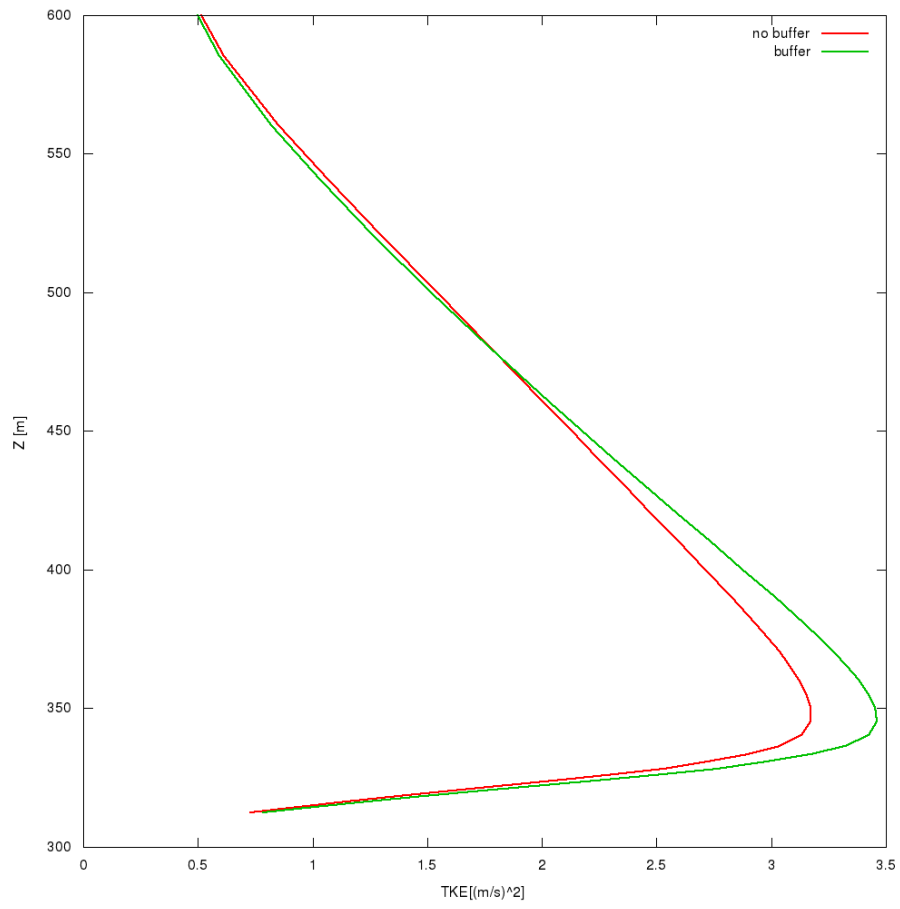


Figure 3.32: Zoom of TKE profiles for simulations with and without buffer

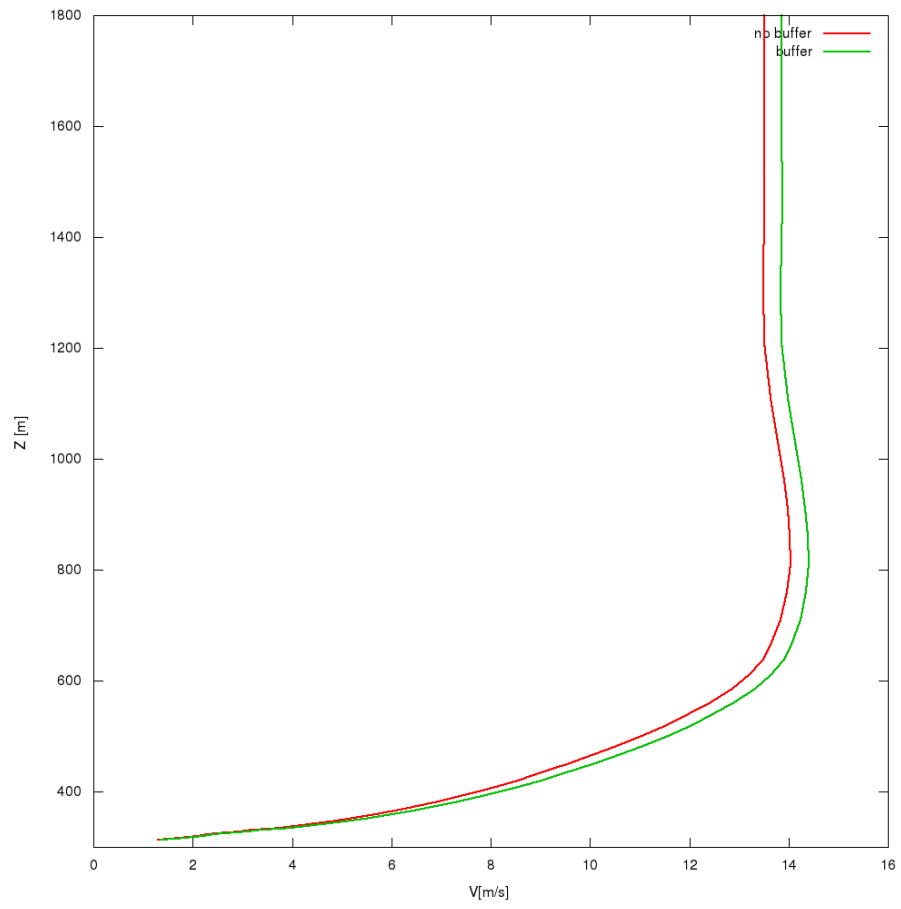


Figure 3.33: Wind speed profiles for simulations with and without buffer

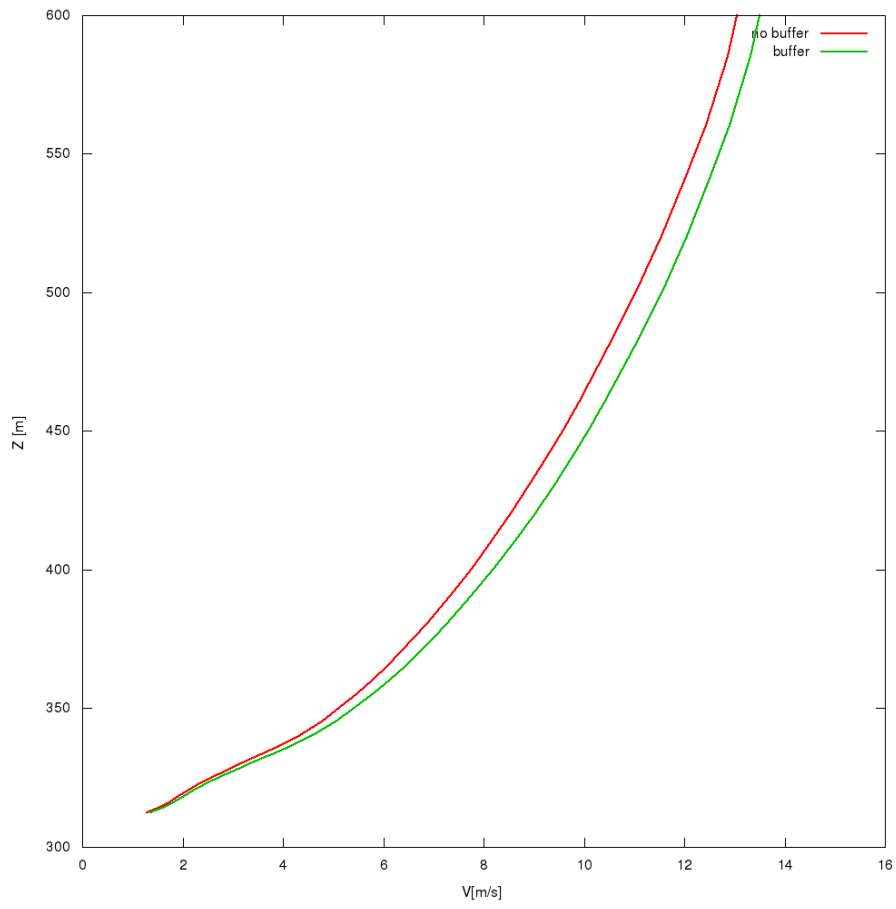


Figure 3.34: Zoom of wind speed profiles for simulations with and without buffer

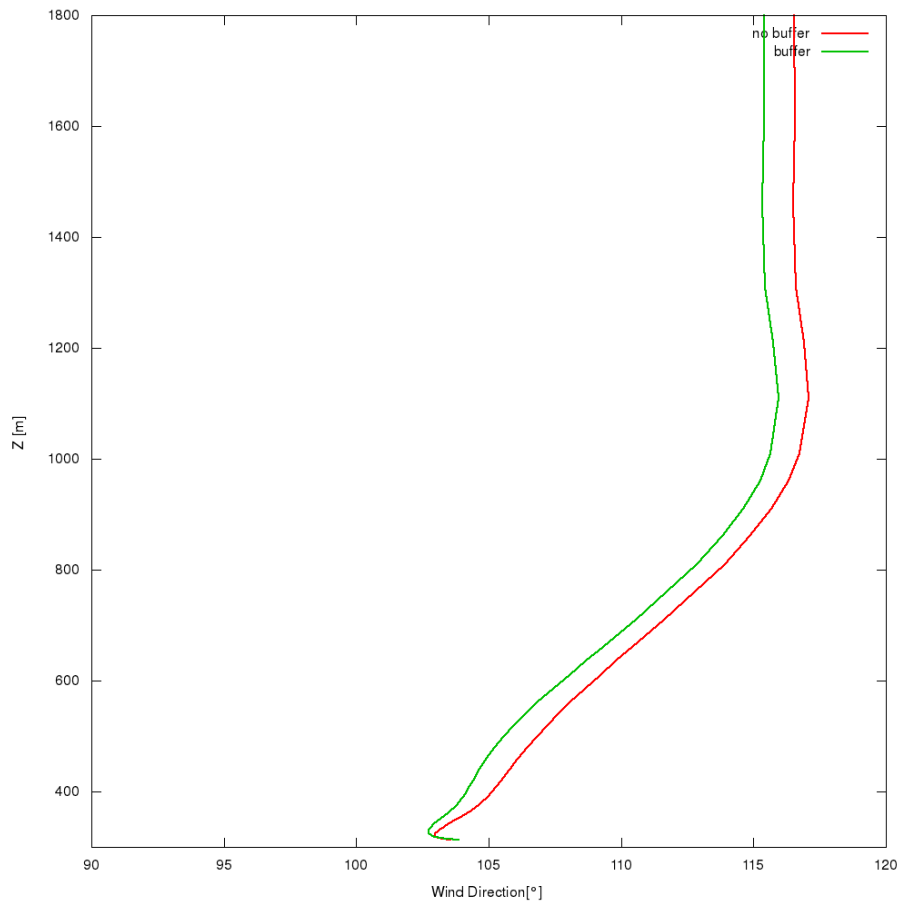


Figure 3.35: Wind direction profiles for simulations with and without buffer

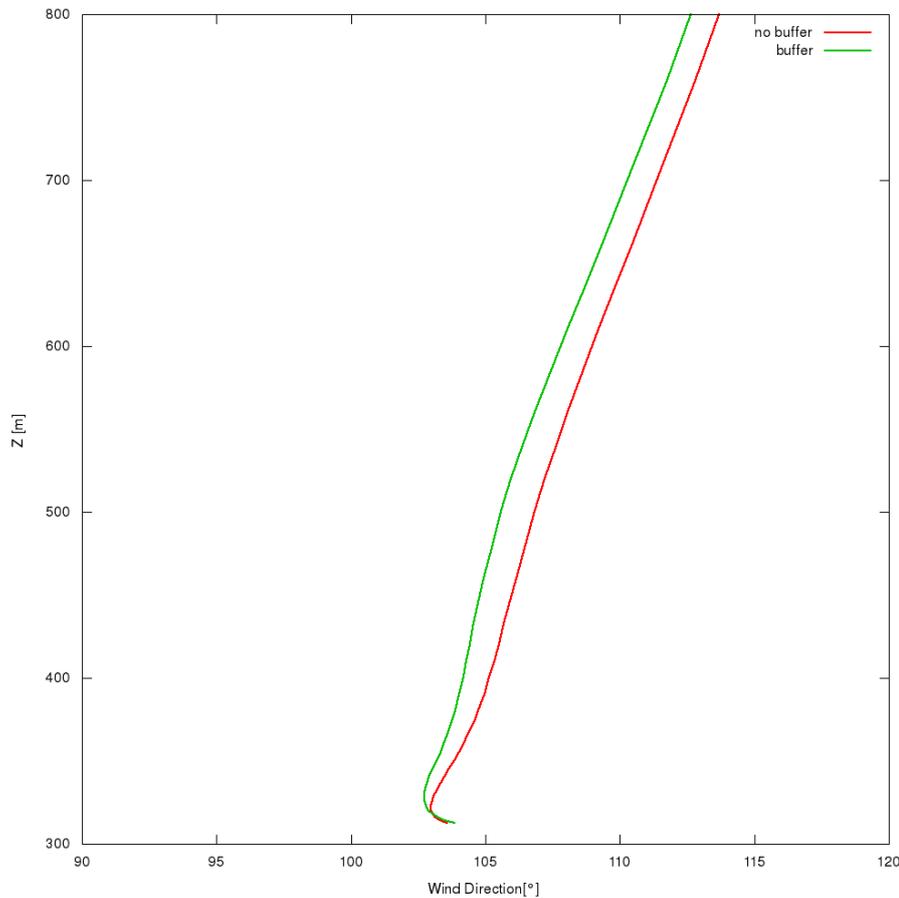


Figure 3.36: Zoom of wind direction profiles for simulations with and without buffer

### 3.2.5 LAI and LAD impact

This analysis has the purpose to take in consideration the effect of the different possibilities as input data: the LAD and LAI. This is done in order to understand if the difference in the wind and turbulent kinetic energy profiles for the two cases are small enough to consider the LAI data, much lighter than LAD due to the fact that it does not change with height. The profiles of the LAI and LAD in the case of mast 7 can be seen in figure 3.37, where we can notice a very noisy vertical profile for the LAD data:

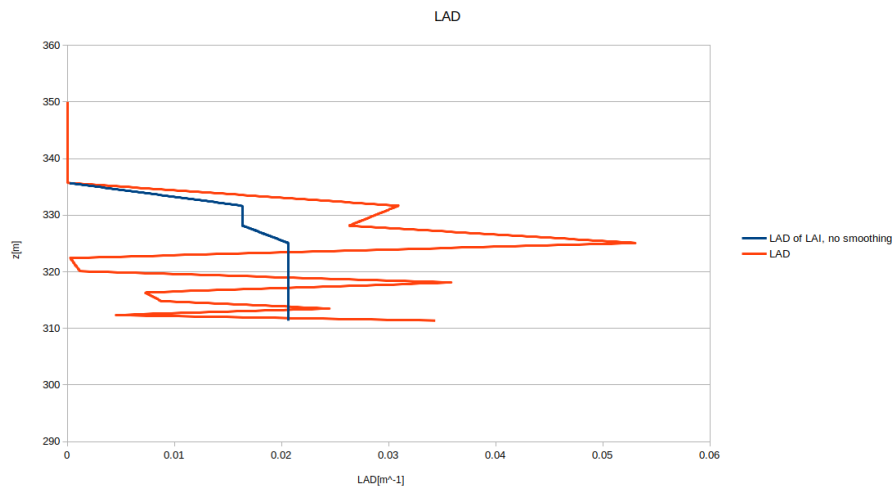


Figure 3.37: Comparison in the LAD vertical profile between LAD and LAI input data

In the analysis of the results of the simulations for those input data, almost all the profile differences are negligible; in fact:

- For the Turbulent kinetic energy there is a small difference only inside the canopy, in which the LAD simulations witness a lower value as can be seen in figure 3.38 and especially 3.39 where it is zoomed the lowest part of the vertical profile.

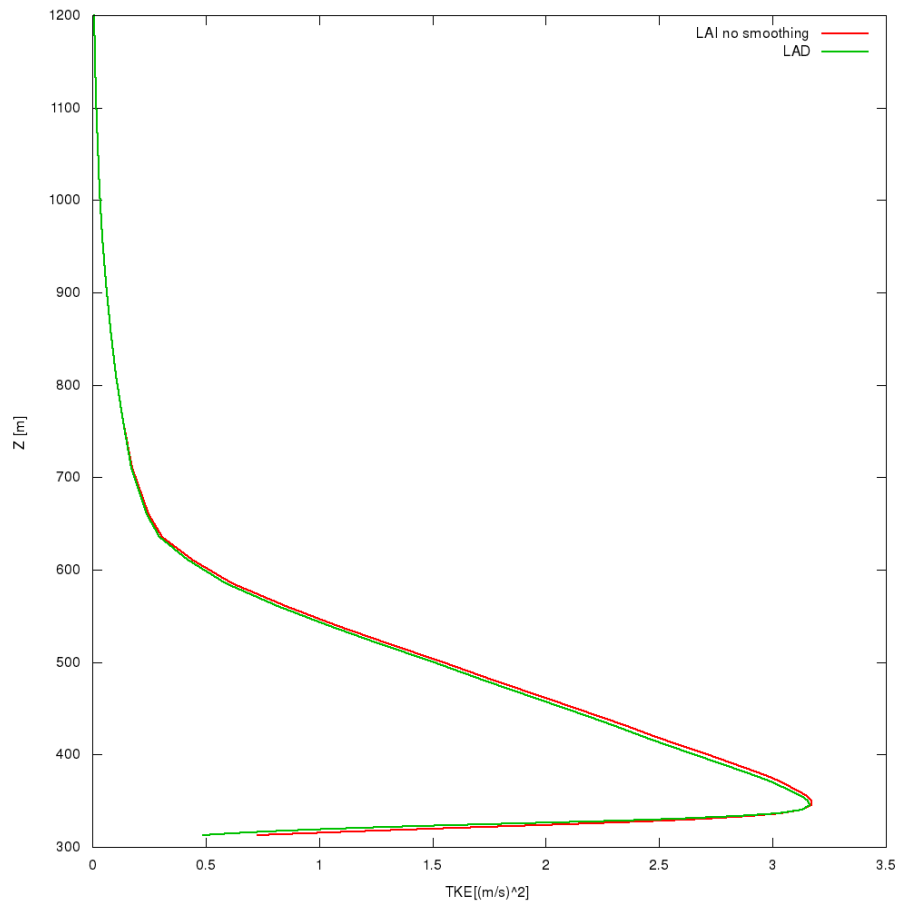


Figure 3.38: TKE profile comparison between LAI and LAD input data

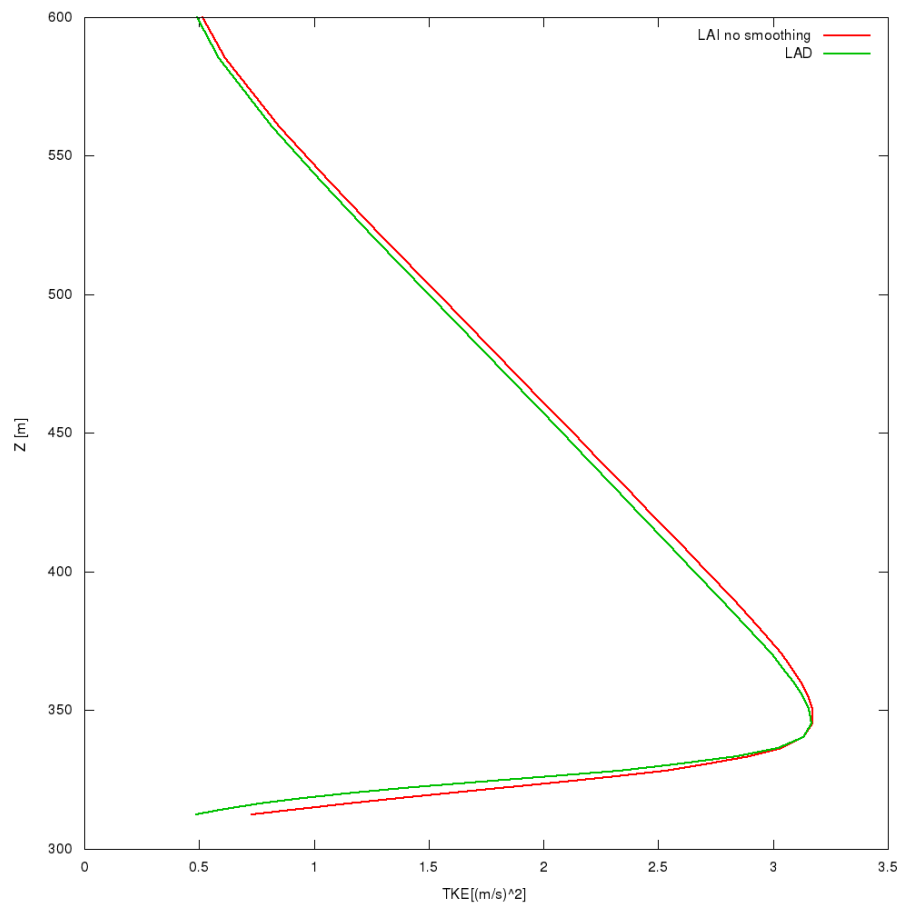


Figure 3.39: TKE profile zoom in the lower zone between LAI and LAD input data

- The wind speed differences can be neglected as shown in figures 3.40 and 3.41:

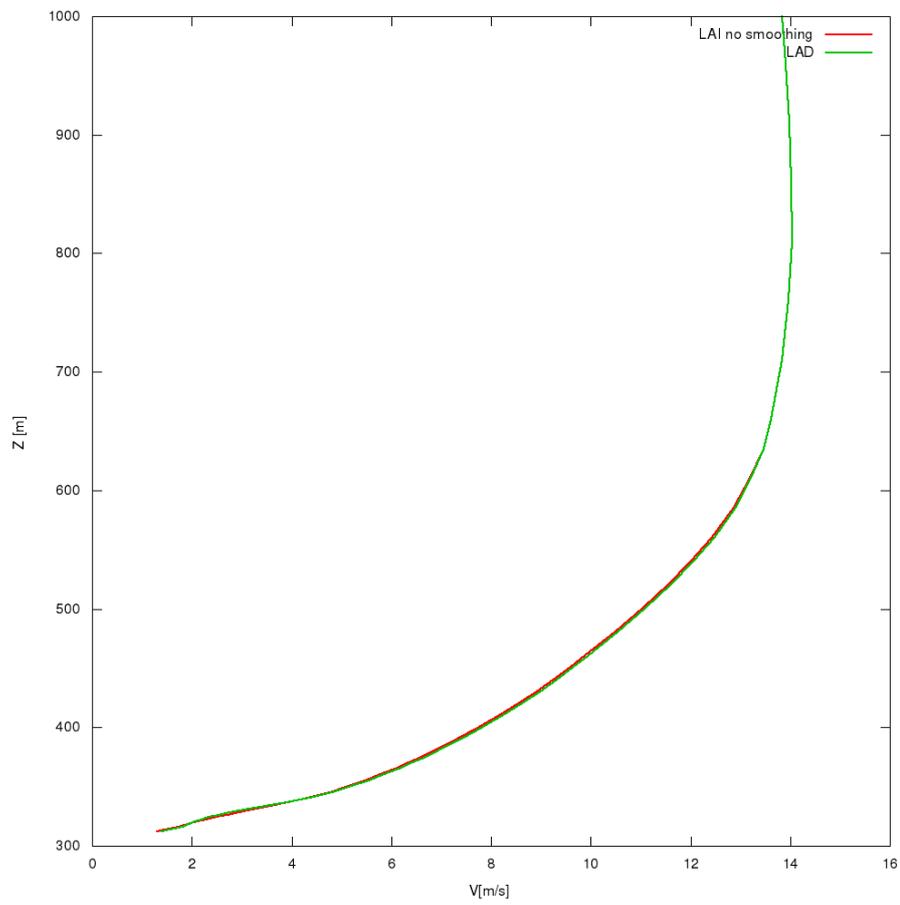


Figure 3.40: Wind speed profile comparison between LAD and LAI input data

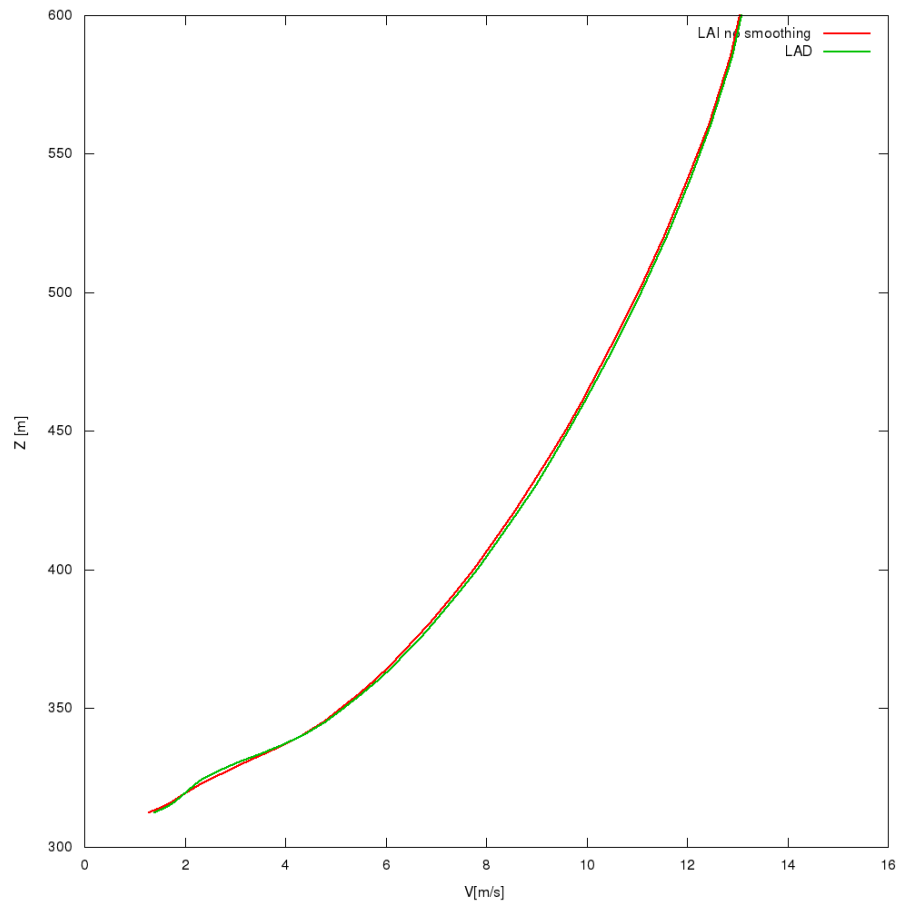


Figure 3.41: Wind speed zoom in the lower zone between LAD and LAI input data

- The LAD simulation witness an higher rotation, with maximum value of about  $5^\circ$  as shown 3.42:

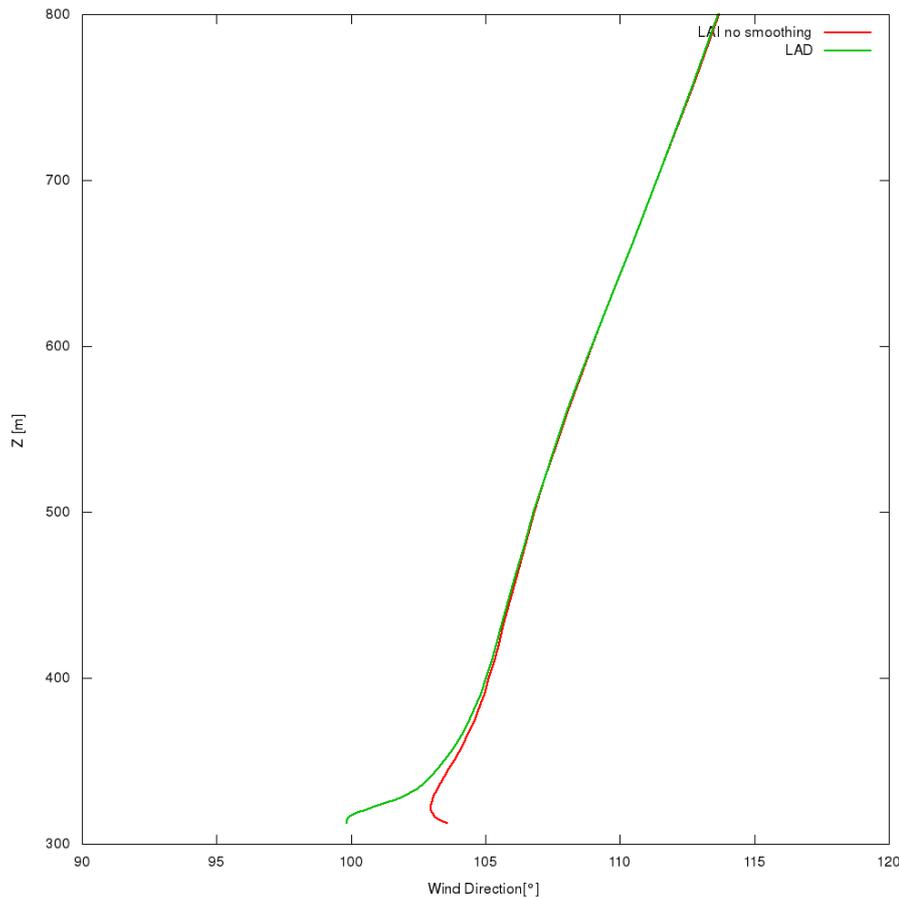


Figure 3.42: Wind direction profile comparison between LAI and LAD input data

### 3.2.6 Smoothing effect on LAI

In order to simplify and lighten the computational cost, a smoothing simplification on the LAI has been made.

This analysis has been done following Observed and modeled near-wake flow behind a solitary tree, (E. Dellwik et al.,2018) [6], a paper in which is showed how the increased resolution of a solitary tree has no improved improvements in the simulation of the wind profile; on the contrary, instead, an exaggerated increase in the resolution affects negatively the study, as well as increasing the computational costs and problem complexity.

In this thesis, a very rough approximation has been made for the LAI smoothing:

- In the point where LAI is zero it remains zero also for the smoothing
- In the point where LAI is different from zero, in the smoothed simulations it takes the value of 0.1, whatever it is its real value.

This is an early stage and very rough approximation but it will be shown, despite those drawbacks, how the effects on the wind study are negligible with respect to the decreased computational cost. For the mast 7 case, the smoothed LAD is much higher than the actual one, as shown in figure 3.43:.

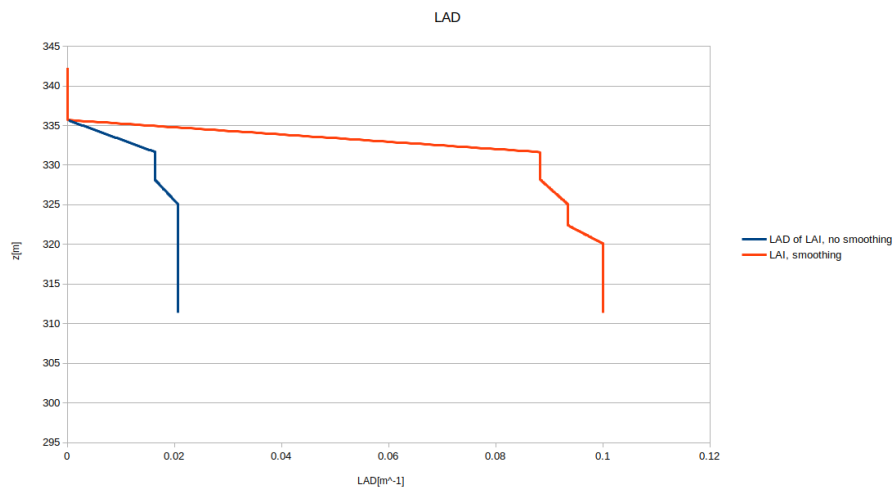


Figure 3.43: Comparison between the LAI actual value and the smoothed one

Due to this increased value it follows that:

- The turbulent kinetic energy for the smoothed case is lower than the actual one due to the higher LAI considered, as figures 3.44 and 3.45 show:

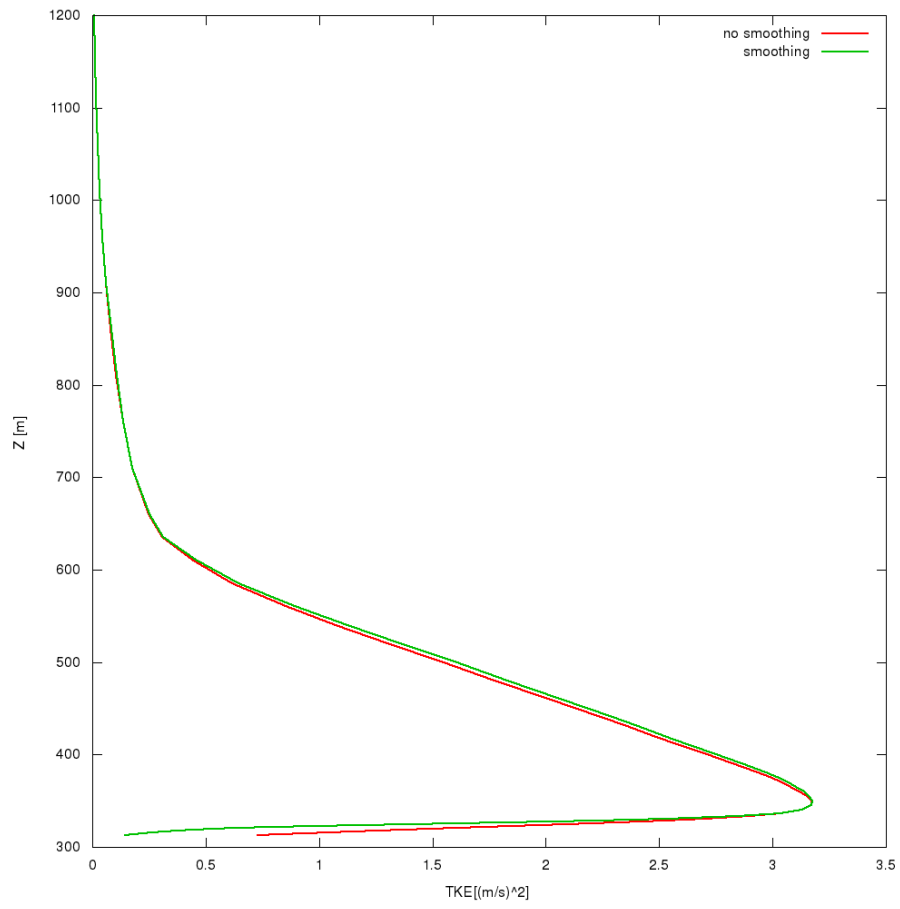


Figure 3.44: TKE profile comparison between actual value and smoothed one

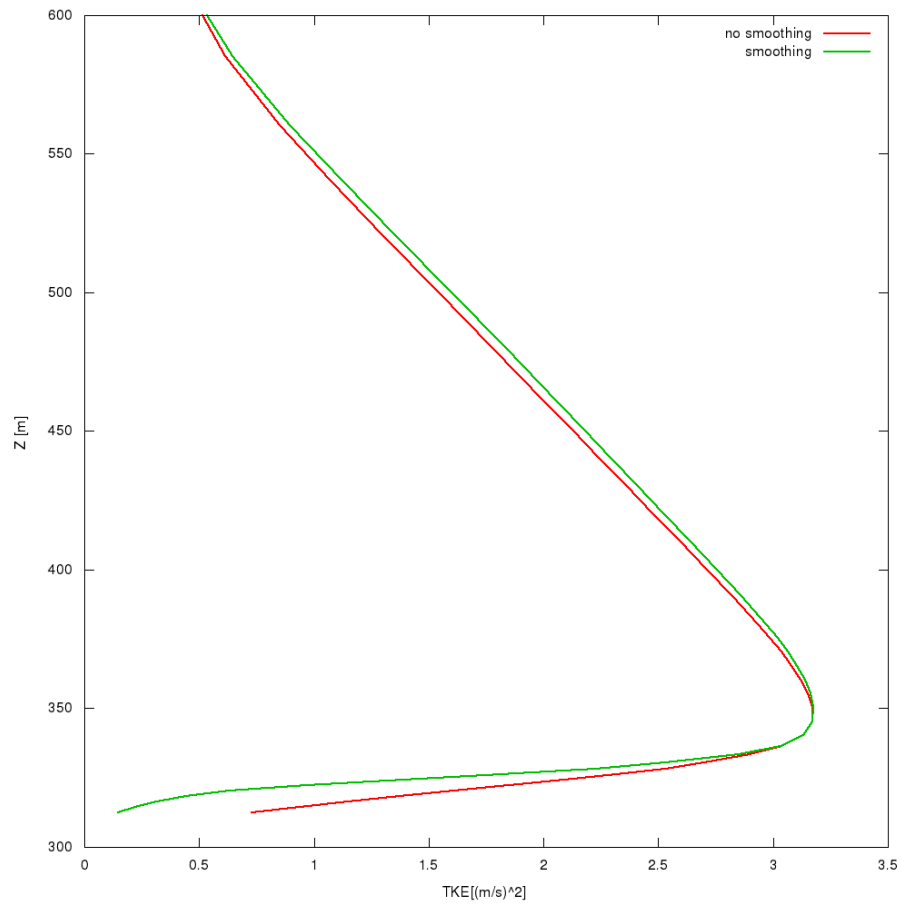


Figure 3.45: TKE profile zoom in the lower zone between actual value and smoothed one

- The wind speed is also lower for the smoothed case, especially inside the canopy and immediately above it, as shown in figures 3.46 and 3.47:

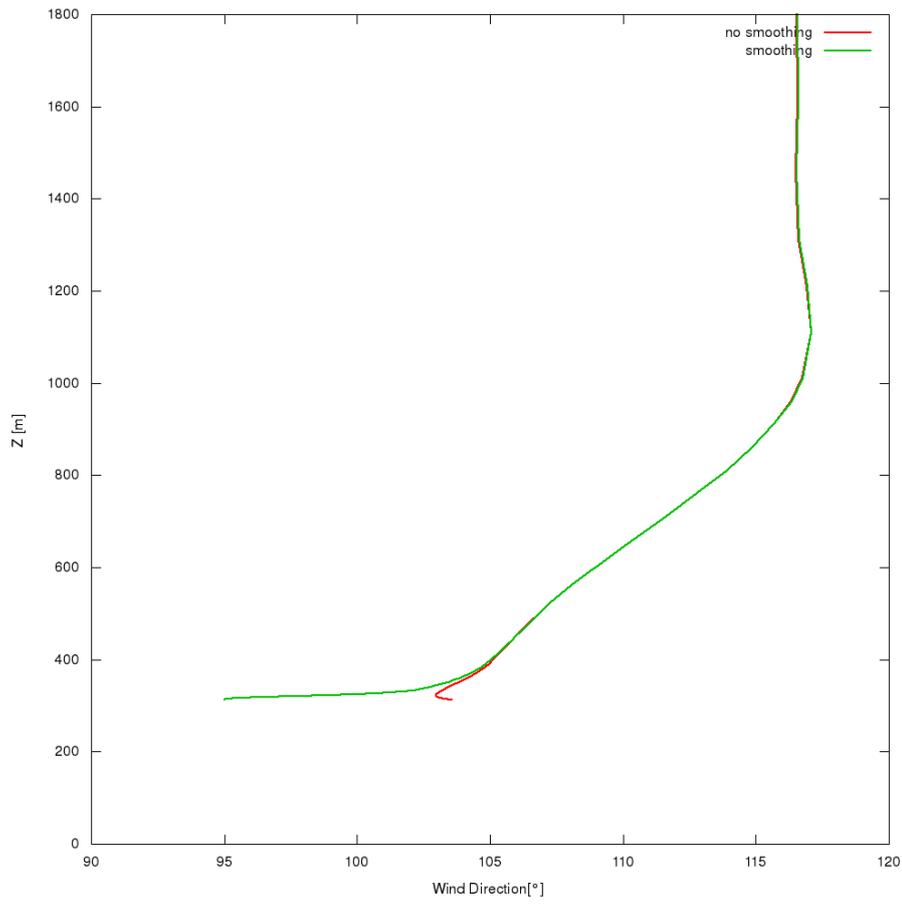


Figure 3.46: Wind speed profile comparison between actual value and smoothed one

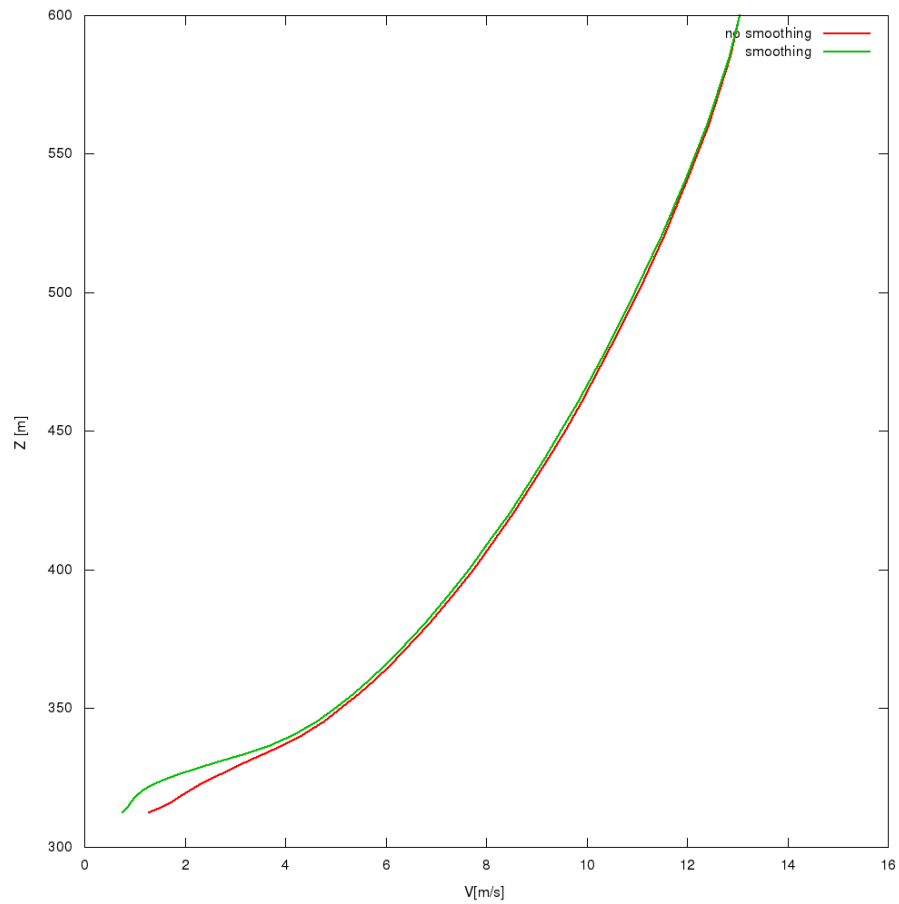


Figure 3.47: Wind speed zoom in the lower zone between actual value and smoothed one

- You witness an increased rotation for the wind profile, especially in the lower part of the profile, directly affected by the canopy presence as shown in figure 3.48:

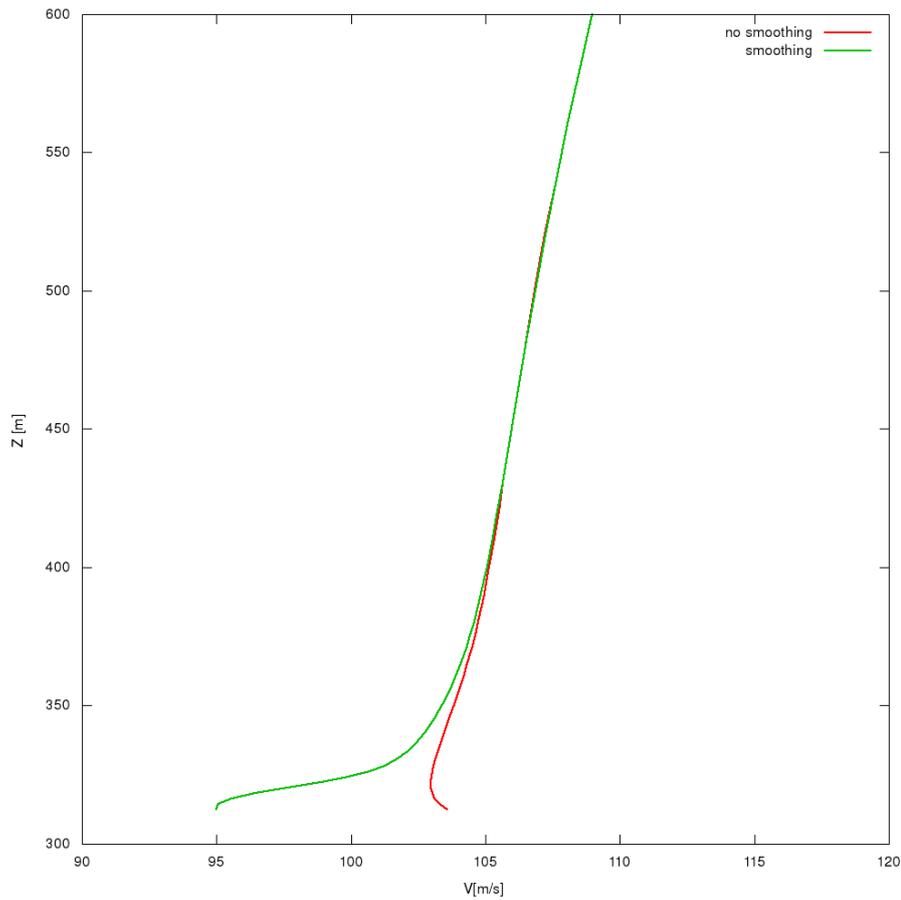


Figure 3.48: Wind direction profile comparison between actual value and smoothed one

### 3.2.7 Comparison between smoothed LAI and LAD

In order to have a complete overview on the theme, a comparison between the most computational demanding simulation, the one with LAD, and the minor applicant for the numerical cost one, the one with LAI, has been developed.

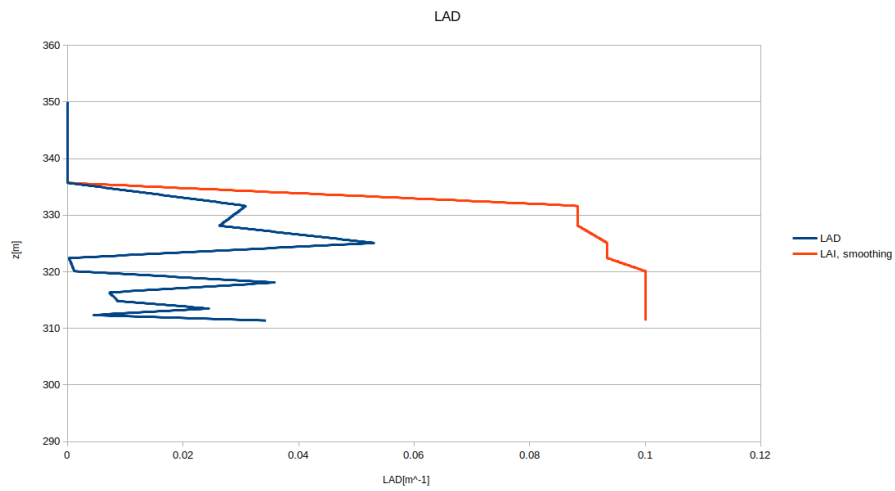


Figure 3.49: Comparison between smoothed LAI values and LAD values

The smoothed value, as shown in figure 3.49, is much higher than the real input one given as input. For this reason, as for the comparison done between smoothed and real LAI, we witness:

- A lower TKE for the smoothed case in the region inside the canopy, as seen in figures 3.50 and 3.51, even if the maximum value is less than  $0.5m/s^2$  and an small increase of TKE in the region above the canopy

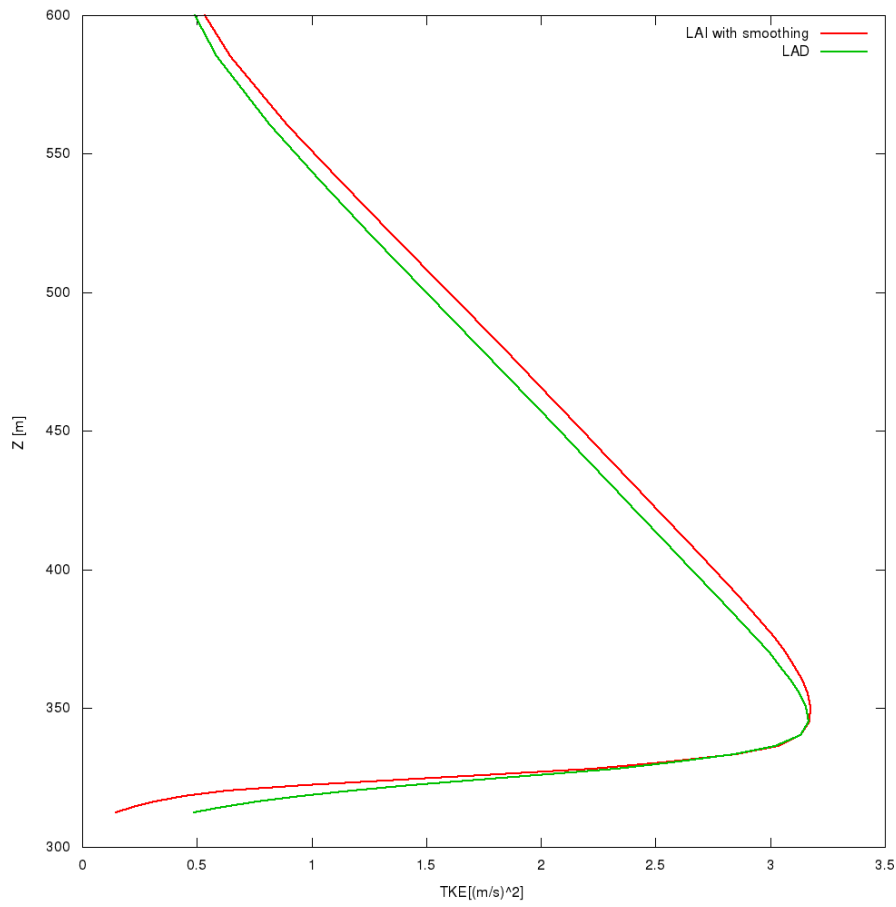


Figure 3.50: TKE profiles for smoothed LAI simulation and LAD one

- A lower wind speed inside the canopy can be seen in figure 3.51 always due to this increased value

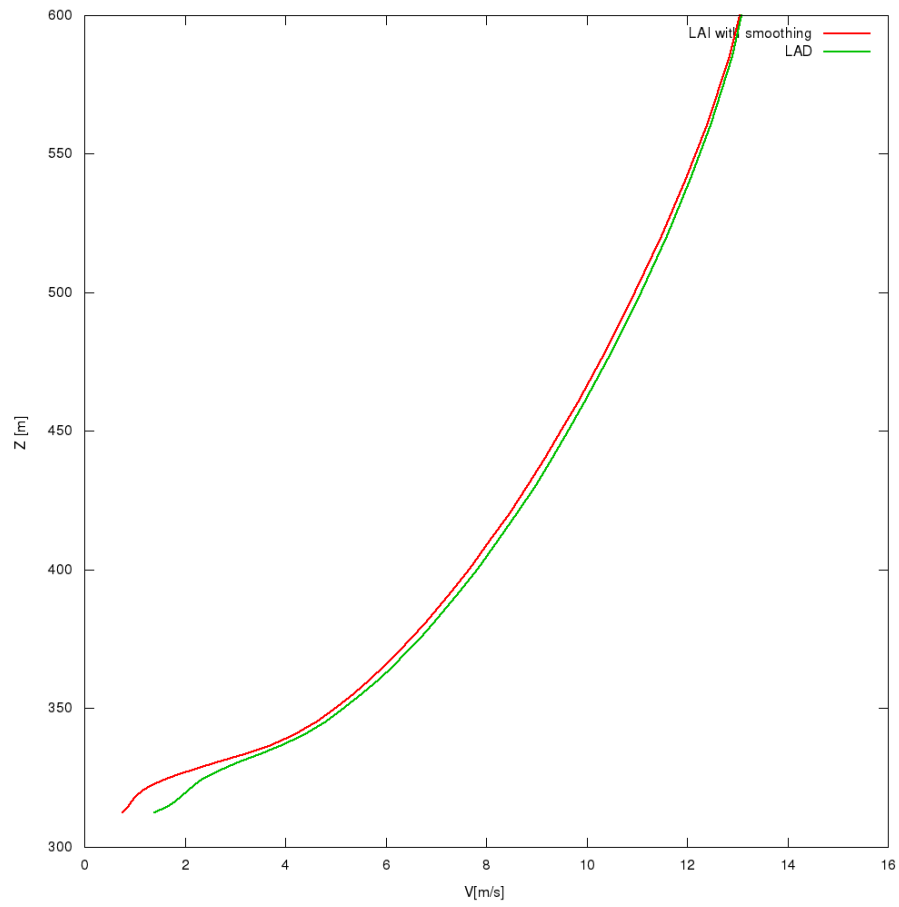


Figure 3.51: Wind speed profiles for smoothed LAI simulation and LAD one

- An higher turning of the wind, especially in the region inside the canopy, due to the higher drag force, as shown in figure 3.52; also for this case the value difference is limited to  $5^\circ$

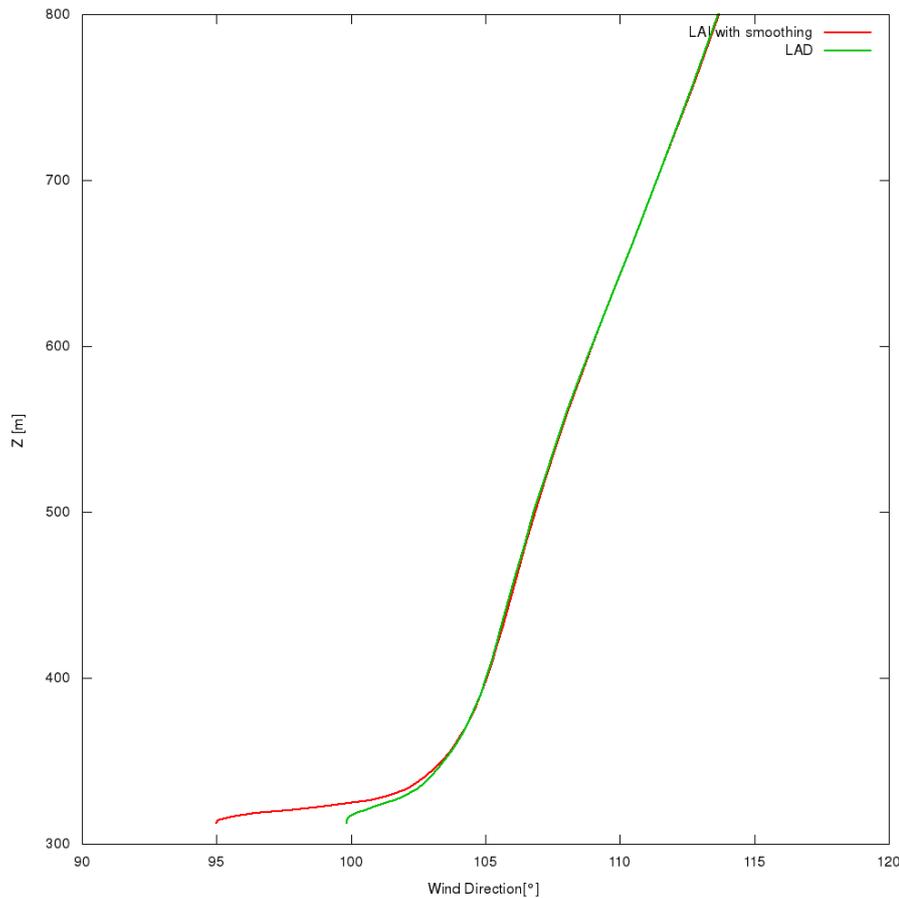


Figure 3.52: Wind direction profiles for smoothed LAI simulation and LAD one

[]

### 3.2.8 Smoothed LAI and mesh refinement comparison

A further comparison between the case with smoothed LAD and the mesh refinement one has been done, due to their similarity. They have been compared also to the normal case and it can be easily seen in figures 3.53, 3.54 and 3.55 that the vertical profile of the turbulent kinetic energy, wind speed and wind direction of the mesh refinement simulation and the smoothed LAI simulation are very similar, while they are different than the normal case.

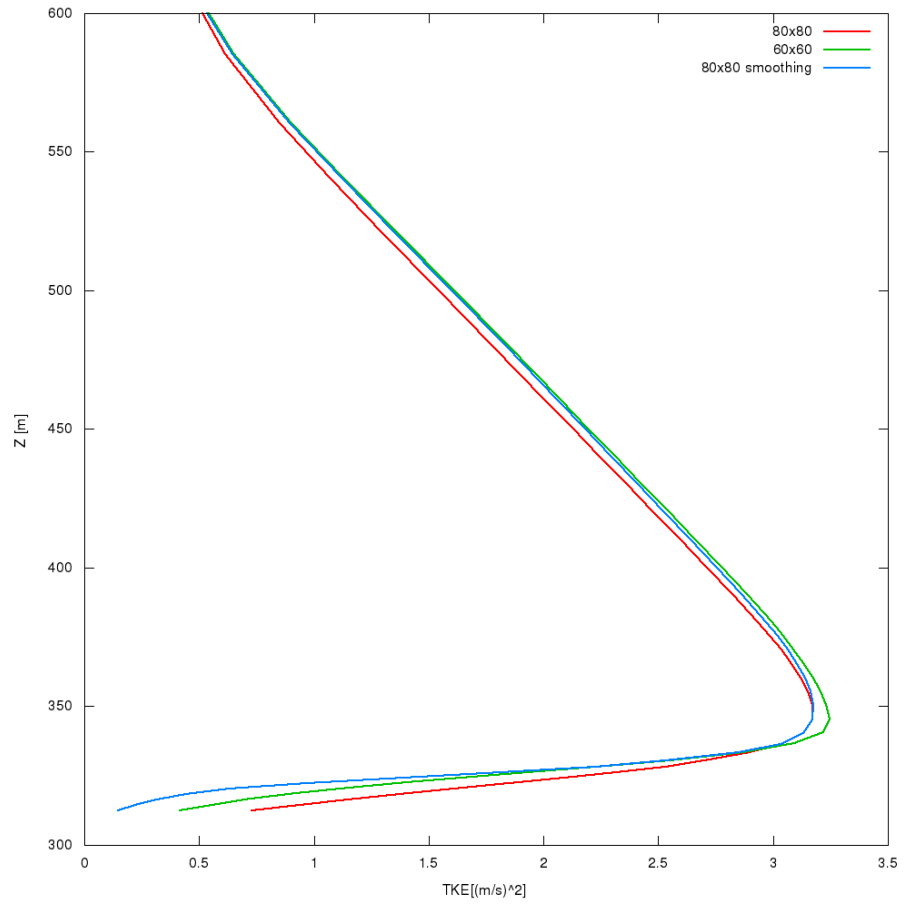


Figure 3.53: TKE profiles for smoothed LAI simulation, mesh refinement and normal ones

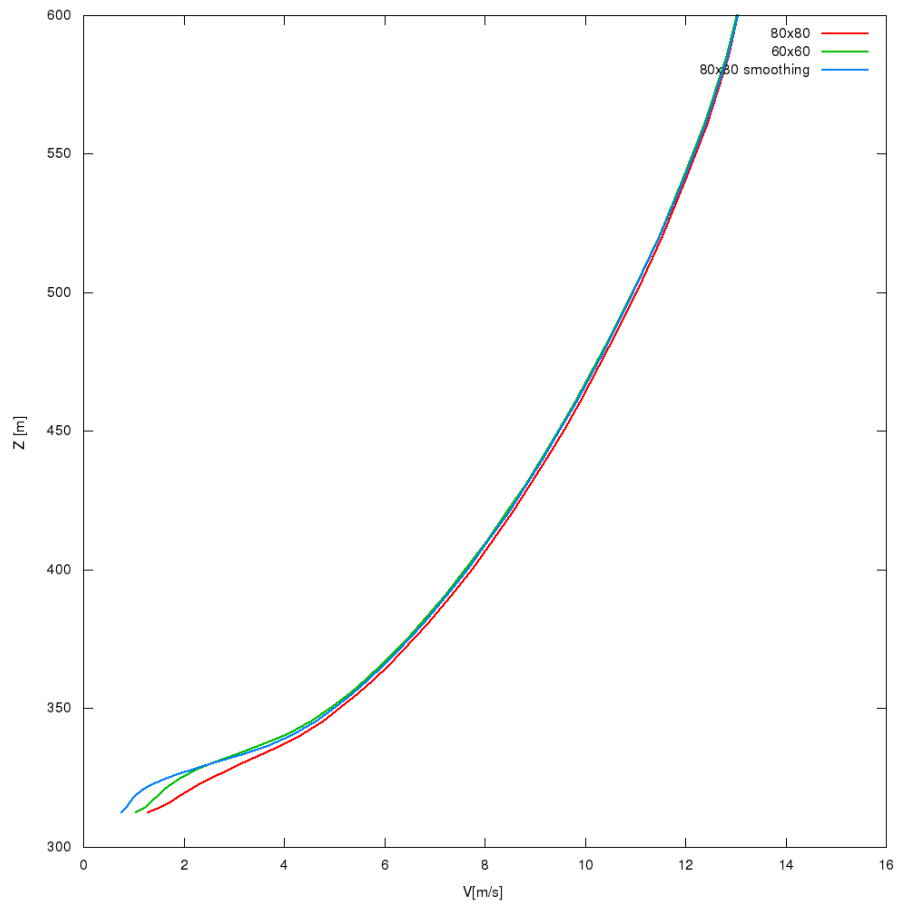


Figure 3.54: Wind speed profiles for smoothed LAI simulation, mesh refinement and normal ones

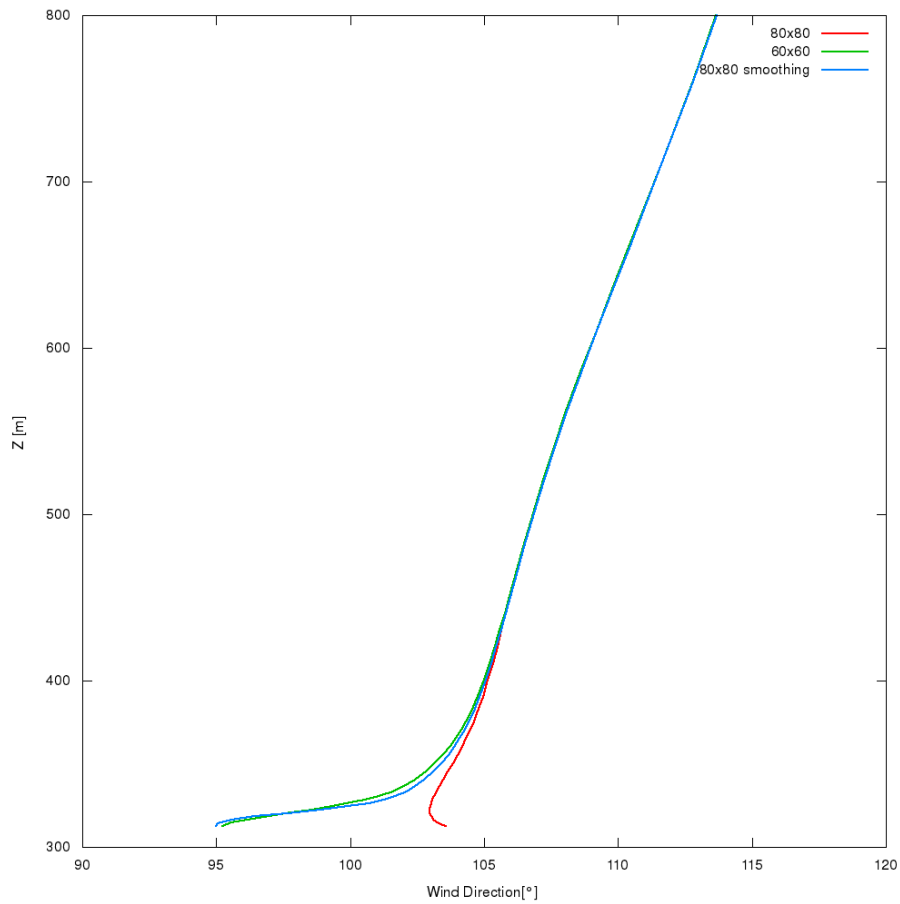


Figure 3.55: Wind direction profiles for smoothed LAI simulation, mesh refinement and normal ones

In order to analyze the reason of this similarity, and noticing that with the case without canopy there was not an evaluable difference between the mesh refinement and the normal case, the attention has been focused on the LAD profiles.

As it can be seen in figure 3.56 , the mesh refinement LAD profile is much more similar to the smoothed value than the normal one.

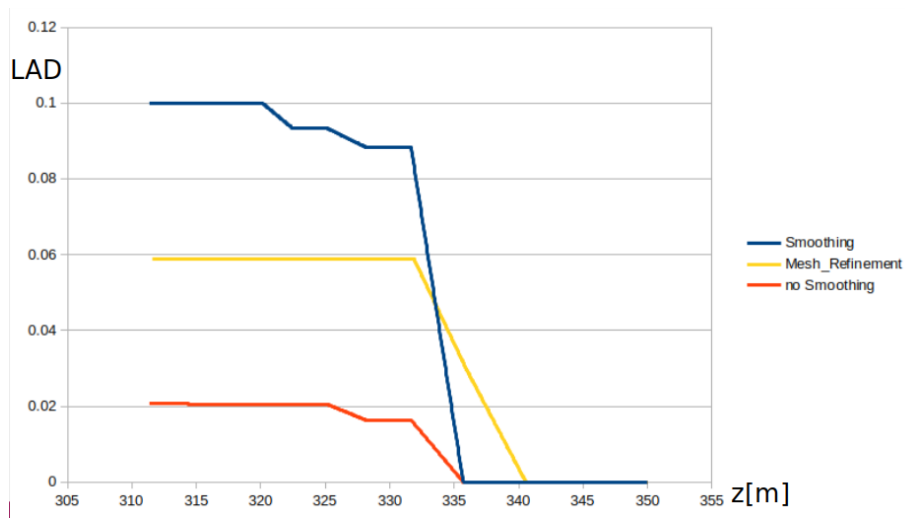


Figure 3.56: LAD profiles for smoothed LAI simulation, mesh refinement and normal ones

Due to this higher value there is an increased value of the drag force that cause, for the simulations with smoothed LAI and the mesh refined one:

- A decreased value for the turbulent kinetic energy inside the canopy
- A lower wind speed inside the canopy
- An higher turning of the wind inside the canopy

### 3.3 Mast 3 Analysis

In addition to mast 7, a similar analysis has been done on mast 3, to figure out if there were confirmations on what was found for mast 7, specially on what concern the different turning of the wind and influence on the type of input data of LAD.

Also a preliminary analysis was computed on mast 1; here, however, a very low canopy presence and a very flat terrain made this analysis useless and it is omitted. Mast 3 has as coordinate 434208.00 m E and 6426942.00 m N and it is, unlike mast 7, one of the most distant from the lake, with an high canopy presence as can be seen in the Google Earth images of the zone in figure 3.57.



Figure 3.57: Mast 3 zone seen from Google earth

The attention has been focused on this mast because, with a preliminary analysis, the different turning of the wind has been highlighted. The simulations done on this mast, that, obviously are the same of mast 7, are :

- 80x80 mesh, LAI input data without smoothing and without buffer
- 80x80 mesh, LAD input data without smoothing and without buffer
- 80x80 mesh, LAI input data with smoothing and without buffer
- 60x60 mesh, LAI input data without smoothing and without buffer
- 80x80 mesh, LAI input data without smoothing and with buffer
- 40x40 mesh, LAI input data without smoothing and without buffer

### 3.3.1 Mesh refinement

The mesh refinement simulations shows little difference for what concern the wind speed and turbulent kinetic energy, while there is a turning in the wind direction in the opposite direction, as shown in figures 3.58, 3.59 and 3.60:

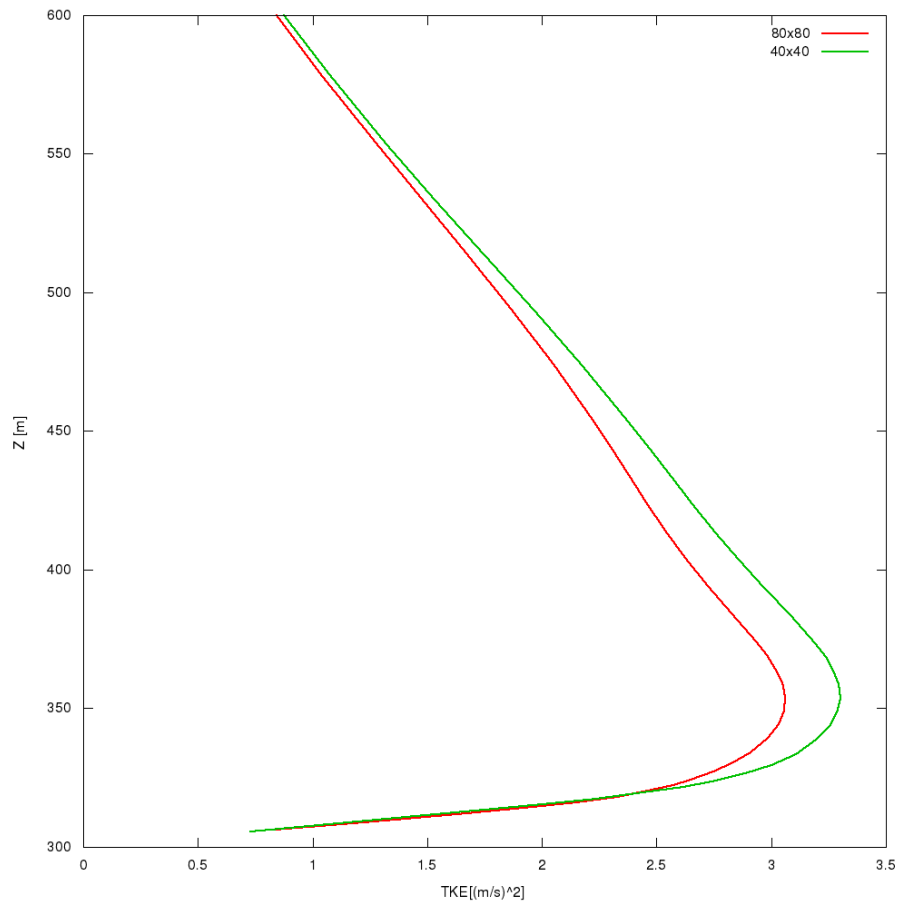


Figure 3.58: TKE profiles for simulation with refined mesh and normal one

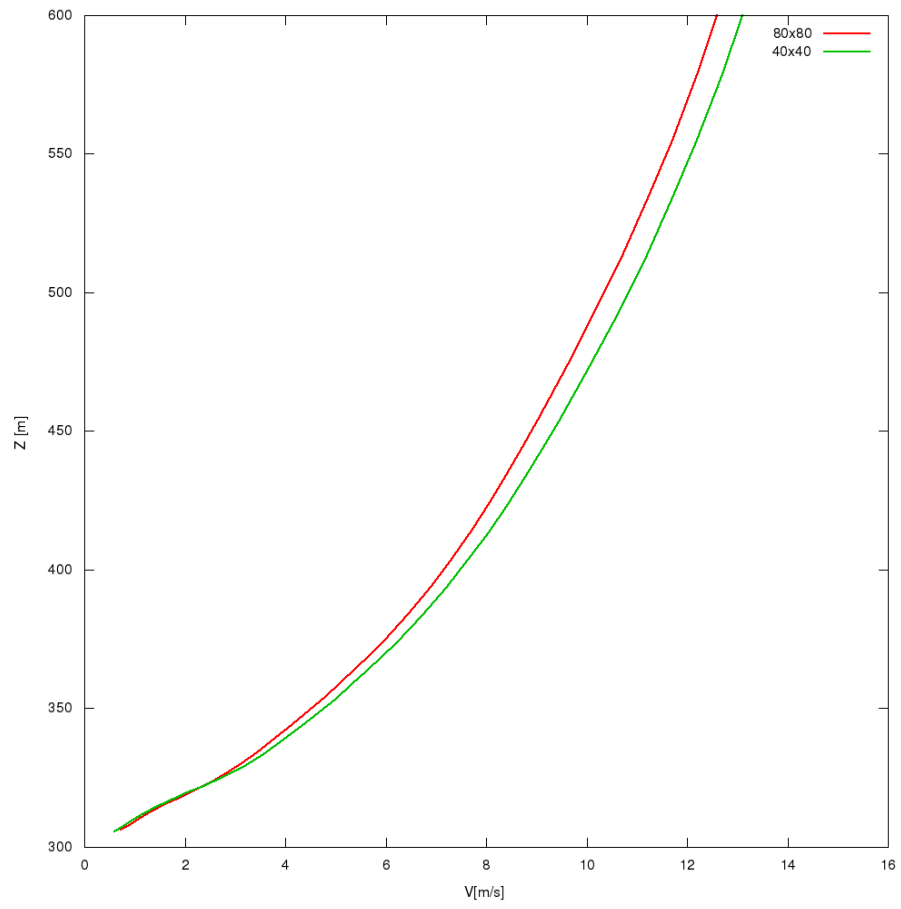


Figure 3.59: Wind speed profiles for simulation with refined mesh and normal one

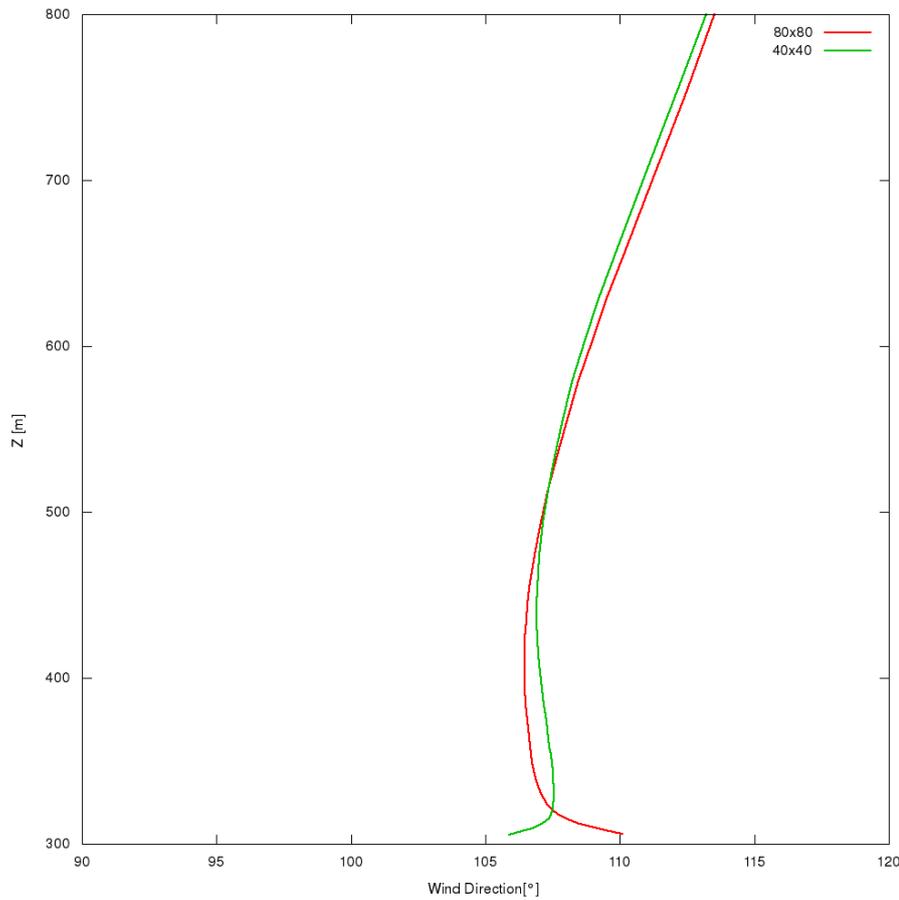


Figure 3.60: Wind direction profiles for simulation with refined mesh and normal one

Due to this difference in the wind direction, a study on the mast has been done to figure out the causes. The causes taken into consideration are mainly three:

- Incoherent dimension of the input data compared with the mesh size of the simulations
- Quite complex terrain topography in the wind direction
- Very heterogeneous leaf area density due to recent cutting and re-planting of trees

### 3.3.2 LAI and LAD input data

The input data, including the LAI and LAD, has been given with a 10x10 m resolution covering 40x40 km of surfaces. The LAD, moreover, was given with a vertical resolution of 1m increasing exponentially the size of the input files.

The mesh size, instead, of the simulations done are the 80x80 m for the coarsest mesh and the 40x40 m for the finest one; note that the finest is four times the input data given, creating a quite evident inconsistency between output and input data.

To be added to this, and this is the main problem of the input data, there is a very noisy profiles of the LAI in the horizontal profiles and also a very noisy profiles in the vertical one for the LAD.

As can be seen in figure 3.61, the input LAI can change from 0 to 8 in a single mesh cell; for this reason, changing the mesh sizes, or more simply slightly shifting the mesh, a very different value can be found for that cell.

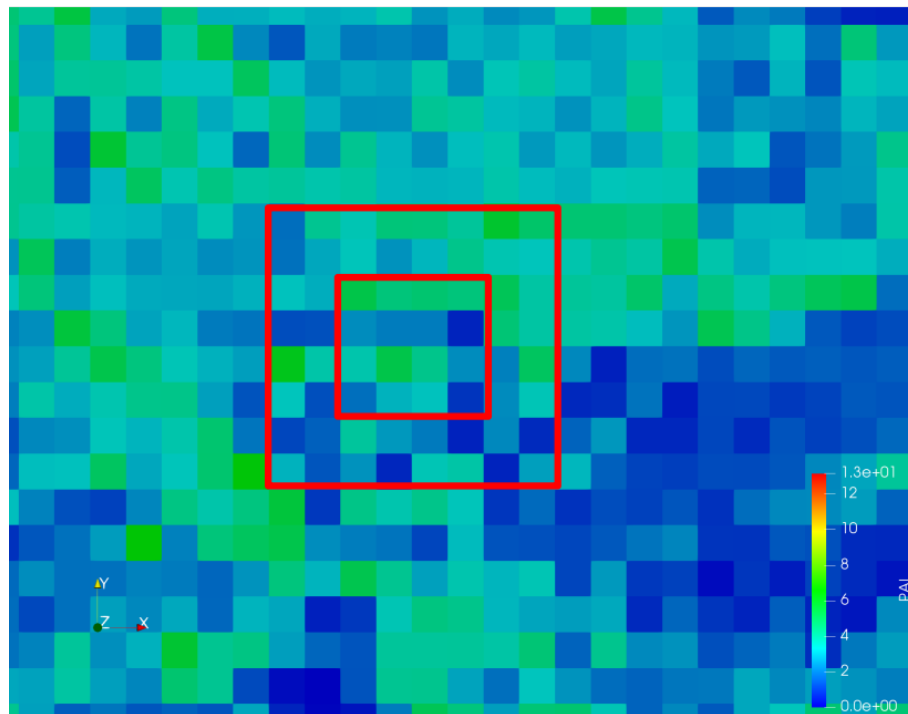


Figure 3.61: Comparison between LAI input and mesh sizes

Also for the vertical profile of the LAD, the input data turns out to be very noisy, as shown in figure 3.62:

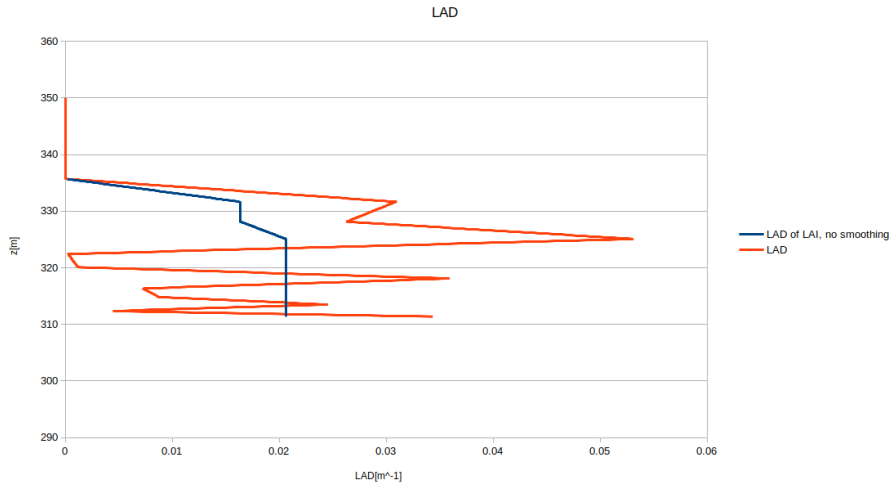


Figure 3.62: Comparison between LAI and LAD profiles

The equations utilized are:

$$\frac{\partial}{\partial t} \mathbf{u} + \mathbf{u} \cdot \nabla \mathbf{u} = -\nabla \left( \frac{p}{\rho} \right) + \nabla \cdot (\nu_t \nabla^s \mathbf{u}) - 2\omega \times \mathbf{u} - C_d LAD |\mathbf{u}| \mathbf{u} \quad (3.3)$$

$$\frac{\partial}{\partial t} \epsilon + \mathbf{u} \cdot \nabla \epsilon = +\nabla \cdot \left( \frac{\nu_t}{\sigma_\epsilon} \nabla \epsilon \right) + \frac{\epsilon}{k} (C_1 P_k - C_2 \epsilon + C_3 C_d LAD |\mathbf{u}| k) \quad (3.4)$$

Changing the LAD value, in those equations, means considerably change the behaviour of the wind described by them, causing an apparent inconsistency between different mesh sizes.

This differences are more evident in the wind direction, that shows a different turning of the wind, because it is very sensitive to the changes in the single components of the equations.

A new branch of the wind study is becoming to study individually the impact of the single components of the equations on the wind behaviour, but it is a very expensive and complex study.

*Look for the paper about this topic*

### 3.3.3 Terrain topography

While terrain topography for other masts can be consider almost flat or semi complex, for mast 3 zone there is a complex terrain with high differences, especially following the wind direction considered in the simula-

tions. As can be seen in the figure 3.63, the mast 3 position is in a higher zone and quite complex zone, creating a very complex wind behaviour:

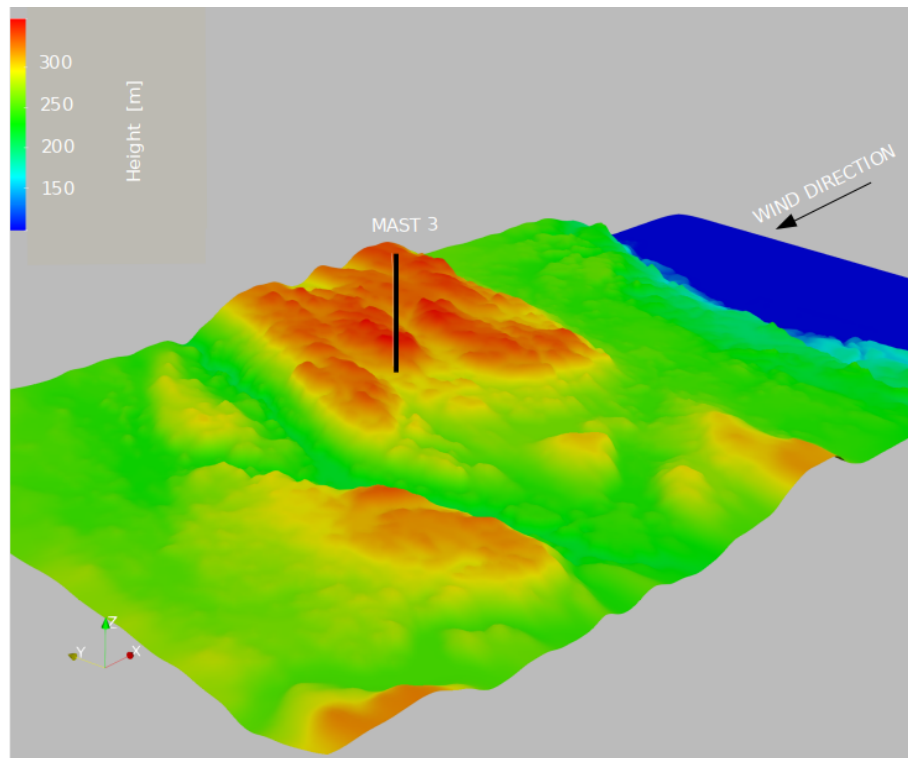


Figure 3.63: Terrain topography and mast 3 position

Seeing the profile of terrain in figure 3.64 in the wind direction, you can better appreciate the complexity of the topography before that the wind, coming from the lake, arrives to the mast 3, where the simulations are compared and the differences highlighted.



Figure 3.64: Terrain topography in wind direction and mast 3 position

### 3.3.4 Changes in the zone

The last feature that can have an effect on the turning of the wind is the heterogeneity of the zone, due to continuous cutting and re-planting of the trees that have produced a zone in which there are the coexistence of old and tall trees with very young and short trees with very different leaf area density and leaf area index, parameters which affects the RANS equations used in this work.

As can be seen in figure 3.65 that represent the zone around mast 3 in 2018, or even better in the figure 3.66 that represent the same zone but in 2006 when the cutting of one portion of the zone is more evident, the canopy profile in the wind direction is very complex.



Figure 3.65: Google Earth capture of the zone around mast 3 in 2018



Figure 3.66: Google Earth capture of the zone around mast 3 in 2006

In figure 3.67, instead, is shown the input data for the canopy in the zone around mast 3.

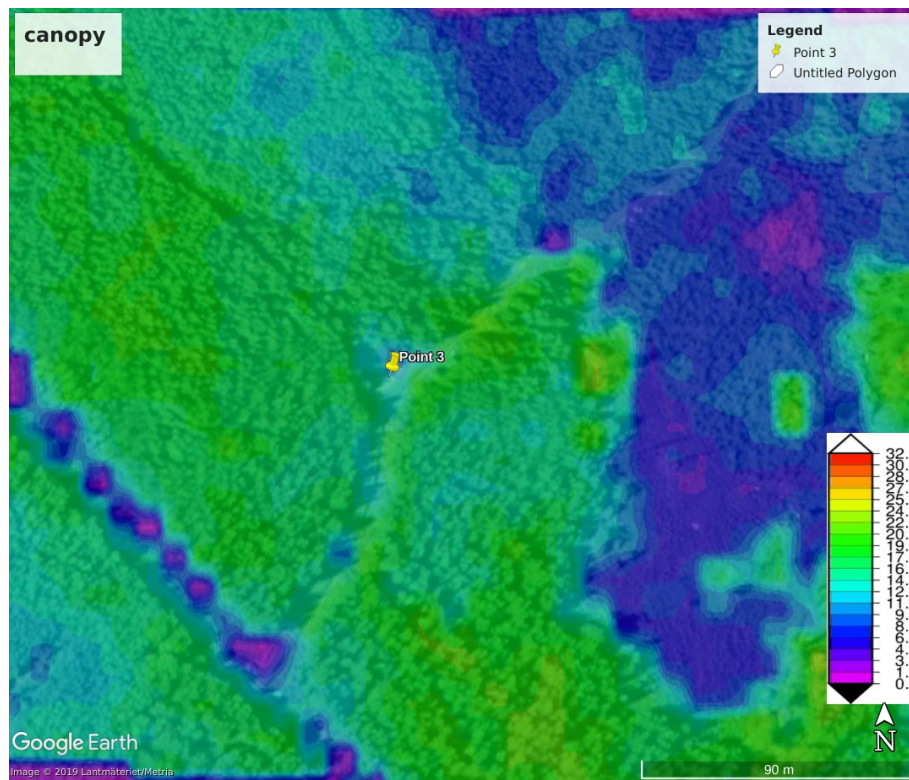


Figure 3.67: Input data of canopy height in the zone around mast 3

To highlight the LAD profile in the wind direction before mast 3, a cut in the wind direction itself has been performed comparing the case which represent the simulation with the normal size of the mesh (80x80) and the simulation with the refined size of the mesh(40x40).



Figure 3.68: LAD values in the wind direction for the normal mesh simulation

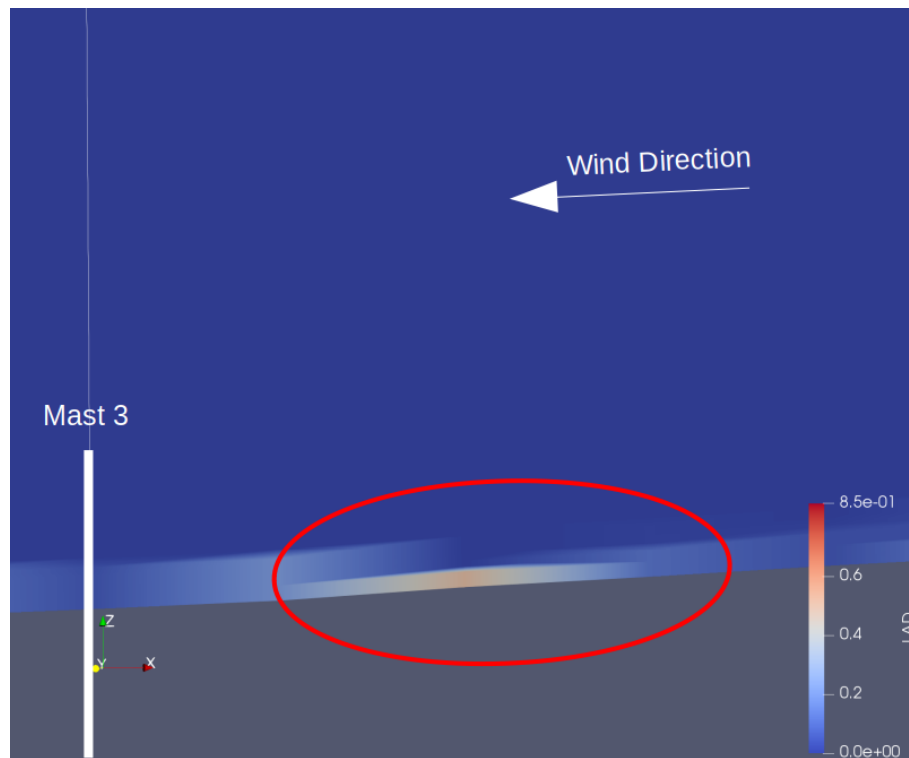


Figure 3.69: LAD values in the wind direction for the refined mesh simulation

As can be seen comparing them, in figure 3.68 the LAD value in front of the mast has a lower and more uniform value, while in figure 3.69 is evident an higher LAD value with a less uniform distribution. This relevant difference is due mainly to the noisiness of the input data of the LAD.

Finally, in order to have an overview of the whole effects on the simulations, a comparison between the normal case, the refined case and the smoothed case have been developed, with an horizontal cut at an height of 10 m showing the wind direction, wind speed, LAD and height of the terrain values.

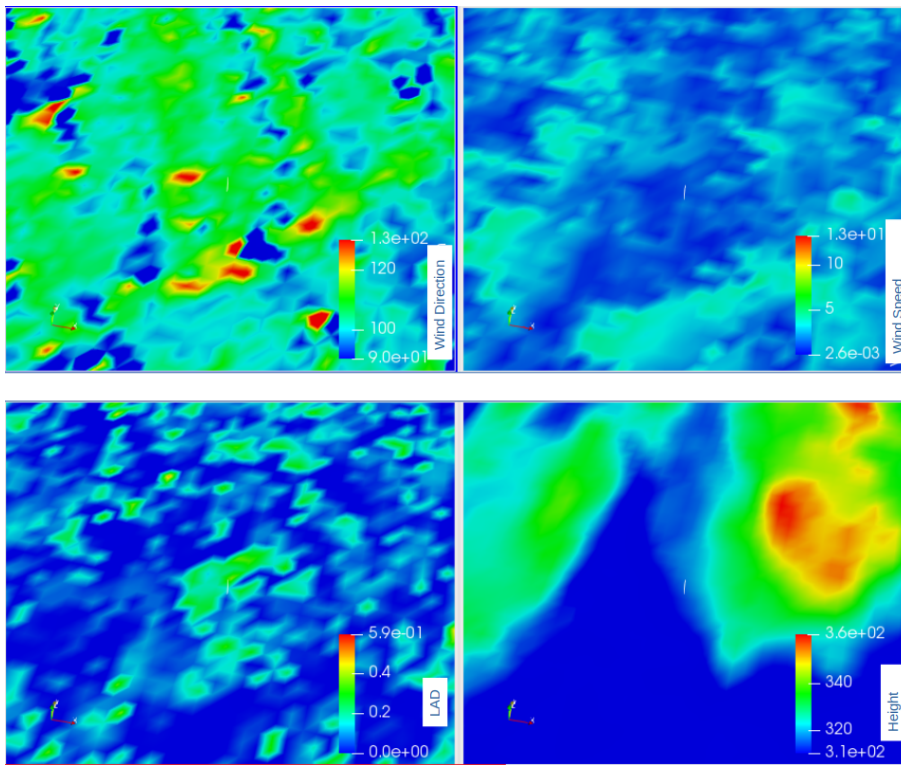


Figure 3.70: Horizontal cut at height of 10 m of wind speed, wind direction, LAD, and terrain height for normal mesh (80x80)

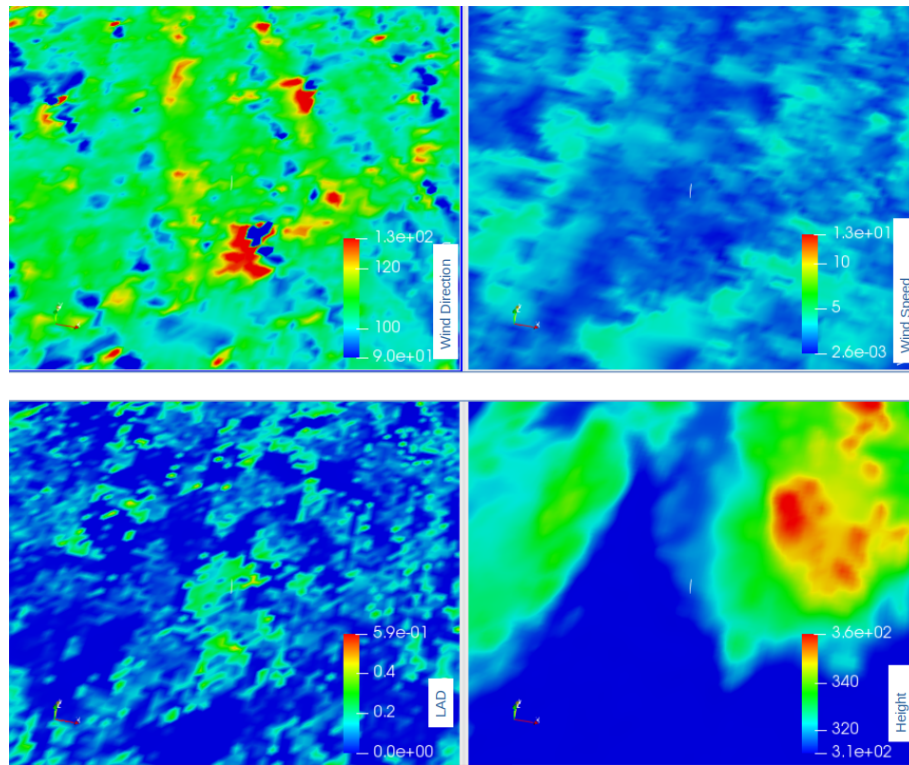


Figure 3.71: Horizontal cut at height of 10 m of wind speed, wind direction, LAD, and terrain height for refined mesh (40x40)

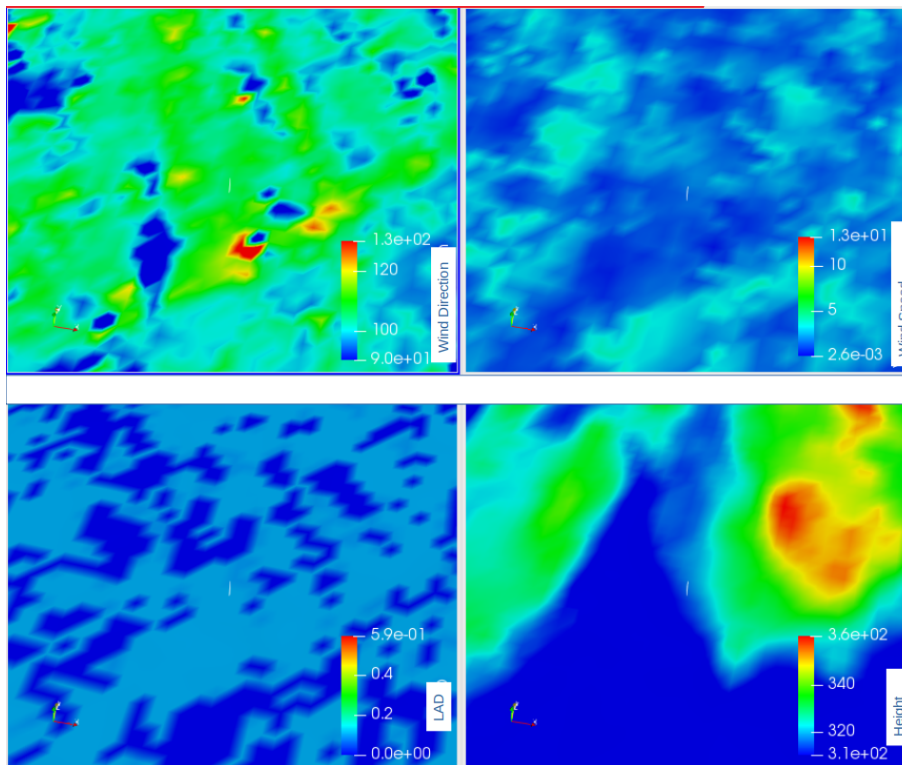


Figure 3.72: Horizontal cut at height of 10 m of wind speed, wind direction, LAD, and terrain height for normal mesh and smoothed value of LAD

As can be seen in figures 3.70, 3.71 and 3.72, the overall shape remains almost constant for all the 4 values, while going from the smoothed case to the refined case the accuracy of the values increases, making also increase the noisiness both of the input values (LAD and terrain height) and of the output values (Wind direction and wind speed).

### 3.3.5 Optimization

In the end of the work, an optimization analysis has been developed. Using the same mesh for all of them, three simulations have been compared:

- Normal mesh without optimization

- Normal mesh with optimization

The optimization, used especially for zones with high topographic gradients, is done in order to increase the elemental quality of the mesh.

The extruding direction for a given node of a mesh, in fact, is computed as the pseudo-normal direction, using an average normal of the adjacent elements, that maximizes the orthogonality of the new generated layer.[11]

Each extruding step is combined with a non-linear optimization of the element quality to improve the mesh configuration before generating a new layer of hexahedra.

In our case, being the zone semi-complex, there are not several zones with high topographic gradients and so the improvement of the computational cost does not witness an evident advantage.

As shown in figure 3.73, the turbulent term witness a quite evident advantage in the convergence; but, instead, the whole RANS equation show no improvements, as can be seen in figure 3.74 due to the small impact of the viscosity term.

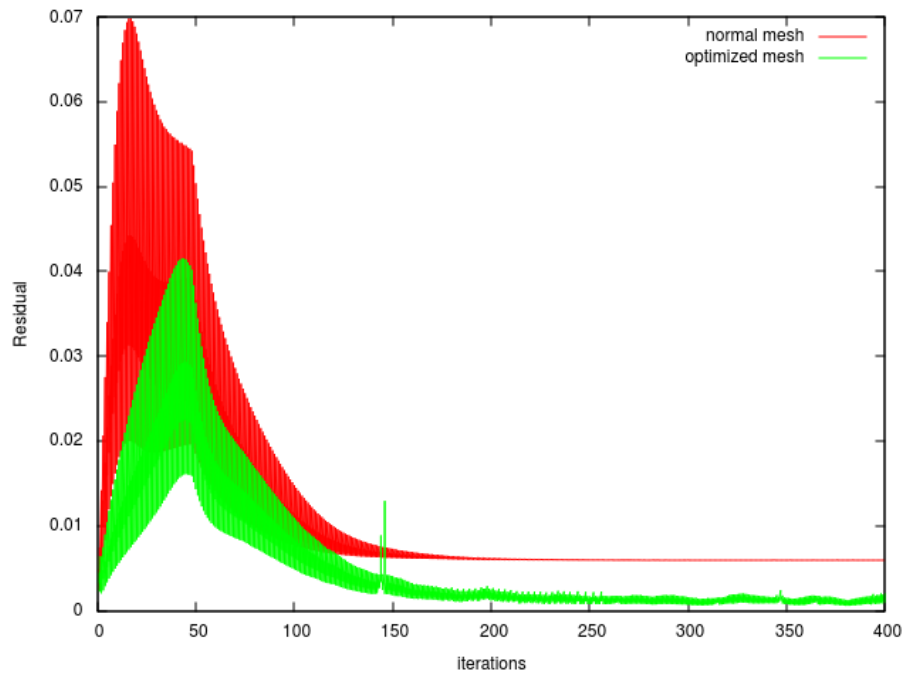


Figure 3.73: Convergence trend of the Turbulent term

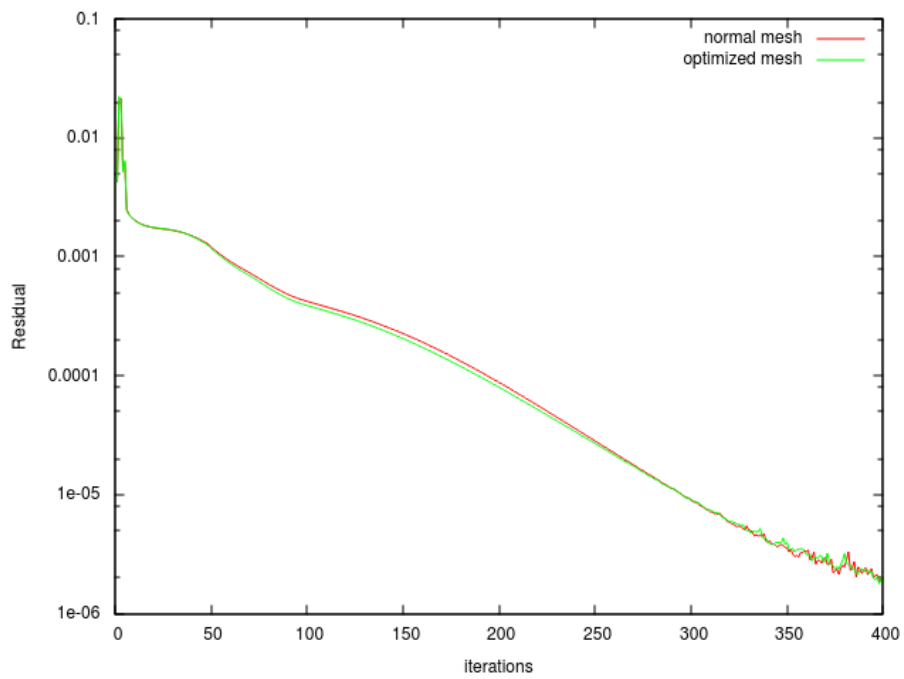


Figure 3.74: Convergence trend of the Navier Stokes equation



## 4 Conclusion

This thesis has as aim the study of the impact of different physical and numerical characteristic on main wind parameters.

The study of the wind is a very complex topic which is in development in the last years but still needs very high computational efforts and several simplifications; moreover, as seen for the leaf area density and leaf area index, following the approach of E. Dellwik et al. for the solitary tree [6], there is not a direct correlation between higher resolution and better results, making the topic more complex.

Despite of those drawbacks the topic has remarkable margins of improvement and it can really help wind industry in the development of farms in location that were excluded in the past.

For this specific site analyzed in this work a semi-complex terrain made the analysis simpler for what concern the study of the impact of the terrain, but quite challenging for the relevant and heterogeneous presence of the canopy; in fact, as seen in the previous chapter the simulations differences, except for the Coriolis effect, became relevant when the canopy is introduced.

Leaving aside the simulations differences for mesh refinement and of the buffer presence that in our case are not so relevant both for the semi-complexity of the terrain and due to the fact that the wind comes from the lake, a very flat zone, the more relevant part of this thesis is the analysis of the leaf area density, the leaf area index and the smoothing of its value.

In fact, as can be easily seen, the computational cost considerably increases when using as input smoothed value of LAI, LAI and LAD but this increase does not coincide with an evident improvement in the results.

Contrairwise, in cases like theses, where the input data of the LAD are not taken considering the computational limit, and a very high noise can be seen in both the vertical and horizontal direction, the use of the LAD instead of simpler value, can have a negative effect making the output values very noisy and depending on mesh sizes, mesh orientation and so on.

This analysis can be useful in order to save money both from the experimental point of view in which input data are taken and both from the computational costs.

The smoothing, furthermore, here used very roughly to understand its behaviour and decrease the computational efforts, can be improved and refined in order to find a compromise between computational cost and physical behaviour.

Those impact can be also study in deeper considering both non stationary cases and unstable atmospheres in order to take in account the time and the effect of temperature and thermal phenomena here neglected and also using LES simulations comparing them with the RANS ones.

Moreover it can be also studied in deeper the turning on the wind, that, as seen in this work, is the most sensible parameter to the input data variation and it is not still clear its behavior in complex and canopy terrain, but it is a key parameter for a proper future wind turbine installation.

# List of Figures

2.1	Region of atmospheric stability, unstability and neutrality, function of the thermal gradient trend in the height . . . . .	18
3.1	Zone considered for the simulation [7] . . . . .	23
3.2	Example of the three zones [4] . . . . .	24
3.3	Height of the zone under study [7] . . . . .	26
3.4	Height of the zone under study, zoom in the masts zone [7] .	26
3.5	Comparison of the wind speed between the 80x80 mesh and the refined 40x40 mesh . . . . .	27
3.6	Comparison of the wind speed between the 80x80 mesh and the refined 40x40 mesh, zoom up to 500 m . . . . .	27
3.7	Comparison of the turbulent kinetic energy $k$ between the 80x80 mesh and the refined 40x40 mesh . . . . .	28
3.8	Comparison of the wind speed between the 80x80 mesh and the refined 40x40 mesh, zoom up to 400 m . . . . .	28
3.9	Comparison of the simulated zone with and without buffer .	29
3.10	Comparison of the wind speed for the simulations with and without buffer . . . . .	30
3.11	Comparison of the wind speed for the simulations with and without buffer, zoom up to 550 m . . . . .	30
3.12	Comparison of the turbulent kinetic energy $k$ for the simulations with and without buffer, zoom up to 600 m . . . . .	31
3.13	Comparison of the wind speed for the simulations with and without Coriolis force . . . . .	32
3.14	Comparison of the wind direction for the simulations with and without Coriolis force . . . . .	33

3.15	Comparison of the turbulent kinetic energy $k$ for the simulations with and without Coriolis force . . . . .	34
3.16	Input data of the canopy height in the simulated domain . .	35
3.17	Input data of LAD values at different height . . . . .	36
3.18	input data of the canopy height in the simulated domain . .	37
3.19	Canopy height in mast 7 zone in 2015 . . . . .	38
3.20	Canopy height in mast 7 zone in 2011 . . . . .	39
3.21	Canopy height input data . . . . .	39
3.22	TKE profile for simulations with and without canopy . . . .	40
3.23	Wind speed profile for simulations with and without canopy	41
3.24	Wind direction profile for simulations with and without canopy	42
3.25	TKE profile for simulations for normal and refined mesh . .	43
3.26	Wind speed profile for simulations for normal and refined mesh . . . . .	44
3.27	Wind direction profile for simulations for normal and refined mesh . . . . .	45
3.28	Simulated zone with buffer . . . . .	46
3.29	Simulated zone without buffer . . . . .	46
3.30	Impact of buffer on the boundaries of the farm zone . . . . .	47
3.31	TKE profiles for simulations with and without buffer . . . .	48
3.32	Zoom of TKE profiles for simulations with and without buffer	49
3.33	Wind speed profiles for simulations with and without buffer	50
3.34	Zoom of wind speed profiles for simulations with and without buffer . . . . .	51
3.35	Wind direction profiles for simulations with and without buffer . . . . .	52
3.36	Zoom of wind direction profiles for simulations with and without buffer . . . . .	53
3.37	Comparison in the LAD vertical profile between LAD and LAI input data . . . . .	54
3.38	TKE profile comparison between LAI and LAD input data .	55
3.39	TKE profile zoom in the lower zone between LAI and LAD input data . . . . .	56

3.40	Wind speed profile comparison between LAD and LAI input data . . . . .	57
3.41	Wind speed zoom in the lower zone between LAD and LAI input data . . . . .	58
3.42	Wind direction profile comparison between LAI and LAD input data . . . . .	59
3.43	Comparison between the LAI actual value and the smoothed one . . . . .	60
3.44	TKE profile comparison between actual value and smoothed one . . . . .	61
3.45	TKE profile zoom in the lower zone between actual value and smoothed one . . . . .	62
3.46	Wind speed profile comparison between actual value and smoothed one . . . . .	63
3.47	Wind speed zoom in the lower zone between actual value and smoothed one . . . . .	64
3.48	Wind direction profile comparison between actual value and smoothed one . . . . .	65
3.49	Comparison between smoothed LAI values and LAD values . . . . .	66
3.50	TKE profiles for smoothed LAI simulation and LAD one . . . . .	67
3.51	Wind speed profiles for smoothed LAI simulation and LAD one . . . . .	68
3.52	Wind direction profiles for smoothed LAI simulation and LAD one . . . . .	69
3.53	TKE profiles for smoothed LAI simulation, mesh refinement and normal ones . . . . .	70
3.54	Wind speed profiles for smoothed LAI simulation, mesh refinement and normal ones . . . . .	71
3.55	Wind direction profiles for smoothed LAI simulation, mesh refinement and normal ones . . . . .	72
3.56	LAD profiles for smoothed LAI simulation, mesh refinement and normal ones . . . . .	73
3.57	Mast 3 zone seen from Google earth . . . . .	74
3.58	TKE profiles for simulation with refined mesh and normal one . . . . .	75

3.59	Wind speed profiles for simulation with refined mesh and normal one . . . . .	76
3.60	Wind direction profiles for simulation with refined mesh and normal one . . . . .	77
3.61	Comparison between LAI input and mesh sizes . . . . .	78
3.62	Comparison between LAI and LAD profiles . . . . .	79
3.63	Terrain topography and mast 3 position . . . . .	80
3.64	Terrain topography in wind direction and mast 3 position . .	81
3.65	Google Earth capture of the zone around mast 3 in 2018 . . .	82
3.66	Google Earth capture of the zone around mast 3 in 2006 . . .	83
3.67	Input data of canopy height in the zone around mast 3 . . .	84
3.68	LAD values in the wind direction for the normal mesh simulation . . . . .	85
3.69	LAD values in the wind direction for the refined mesh simulation . . . . .	86
3.70	Horizontal cut at height of 10 m of wind speed, wind direction, LAD, and terrain height for normal mesh (80x80) . . . .	87
3.71	Horizontal cut at height of 10 m of wind speed, wind direction, LAD, and terrain height for refined mesh (40x40) . . . .	88
3.72	Horizontal cut at height of 10 m of wind speed, wind direction, LAD, and terrain height for normal mesh and smoothed value of LAD . . . . .	89
3.73	Convergence trend of the Turbulent term . . . . .	90
3.74	Convergence trend of the Navier Stokes equation . . . . .	91

## References

- [1] P. H. Alfredsson and A. Segalini. “Introduction Wind farms in complex terrains: an introduction”. In: *Philosophical Transactions of the Royal Society A: Mathematical, Physical and Engineering Sciences* 375.2091 (2017), p. 20160096. DOI: 10.1098/rsta.2016.0096. eprint: <https://royalsocietypublishing.org/doi/pdf/10.1098/rsta.2016.0096>. URL: <https://royalsocietypublishing.org/doi/abs/10.1098/rsta.2016.0096>.
- [2] David Apsley and I P Castro. “A limited-length-scale k- model for the neutral and stably-stratified atmospheric boundary layer”. English. In: *Boundary-Layer Meteorology* 83 (1997), pp. 75–98. ISSN: 0006-8314.
- [3] M Avila et al. “Daily cycle simulations of thermally stratified flows over forests”. In: *Journal of Physics: Conference Series* 1256 (July 2019), p. 012003. DOI: 10.1088/1742-6596/1256/1/012003. URL: <https://doi.org/10.1088>.
- [4] Jordi Barcons, Matias Avila, and Arnau Folch. “Diurnal cycle RANS simulations applied to wind resource assessment”. In: *Wind Energy* 22.2 (2019), pp. 269–282. DOI: 10.1002/we.2283. eprint: <https://onlinelibrary.wiley.com/doi/pdf/10.1002/we.2283>. URL: <https://onlinelibrary.wiley.com/doi/abs/10.1002/we.2283>.
- [5] “BSC website, <https://www.bsc.es/research-development/research-areas/engineering-simulations/alya-high-performance-computational>”. In: (). URL: <https://www.bsc.es/research-development/research-areas/engineering-simulations/alya-high-performance-computational>.
- [6] E. Dellwik et al. “Observed and modeled near-wake flow behind a solitary tree”. In: *Agricultural and Forest Meteorology* 265 (2019), pp. 78–87. ISSN: 0168-1923. DOI: <https://doi.org/10.1016/j>.

- agrformet.2018.10.015.URL: <http://www.sciencedirect.com/science/article/pii/S0168192318303393>.
- [7] “Hornamossen benchmark website, <https://windbench.net/hornamossen>”. In: (). URL: <https://windbench.net/hornamossen>.
- [8] “IRENA website, <https://www.irena.org/wind>”. In: (). URL: <https://www.irena.org/wind>.
- [9] S. Ivanell et al. “Microscale model comparison (benchmark) at the moderate complex forested site Ryningsnäs”. In: *Wind Energy Science Discussions* (Apr. 2018), pp. 1–27. DOI: 10.5194/wes-2018-20.
- [10] M P van der Laan et al. “Predicting wind farm wake interaction with RANS: an investigation of the Coriolis force”. In: *Journal of Physics: Conference Series* 625 (June 2015), p. 012026. DOI: 10.1088/1742-6596/625/1/012026. URL: <https://doi.org/10.1088/1742-6596/625/1/012026>.
- [11] Abel Gargallo-Peiró Matias Avila and Arnau Folch. “Paper of the formulation of the CFD model against experimental data”. In: (Apr. 2017).
- [12] Obukhov A. Monin A. S. “Basic laws of turbulent mixing in the surface layer of the atmosphere”. In: *Contrib. Geophys. Inst. Acad. Sci. USSR. IX 1954. 151. 163–187* (1954).
- [13] Andrey Sogachev, Mark Kelly, and Monique Leclerc. “Consistent Two-Equation Closure Modelling for Atmospheric Research: Buoyancy and Vegetation Implementations”. In: *Boundary-Layer Meteorology* 145 (Nov. 2012). DOI: 10.1007/s10546-012-9726-5.
- [14] Paul van der Laan and Niels N. Sørensen. “Why the Coriolis force turns a wind farm wake clockwise in the Northern Hemisphere”. English. In: *Wind Energy Science* 2 (2017), pp. 285–294. ISSN: 2366-7443. DOI: 10.5194/wes-2-285-2017.